Determination of the interface structures of the multilayer system MgO/Fe/GaAs(001)
-
An x-ray photoelectron spectroscopy and diffraction study

Dissertation
zur Erlangung des akademischen Grades
Dr. rer. nat.
der Fakultät Physik
der Technischen Universität Dortmund

vorgelegt von

Dipl. Phys. Dominique Krull
geb. Handschak
geboren in Burg

Lehrstuhl für Experimentelle Physik 1
Fakultät Physik
Otto-Hahn-Str. 4
D-44221 Dortmund
Technische Universität Dortmund

-Dezember 2014-

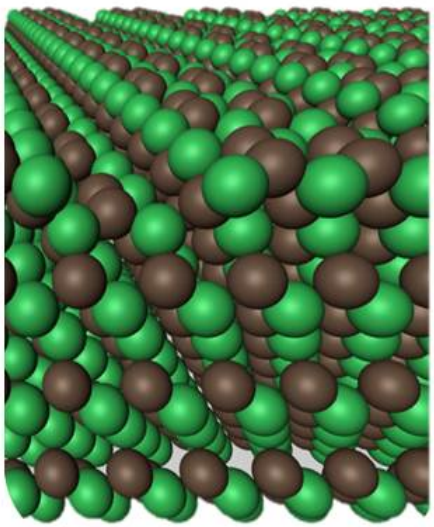

technische universität
dortmund

The action occurs at the interface!

Erster Gutachter:	Prof. Dr. Carsten Westphal
Zweiter Gutachter:	Dr. Kai P. Schmidt
Vorsitzender der Prüfungskommission:	Prof. Dr. Dr. Wolfgang Rhode
Vertreterin der wissenschaftlichen Mitarbeiter:	Dr. Bärbel Siegmann

Abgabedatum: 09. 12. 2014
Tag der Disputation: 16. 01. 2015

Abstract

In this thesis, the interfaces of the spintronics multilayer system MgO/Fe/GaAs(001) are determined. The Tunnel Magneto Resistance (TMR) and Giant Magneto Resistance (GMR) effects used for spintronics devices arise at the interfaces of the junctions and are influenced by the chemical and structural properties.
A very suitable tool for investigating thin-films and interfaces of multilayers is photoelectron spectroscopy. It allows a detailed chemical investigation by high-resolution core level spectra of each element. The spectral components contained in the signals provide information of the local bonding, e.g. whether the emitter is located as a part of a dimer at the surface or located within a bonding beneath the surface. The intensity of the signals varies as a function of polar- and azimuth-angle. This is a result of diffraction and scattering events of the out-going electron wave at neighboring atoms around the emitter atom. Therefore, photoelectron diffraction allows a structure analysis of the surface. The combination of high-resolution spectra and diffraction patterns enable a detailed analysis of each individual layer.
The MgO/Fe/GaAs(001) system was prepared in-situ and investigated successively by using synchrotron light from beamline 11 of the electron storage ring DELTA. Thereby, the necessity of a reconstructed GaAs-surface to ensure an epitaxial growth of the Fe-film is verified by XPD patterns of the Fe/GaAs(001) and Fe/GaAs(4×2)-system. The spectra clearly show a chemical bonding between the Fe-film and the GaAs-substrate. The diffraction patterns reveal an epitaxial growth of Fe on GaAs(4×2), but in a pyramid-like structure due to simultaneous layer and island growth. Iron is deposited on a cleaned GaAs(001)-surface, but the inter-diffusion is strong as the Fe-film is completely amorphous. The Ga-rich (4×2)-reconstruction prevents a diffusion and ensures an epitaxial growth of the Fe-layer.
The topmost MgO-layers were prepared on the well-ordered Fe(001)-surface and grow epitaxial. The Fe was oxidized at the surface and was found in a two layer thick FeO-film due to MgO-deposition. The MgO-film is halite structured and shows a lattice misfit by slightly shifted Mg-atoms. This shift was confirmed at thin and thick MgO-films and may be induced by the substrate, because the Fe/GaAs-interface clearly influences the MgO/Fe-interface structure.
Furthermore, the chemical and structural changes may influence the magnetic properties of the multilayer system. Hence, they are verified by magneto-optical measurements using T-MOKE. The spectra reveal a strong reaction of the Fe-interlayer on the external magnetic field. Further, the T-MOKE analysis reveals non-magnetic properties of the GaAs-substrate nor the thin MgO-film. An additional hysteresis measurement showed excellent ferromagnetic properties of the remaining Fe despite all chemical and structural changes.

Kurzfassung

Die vorliegende Arbeit befasst sich mit der Untersuchung der Grenzflächen des Spintronik Mehrschichtsystems MgO/Fe/GaAs(001). Der magnetische Tunnelwiderstand (TMR) und der Riesenmagnetowiderstand (GMR), die in Spintronikbauelementen Anwendung finden, treten an den Grenzflächen auf und werden durch die chemischen und strukturellen Eigenschaften beeinflusst.
Die Photoelektronenspektroskopie eignet sich besonders zur Analyse von dünnen Filmen und Grenzstrukturen von Mehrschichtsystemen. Sie ermöglicht eine genaue chemische Untersuchung über hochaufgelöste Spektren der Rumpfniveaus einzelner Elemente. Die spektralen Komponenten in einem Signal beinhalten Informationen über die lokalen Bindungen, z.B. ob der Emitter in einen Oberflächen-Dimer oder in einer tiefer liegende Schicht gebunden ist. Die Signalintensität variiert als Funktion von Polar- und Azimutwinkel. Ursächlich hierfür sind Beugungs- und Streuungseffekte der emittierten Elektronenwelle an benachbarten Atomen. Die Kombination aus hochaufgelösten Spektren und Beugungsbildern erlaubt eine detaillierte Analyse jeder einzelnen Schicht.
Das MgO/Fe/GaAs(001)-System wurde in-situ präpariert und sukzessive unter Verwendung von Synchrotronstrahlung der Strahllinie 11 des Speicherings DELTA untersucht. Dabei wurde die Notwendigkeit einer GaAs Oberflächenrekonstruktion für epitaktisches Wachstum des Fe-Films nachgewiesen.
Die Spektren der Fe/GaAs(4×2) und Fe/GaAs(001) Systeme weisen eindeutige chemische Bindungen auf. Die Beugungsbilder zeigen ein epitaktisches Wachstum von Fe auf GaAs(4×2) in einer pyramidalen Struktur, die durch das gleichzeitige Insel- und Lagenwachstum verursacht wird. Das Eisen reichert sich auf einer gereinigten GaAs(001) Oberfläche an, allerdings ist die Austausch-Diffusion so stark, dass der Fe-Film komplett amorph ist. Die Ga-reiche (4×2)-Rekonstruktion verhindert eine Diffusion und gewährleistet ein epitaktisches Wachstum der Fe-Schicht. Das MgO wurde auf der wohlgeordneten Fe(001)-Oberfläche aufgebracht und ist dort epitaktisch aufgewachsen. Die Fe-Oberfläche ist aufgrund der MgO-Anlagerung oxidiert, was sich in einer zwei Lagen dünnen FeO-Schicht zeigt. Der MgO-Film liegt in einer Steinsalzstruktur vor, bildet aber einen Gitterfehler in Form von leicht verschobenen Mg-Atomen aus. Diese Verschiebung ist sowohl für den dünnen als auch für einen dickeren Film vorhanden. Dies könnte durch das Substrat induziert sein, da die MgO/Fe Grenzfläche deutlich durch die Fe/GaAs Grenzstruktur beeinflusst wird. Chemische und strukturelle Veränderungen beeinflussen die magnetischen Eigenschaften des Mehrlagensystems. Daher wurden diese durch Magneto-optische Messung mittels T-MOKE untersucht. Die Spektren zeigen eine starke Reaktion des Eisens auf das externe magnetische Feld. Die Analyse der T-MOKE Daten ergab weder magnetischen Eigenschaften des GaAs-Substrats noch der dünne MgO-Schicht. Eine zusätzliche Hysterese Messung belegt die exzellenten ferromagnetischen Eigenschaften der Fe Zwischenschicht trotz der chemischen und strukturellen Veränderungen.

Contents

1 Introduction

Multilayer-systems consisting of ferromagnets, insulators, and semiconductors are in present interest in the research field of spin-electronics [1–4]. Within *spintronics* the spin of the electrons instead of their charge are used for representation and processing data. The degree of freedom of the electron spin substitutes the depiction of charge by holes and electrons [5]. This offers the possibility of non-volatile data storage.

The quantum-mechanics effects of spintronics devices are the **T**unnel **M**agneto **R**esistance (TMR) and the **G**iant **M**agneto **R**esistance (GMR). TMR was discovered by Michel Julière in 1975 observing a relative resistance change in a Fe/Ge-O/Co junction at $T = 4.2\,\mathrm{K}$ [6]. Junctions based on TMR consists of two ferromagnets (FM) separated by a thin insulator (I) layer. A schematic illustration of the TMR effect is shown in Fig. 1.1.

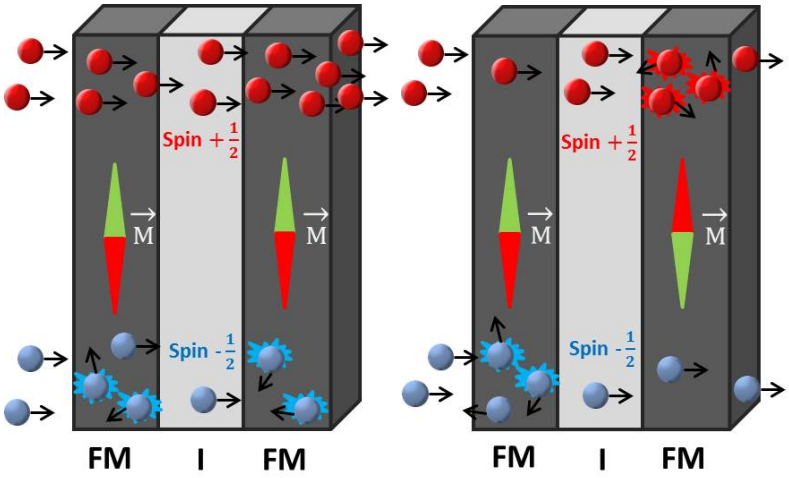

(a) parallel (b) anti-parallel

Figure 1.1: Schematic illustration of the TMR effect for the parallel (a) and anti-parallel (b) geometry of the magnetization $\vec{M}$. Depending on orientation spin-up and spin-down electrons are scattered differently at the FM/I interfaces.

The electrons may tunnel from one ferromagnet into the other if the insulator is thin enough. The electron spin is either $s = +\frac{1}{2}$ (up) or $s = -\frac{1}{2}$ (down). The magnetization $\vec{M}$ of the FM can be controlled by external magnetic fields. Depending on the mutual orientation of the magnetization the spin-up and spin-down electrons are scattered differently at the FM/I-interface. In the parallel geometry of $\vec{M}$ as shown in Fig. 1.1 (a) electrons with spin-up can travel unimpeded whereas the spin-down electrons are scattered at the FM/I-interfaces. If the magnetizations are anti-parallel as shown in Fig. 1.1 (b) the spin-down electrons are scattered at the first and the spin-up electrons at the second interface.
Basically, the GMR effect is similar to the TMR with a GMR-junction is consisting of two magnetic material being separated by a non-magnetic layer. It was discovered by Peter Grünberg and Albert Fert independently in 1988 and they received the Nobel Prize in 2007 [7,8]. They showed, that the electric resistance is depending on the mutual orientation of the magnetization direction of the magnetic layers. It is the strongest if magnetizations $\vec{M}$ are anti-parallel. Often, GMR-junctions consist of ferromagnets and semiconductors, with three basic requirements:

- a spin injection with consistent orientation from the ferromagnet into the semiconductor
- a transfer of the spins within the semiconductor and in case of need a manipulation of the spins
- a spin detection by a second ferromagnet

As an example for an GMR junction, a spin field effect transistor (spin-FET) by Datta and Das [9] is schematically shown in Fig. 1.2.

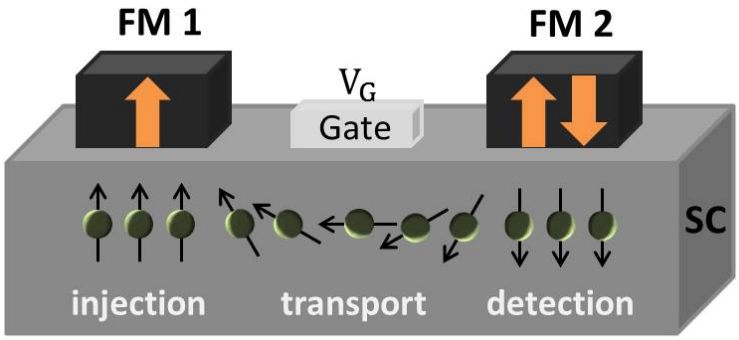

Figure 1.2: Schematic illustration of a ferromagnet-semiconductor GMR junction. The three spintronics steps of spin-injection, spin-transport, and spin-detection are marked. The spins are injected and detected using external magnetic fields via the magnetization of the ferromagnets FM 1 and FM 2. A manipulation of the electron's spin during the transport is provided by an additional gate electrode between the FM contacts.

Two ferromagnets (FM) are located on top of a semiconductor (SC) similar to source and drain of an FET, respectively. Controlled spin-injection and -detection becomes possible by using the orientation of the magnetization within the FM. The spin-polarized electrons travel from one spin-selective FM contact to the other. An additional voltage perpendicular to direction of movement causes a spin-orbit coupling, which conforms to an effective magnetic field perpendicular to the direction and the electric field. Due to this, the spin-polarized electrons precess. Only electrons with spins parallel to the spin-orientation can be detected at the drain-FM. Within the SC electron transport with defined spin-orientation should be possible over a sufficient large distance. Certainly, this was already achieved in 1998 by Hägele *et al.* [10], with spin polarized electron-hole pairs. The pairs were accelerates by circular polarized light and after a certain distance their spin polarization was optically detected by measuring the circular polarization of the recombination radiation.

Examples for junctions using the TMR and GMR effect are **M**agnetic **T**unnel **J**unctions (MTJ) [11] or **M**agnetoresistive **R**andom **A**ccess **M**emory (MRAM) devices [12]. They are widely used in hard disc drives or for sensing applications. Especially, the non-volatile data storage technique of MRAM offers a way for keeping data without permanent energy consumption. Therefore, all information can be kept on a circuit device and it is not necessary to transfer the information to an external memory. In fact, a computer using MRAM would be ready-to-operate directly after power-up.

One of the most favorable elements for TMR and GMR multilayer devices are the insulator Magnesium Oxide (MgO), the ferromagnet Iron (Fe), and the semiconductor Gallium-Arsenide (GaAs). Iron is a suitable ferromagnet, in fact it is the eponym of this type of magnetization. Magnesium oxide is an applicable insulator due to its great band gap of $\Delta = 7.8\,\mathrm{eV}$ [13]. The option of varying the band gap during the manufacturing process and a high electron transit frequency puts Gallium-Arsenide as a favorable semiconductor for TMR and GMR junctions.
Layer systems of MgO-Fe show a TMR effect even at room temperature [14] and are still favored in present research of MTJs [15–19]. The three mentioned requirements on GMR-junctions of spin-injection, -transfer, and -detection are all mostly fulfilled by Fe-GaAs layer systems [20, 21]. At room temperature a spin-injection from Fe into GaAs was first successfully shown by Zhu *et al.* in 2001 [22] with an efficiency of 2%.
In this thesis, a multilayer system consisting of MgO, Fe, and GaAs was prepared and investigated. Thereby, the focus was set on the material properties, because the knowledge of the initial characteristics of a system allows a precise preparation to optimize the efficiency of the spintronics effects. The chemical and electronic properties provide the information about bonds between the corresponding elements and especially the location of the bonds within the sample-system. The here investigated multilayer system MgO/Fe/GaAs(001) offers the possibility of a combination of the discussed effects for improving the spin-injection into the semiconductor for these electrons created by tunneling through an insulating barrier [23]. As mentioned before, both the TMR and the GMR effect arise at the interfaces of the layer systems. The structural properties of the interfaces have the strongest influence on the efficiency of the TMR and GMR effects [24–26]. Hence, this study focuses strongly on the two interfaces of the sample-system Fe/GaAs(001) and MgO/Fe(001). The photoelectron spectroscopy is chosen as the method of investigation, because it provides electronic, chemical, and structural information at the same time. Furthermore, it is very sensitive to solid surfaces, thin films, and their interfaces. Here, additional magnetic measurements are performed using magneto-optical spectroscopy. It allows a magnetic characterization of the three layer system and detection of possible magnetic differences due to structural changes. Especially, the ferromagnet and insulating properties of Iron and Magnesium oxide are indispensable in TMR/GMR-junctions.

Outline

The present thesis is organized as follows.
In section 2 the theoretical aspects of the used methods are introduced briefly. The physical main ideas of the photoelectron spectroscopy, diffraction, and magneto-optical spectroscopy are discussed with the view to the later considerations. The characteristics of a single XPS spectrum like spin-orbit coupling or chemical shift are described. The principles of scattering effects and the origin of the diffraction pattern are elucidated.
Section 3 addresses to the experimental set-up for the measurements. The vacuum chambers and their specific properties are discussed. Single components like the evaporator, sputter gun, and the LEED system are described. The sample holder for the photoelectron spectroscopy has some specific characteristics, which are elucidated. Finally, the synchrotron source DELTA, especially beamline 11, is introduced.
The preparation of the three layer system is part of section 4. The single elements are briefly introduced with the focus on their physical properties.
In section 5 the obtained results are discussed in detail. The interfaces were successively analyzed as shown by spectra and diffraction results. The magnetic results are discussed for the complete three layer system. Finally, the results for Fe/GaAs(001) without surface reconstructions are discussed.
Conclusively, section 6 summarizes the main results of this study and section 7 gives an outlook for possible further investigations.

2 Theoretical principles

The analysis of surfaces and interfaces of solid states imposes several requirements on the experimental methods. Most important are a surface or interface sensitivity, and the possibility of having access to electronic and chemical properties. Further, a method is requested, which allows a structure determination of epitaxial multilayer systems. In this thesis, **X**-ray **P**hotoelectron **S**pectroscopy (XPS) was used, because it combines all of these prerequisites. Incoming light excites core level electrons, which are emitted. Their amplitudes and thus the intensity distribution contains the requested information about the sample. The theoretical principles and characteristics of XPS are introduced in section 2.1.
Additionally, **X**-ray **P**hotoelectron **D**iffraction (XPD) provides detailed structural information of a sample. It is based on the effect that out-going electron waves contain structure information on the emitter environment. The experimental geometry and the analysis of XPD pattern are described in section 2.2.
A suitable tool to detect the magnetic properties of multilayer systems is the magneto-optical spectroscopy, which is based on magnetization direction dependent selection rules for a defined polarization state of the incoming light. In this thesis, the **T**ransversal **M**agneto-**O**ptical **K**err **E**ffect (T-MOKE) is used, because it allows an element selective investigation of the sample's magnetism. The theoretical ideas are described in section 2.3.

2.1 X-ray Photoelectron Spectroscopy

The fundamental idea of the photoelectron spectroscopy and diffraction is based on the photoelectric effect, discovered by Heinrich Hertz and Wilhelm Hallwachs in 1887 [27–29]. They observed that a metal plate loses its negative charges due to the irradiation with ultraviolet light. The theoretical explanation of this phenomenon was given by Albert Einstein in 1905 [30]. Einstein described the light energy being carried in discrete quantized packets, by matching the light particle *photon* to an energy of $E_{\mathrm{ph}} = h\nu$. Thereby, h describes the Planck constant and ν the frequency of the light.
In the course of the photoelectric effect an incoming photon is absorbed by a bonded electron by evolving its complete energy E_{ph}. Then, the electron may emit from the solid into vacuum, if sufficient energy was transferred. Thus, the photoelectric

equation by Einstein [30] is

$$E_{\mathrm{ph}} = E_{\mathrm{B}} + \Phi_{\mathrm{A}} + E_{\mathrm{kin}} \ , \tag{2.1}$$

where E_{B}, Φ_{A}, and E_{kin} denote the electron's binding energy, the work function, and the electron's kinetic energy, respectively. In words, the electron commonly named *photoelectron* has to overcome the element and orbital specific binding energy and the likewise element specific work function. The residual energy remain as the kinetic energy of the photoelectron. The work function defines an energy barrier between the vacuum level E_{vac} and the Fermi level E_F, which has to be overcome to dissolve and electron from the solid state via its surface [31].
The photoelectric effect is followed by relaxation processes within the atoms [32]. Due to the photoelectron emission an unoccupied energy state occurs. The hole is filled by an electron transfer from a shallow bond state E_i to the unoccupied state E_f. This process generates a photon with the energy

$$h\nu = E_i - E_f \ . \tag{2.2}$$

This photon can either be emitted as characteristic fluorescence radiation of the solid or it can be absorbed by another electron, which subsequently is emitted into the vacuum. The second process describes the Auger-Meitner Effect [33, 34]. The emitting electron is named *Auger-electron* and it is independent of the incoming photon energy. The Auger-Meitner Effect prevails for elements with atomic numbers $Z \leq 30$ and the fluorescence radiation has a high probability for elements with atomic numbers $Z \geq 60$ within the relaxation process. The photoelectric effect and the relaxation processes are illustrated in Fig. 2.1.
The surface sensitivity of the photoelectron spectroscopy can be controlled by the incoming photon energies, because it defines the resulting kinetic energies of the photoelectron. The probability an electron emitted from a solid state depends on the **I**nelastic **M**ean **F**ree **P**ath (IMFP) λ_e of electrons in matter [35]. This quantity denotes the average distance which electrons may travel through a solid until they are inelastically scattered. The intensity of photoelectrons being emitted from the depth d is given by the Beer-Lambert equation [36, 37]

$$I = I_0 \cdot e^{-d/\lambda_e} \ , \tag{2.3}$$

with I_0 denoting the primary intensity [38]. For pure elements the IMFP has been

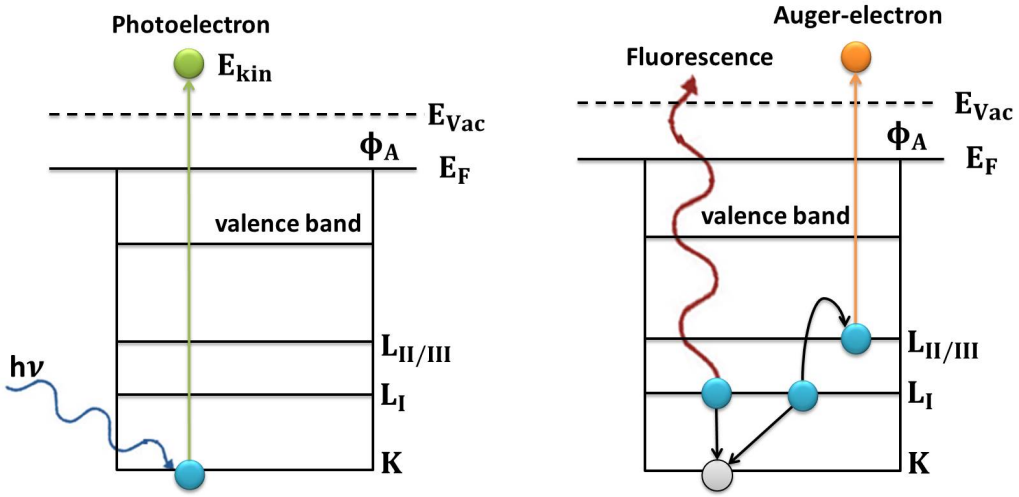

(a) Photoelectric effect (b) Relaxation

Figure 2.1: Illustration of the photoelectric effect (a) and the followed relaxation processes within the atom (b). An incoming photon is absorbed by a bonded electron (blue), which can emit into the vacuum (green). The hole (gray) will be occupied from another electron by evolving energy. This released energy either emits as fluorescence radiation (red) or as Auger-electrons (orange).

published as a semi-empiric formula depending on the electron's kinetic energy E_{kin} and the monolayer thickness a [39]

$$\lambda_e = \frac{2170}{E_{\text{kin}}^2} + 0.72\sqrt{a \cdot E_{\text{kin}}} \ . \tag{2.4}$$

Figure 2.2 shows schematically the behavior of the mean free path depending on the kinetic energy, which is a very good approximation for most of the inorganic samples. Therefore, this curve is commonly called *universal curve*.
Organic and low conducting samples have bigger mean free paths resulting a deviation of the universal curve to higher values. Furthermore, the curve has a minimum at approximately $E_{\text{kin}} \approx 30\,\text{eV} - 50\,\text{eV}$ and $\lambda_e \approx 5\,\text{Å}$. In the range of lower kinetic energies the IMFP is influenced by single-electron excitation. The excitation due to oscillations in electron density defines λ_e at high kinetic energies. The universal curve illustrates that the sensitivity for solid state surface measurements with photoelectron spectroscopy can be controlled by the incoming photon energy. Detected photoelectrons with kinetic energies in the range of 50 eV can only be emitted by surface layers, due to their small inelastic mean free paths.

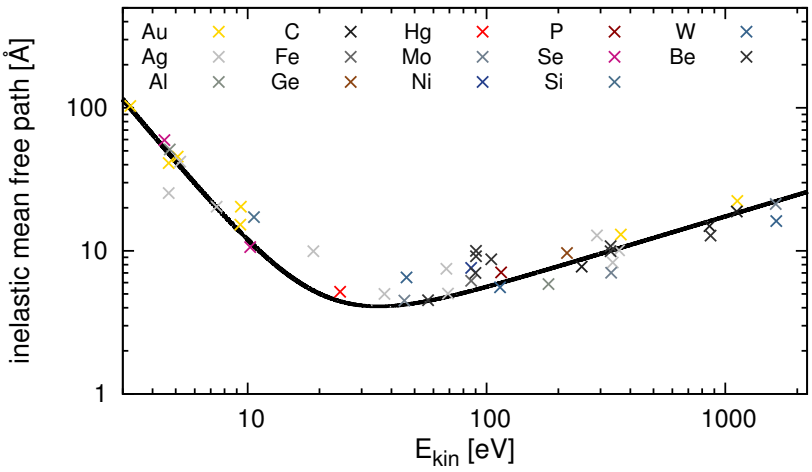

Figure 2.2: Illustration of the empirical behavior of the inelastic mean free path for electrons in matter depending on their kinetic energy. The universal curve (black line) as well as several values for different elements (color crosses) are shown.

2.1.1 XPS spectra

The binding energy E_B can be measured indirectly by recording a spectrum of the photoelectron intensities depending on their kinetic energies. For constant photon energies the binding energy E_B can be calculated easily as clarified by the photoelectric equation 2.1. Common measuring instruments allow to identify the binding energy of the single electron state correct to a milli-electron volt. Thereby, the incoming light has to be monochromatic. Otherwise, a difference in the excitation energy or wavelengths causes different maxima of the intensity for a single energy state.

A XPS survey scan records all elements located within the sample, if the excitation energy is high enough. Due to the energy-dependent cross section of the sub-shells, various elements show different intensities of the photoelectrons. Only Hydrogen and Helium cannot be detected due to their small cross sections. These cross sections can be found in charts like Reference [40]. A typical survey spectrum of the three layer system MgO/Fe/GaAs is shown in Fig. 2.3.

Further phenomena may cause additional intensity maxima within a survey scan and will be discussed briefly.

In the low energy range a strong increase of the intensity occur due to secondary electrons. They originate either from low bonded energy states excited by the emitting photoelectrons or are inelastically scattered electrons.

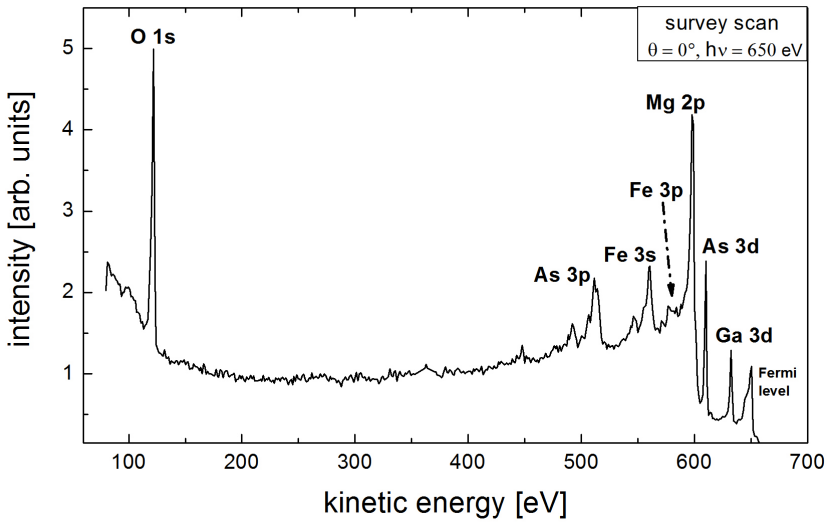

Figure 2.3: A generic photoelectron-spectrum. All elements located in the sample are denoted due to their specific energy positions.

Satellite signals are the result of a sudden change in the effective charge due to the loss of core electrons. Two types of satellites can be distinguished, the *shake-up* and *shake-off* lines. The first type is the result of the interaction between the emitting photoelectron with a valence electron by exciting it to a higher energy level. Consequently, the photoelectron energy is reduced and a satellite structure arise a few electron-volt below the main XPS peak. In the second case the valence electron is ejected from the ionized atom completely. These shake-off lines may appear as a broadening of the main signal or contribute to the background only. Signals from emitted valence band electrons occur in the high energy range due to their weak binding energies.

Clean surfaces of metals or semiconductors enable to detect a specific feature, the *plasmon-peaks*. The outgoing photoelectrons may excite collective oscillations of the quasi free-electron gas in the conduction band, the so-called *plasmons*. Thereby, the discrete loss of the electron energy conforms to the extrinsic plasmon energy. The refill of the hole due to the photoelectric effect from the Fermi-sea instead the atom itself originate intrinsic plasmons.

The signals resulting from the Auger-electrons are characterized by the involved energy levels. The KLL-Auger-line for example results from the $L_{\mathrm{I}}L_{\mathrm{II,III}} \rightarrow K$ subshell transition. These signals are independent on the incoming photon energy, so they are found at a constant kinetic energy positions within different survey scans.

In this thesis only the plasmon peaks of the GaAs-substrate are visible supplementary to the main XPS signals.
Besides this, the line shape of one core level signal may be subjected to further phenomena, which are described below.

spin-orbit coupling

A single photoelectron signal may split into multiplets due to the interaction of the orbital angular momentum and the spin of the electron, the so-called **S**pin-**O**rbit **C**oupling (SOC). The eigenstates of the electron wave function $|\Psi\rangle = |n, l, m, s\rangle$ are described by four quantum numbers. The principal quantum number n describes the energy shell of an atom and the azimuthal quantum number l depicts the sub-shell and magnitude of the orbital. The magnetic quantum number m characterizes the specific orbital of this sub-shell and yields the spatial orientation of the electron angular momentum. The spin projection quantum number s describes the spin of the electron within that orbital. The magnetic moment and the spin of the electrons within an atom interact additive:

$$S = \sum_{\mu} s_{\mu} \tag{2.5}$$

$$L = \sum_{\mu} l_{\mu} \ . \tag{2.6}$$

The final states are given by the total-angular momentum J yielded by the LS-coupling [31]:

$$J = L \pm S \ . \tag{2.7}$$

The electron spin can either be parallel or anti-parallel to the orbital angular momentum. Therefore, two states of the total-angular momentum exits, $J = L + S$ and $J = L - S$. In the second case, the kinetic energy of the photoelectrons is smaller. If unpaired electrons exist in the valence band a multiplet splitting occur. The signals of atom-levels with an azimuthal quantum number of $l \geq 1$ split into a doublet. The quotient of the order of degeneracy $(2J + 1)$ indicates the height ratio of the resulting doublets. A p-level for example splits into $p_{1/2}$ and $p_{3/2}$ states and

has a height-ratio of [41]:

$$h_{LS} = \frac{2 \cdot \frac{1}{2} + 1}{2 \cdot \frac{3}{2} + 1} = 0.5 \ . \tag{2.8}$$

Fig. 2.4 shows generic the XPS $3p$ and $2p$ core level signals of Arsenic (As) and Iron (Fe), respectively.

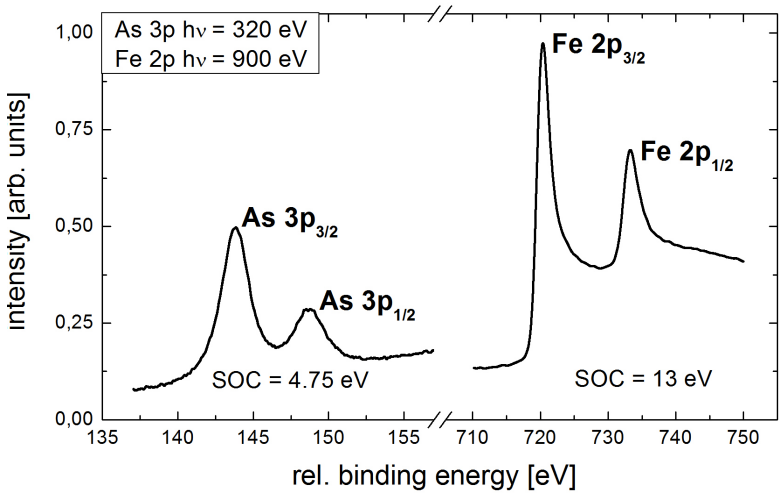

Figure 2.4: XPS core level signals of As $3p$ and Fe $2p$. Due to the strong SOC the $p_{1/2}$ and $p_{3/2}$ signals are sharply separated. The height ratio of $h_{LS} = 0.5$ for the p-orbital are clearly visible.

Due to the strong spin-orbit coupling of SOC = 13 eV of the Fe $2p$-signal, two sharply separated maxima of the intensities corresponding to the Fe $2p_{1/2}$ and Fe $2p_{3/2}$ doublet occur. In the case of As $3p$ the energy shift caused by the spin-orbit coupling is SOC = 4.75 eV resulting likewise in two separable maxima. Certainly, other element-orbitals with lower couplings originate signals, where the multiplets overlap. The precise value of the energy splitting caused by the SOC is a function of the atomic number, the shell, and the orbital angular momentum of an element [42].

chemical shift

The atomic number and the distance that its valence electrons reside from the charged core of an element affect an atoms electronegativity. Within a chemical bonding the more electronegative element attracts the binding electrons towards itself. As a consequence, the relative atomic number of its binding partner raises

and the binding energies of the electrons near the core increase, which in turn reduce the kinetic energy of the emitted photoelectrons. This phenomenon becomes apparent in an XPS spectrum by shifted maxima of the photoelectron intensities. Therefore, this phenomenon is named *chemical shift*. In Fig. 2.5 the chemical shift of the 1*s*-signal of Carbon (C) of the molecule ethyl trifluoroacetate is shown.

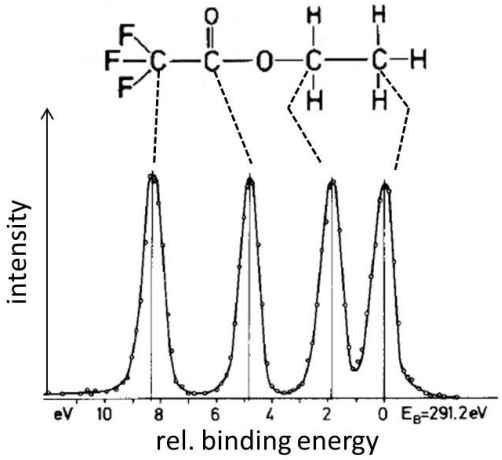

Figure 2.5: Different intensity maxima of the C 1*s*-signal in ethyl trifluoroacetate $FCH_2COOC_2H_5$ resulting from the different electronegativities of the binding partners. This figure is extracted from References [43, 44].

Depending on the value of the electronegativity, several maxima of the C 1s-signal occur. Hydrogen (H) is less electronegative than Oxygen (O), which resulting in a stronger shift the more Oxygen atoms are bonded to the Carbon. One of the most electronegative elements is Fluorine (F). Hence, the C 1*s*-signal of the C-F-bond is shifted about $\Delta E \approx 8\,\mathrm{eV}$ towards higher electron binding energies with regard to the C-H-bond. The phenomenon of the chemical shift can result in additional components to a bulk signal of a single XPS-signal and provides the chemical information about the sample. A separation between surface, thin films, and bulk is ambiguous and depends often on the application and discipline [45]. In common usage, the surface is related to $1-3$ atomic layers and thin films to thicknesses of $0.2\,\mathrm{nm} - 1\,\mu\mathrm{m}$ [31]. The remainder of the solid is referred to the bulk material.

2.1.2 Analysis of XPS-signals

As discussed in the previous chapter, a single XPS signal may consist of different components due to the chemical shift and splitting into multiplets due to the spin-orbit coupling. Thus, information about the sample and its interfaces can be ob-

tained by measuring high resolution spectra and fit them with a suitable function. To deduce the information requested, the kinetic energies of the components have to be known.

In a first step the background consisting mostly of secondary electrons must be removed from the spectrum. In this work the Shirley function was used to reduce the spectra to the photoelectron intensity only [46]. The background is monotonically non-increasing and has an inflection point at the maximum of the XPS signal. At the boundaries the Shirley-function has the same value as the intensity of the signal itself. This is schematically illustrated in Fig. 2.6.

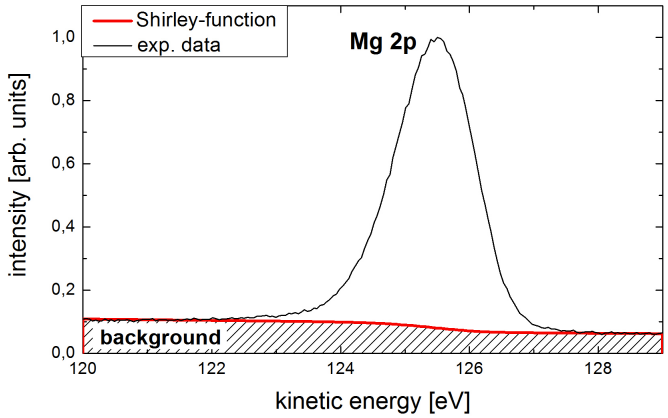

Figure 2.6: Illustration of the Shirley-background using the example of the Mg 2*p* high-resolution XPS signal.

A XPS signal should conform to a δ-peak, but it is widened due to the finite lifetime of core-holes and excited states. This *natural broadening* results from the energy-time uncertainty relation and can be described by a Lorentz-function. Likewise, a XPS signal is broadened by the Gaussian influence of the measure equipment, e.g. a finite resolution. Hence, a convolution of Gaussian and Lorentz function, the Voigt-profile, is basically used for a fitting procedure. In this work, the analysis of the XPS spectra reveals that the Gaussian influence of the experimental set-up dominates the form of the signals. Therefore, the Gaussian function

$$G(E) = \sum_{\mu} \left[A_\mu \exp\left(\frac{1}{2} \left[\frac{E - E_\mu}{\sigma_\mu} \right]^2 \right) + h_{\mathrm{LS}} A_\mu \exp\left(\frac{1}{2} \left[\frac{E - (E_\mu - f_{\mathrm{LS}})}{\sigma_\mu} \right]^2 \right) \right] \tag{2.9}$$

is applied for the least squares fits. Thereby, A_μ denotes the complex amplitude, and σ_μ the **F**ull **W**idth **H**alf **M**aximum (FHWM). The parameters h_{LS} and f_{LS} include the height ratio and the energy shift caused by the spin-orbit coupling. The number of terms of the sum is depending on the number of components within a XPS signal due to possible chemical shifts. The kinetic energy position of each component is given by E_μ. Photoelectron-spectra of metals show a lightly asymmetric line shape due to a distribution of unfilled one-electron levels. These are available for shake-up like events following core electron emission. Instead of a discrete structure like the shake-up satellites an asymmetric line shape of the main peak occurs. In this thesis the signal of the metal Iron was fitted using the Gaussian function (2.9) due to the dominance of the Gaussian extension. A short discussion of this Gaussian dominance even for a metal signal is given in the Appendix A.1. The high-resolution spectra are fitted using OriginPro 8.5 based on the Levenberg-Marquardt-Algorithm [47].
To identify the components within a signal related to atoms in subsurface, surface, or interface regions two spectra are recorded at different emission angles. As displayed in Fig. 2.7 the effective depth from which the photoelectrons emit depends on the polar angle θ. It describes the angle between the surface normal and the detector normal. In this example foreign atom are located at the surface of a Ga-sample. This is displayed obvious by the increase of a shoulder within the spectrum at the surface sensitive position $\theta = 60°$. For decreasing polar angles the effective and mean profile depths assimilate and the Ga bulk-signal dominates the spectra. Certainly, spectra of one single XPS signal recorded at different angles should only be varying in the intensities, which have to be minded within the fitting procedure.

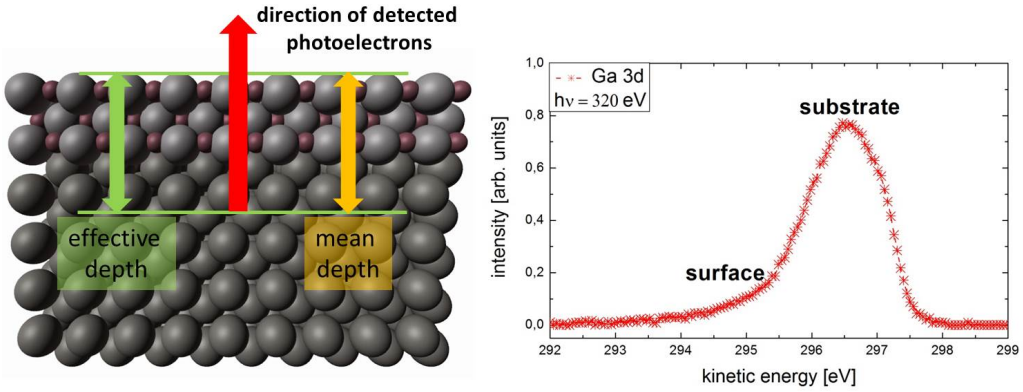

(a) $\theta = 0°$

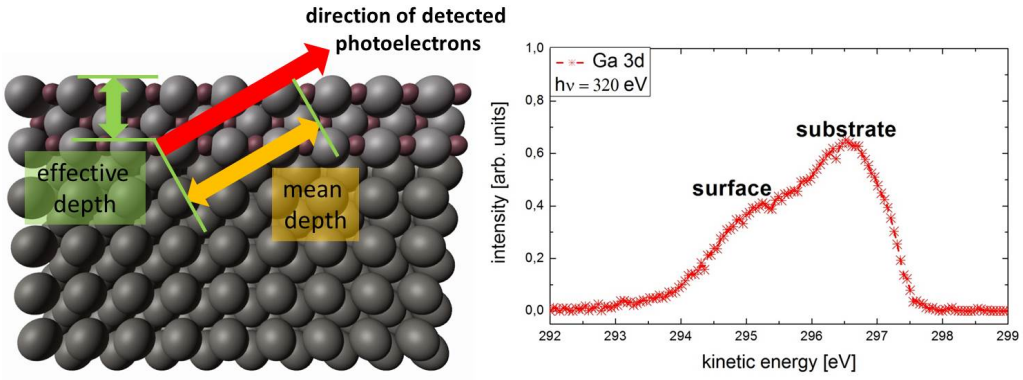

(b) $\theta = 60°$

Figure 2.7: Illustration of the dependence of a core-level XPS-signal on the sample position. The resulting profile depth is shown for normal emission of $\theta = 0°$ (a) and the surface sensitive polar angle $\theta = 60°$ (b).

The comparison of spectra recorded at different polar angles allows an identification of the elements located in different regions of the sample. Furthermore, it verify if the sample is clean, because foreign atoms of the environment attach only to the surface layers.

2.2 X-ray Photoelectron Diffraction

The dependence of the photoelectron intensities on the emission angles was first observed in 1970 by Kai Siegbahn *et al.* using a Sodium Chloride single crystal [48]. His observed anisotropic modulations of the intensities resulted from scattering effects of the emitting photoelectrons at neighboring atoms. In 1974 Ansgar Liebsch

recognized that the measured modulations provide information about the local environment of the emitting atom [49].

A crystalline sample shows symmetric modulation of the photoelectron intensities, which can be attributed to the symmetries of the sample structure. If the movement of the photoelectrons through the solid is considered as waves, these modulations can be explained by the interference of non-scattered and scattered waves. In the case of photoelectron diffraction the parts of inelastic scattering processes are neglected, because inelastic scattered electrons raise the background of the spectrum only. Therefore, the scattered and non-scattered electron waves have the same wavelength and the intensity modulation is given by the superposition of the primary wave $\Psi_0(\vec{k})$ and the sum of all scattered waves $\Psi_j(\vec{k})$:

$$I(\vec{k}) = \left| \Psi_0(\vec{k}) + \sum_j \Psi_j(\vec{k}) \right|^2 . \tag{2.10}$$

Below, the theory of single scattering is used to describe the physical principles of the **X**-ray **P**hotoelecton **D**iffraction (XPD). Certainly, the theory of multiple scattering has to be minded for a suitable analysis of the intensity modulations and is explained in detail in Reference [50].
The scattering process of the emitted photoelectrons is schematically shown in Fig. 2.8.
In the single scattering case the scattered waves $\Psi_j(\vec{r})$ are given by

$$\Psi_j(\vec{r}) = \Psi_0(\vec{r_j}) \cdot f_j(\vec{k}) \cdot \frac{e^{ik|\vec{r_j}-\vec{r}|}}{|\vec{r_j}-\vec{r}|} , \tag{2.11}$$

$$\text{with } f_j(\vec{k}) = |f_j(\vec{k})| \cdot e^{i\Delta\phi(\vec{k})} . \tag{2.12}$$

The scattered wave is described by $\exp(ik|\vec{r_j}-\vec{r}|)$ and the term $\frac{1}{|\vec{r_j}-\vec{r}|}$ ensures the conservation of energy. The primary wave is given by $\Psi_0(\vec{r_j})$. The complex item $f_j(\vec{k})$ describes the scattering factor, which includes the amplitude $|f_j(\vec{k})|$ and the phase $e^{i\Delta\phi(\vec{k})}$ of the scattered wave. Thus, the intensity modulation $I(\vec{k})$ in equation (2.10) is a function of the positions of the atoms in the local emitter environment $\vec{r_j}$.
The amplitude and the phase depend on the modulus and direction of the wave vector $\vec{k}$ and are not isotropic. The modulus of $\vec{k}$ is proportional to $\sqrt{E_{\text{kin}}}$ and is

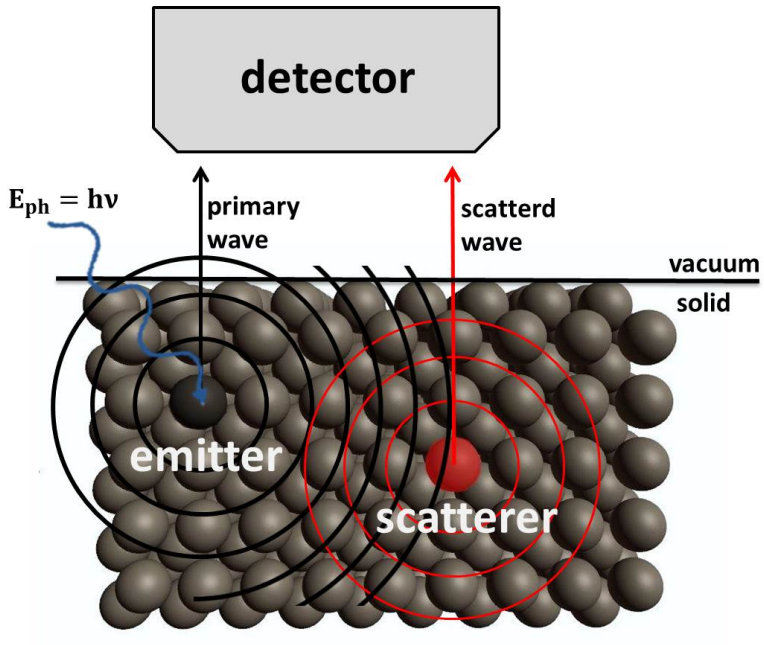

Figure 2.8: Illustration of the photoelectron diffraction process. The interference of the primary wave (black) and scattered wave (red) causes intensity modulations of the spectra at the detection point.

vectored from the emitter towards the detector. Furthermore, the scattering factor is element specific. This phenomenon is illustrated in Fig. 2.9 for Nickel (N) and Oxygen (O) at different kinetic energies.
If the kinetic energy is $E_{\text{kin}} \geq 500\,\text{eV}$, the photoelectrons are focused strongly in forward direction. The maxima of high-energy diffraction pattern are distinct and located in a small solid angle. They provide information about the structure environment between the emitter and the detector. Information about the structure behind the emitter can be obtained by backward scattered waves. The scattering in backward direction becomes important for energies $E_{\text{kin}} \leq 300\,\text{eV}$. Due to the element specific scattering effects XPD pattern using low energies includes, beyond the atom positions, information about the elements in the local emitter environment.
The photoelectron diffraction is based on the photoelectron spectroscopy and thus allows an independent investigation of the local structure of various elements within one sample. It is possible to identify different structures for one single element due to the chemical shift discussed in chapter 2.1.1. Therefore, XPD is an excellent tool for structure investigations of the interface and by using suitable photon energies of the surface of multilayer systems.

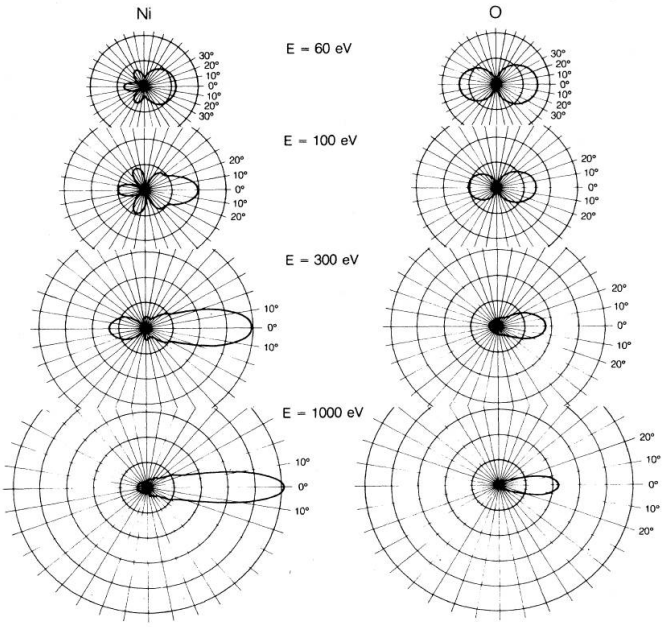

Figure 2.9: Illustration of the dependence of the scattering factor on the element and energy using the example of N and O. The figure is taken from Reference [50].

2.2.1 XPD pattern

In order to measure a XPD pattern two modes may be applied, the angle-resolved mode and the energy-resolved mode. In the first case, the energy is kept constant under varying the emission angle, whereas in the second case the energy is varied by constant emission direction. In this thesis, the angle-resolved XPD geometry was applied. A spectrum of one single XPS signal is recorded at various sample positions. Figure 2.10 illustrates schematically the measuring process of the angle-resolved mode. The emission angles describe the sample position in polar and azimuth direction with regard to the detector. The polar angle θ is defined as the angle between the surface normal and the vector between sample and detector. The rotation around the surface normal is described by the azimuth angle φ. Within the XPD measurements both polar and azimuth angles were changed, with a polar-angle range of $0° \leq \theta \leq 60°$ and an azimuth-angle range of $0° \leq \varphi \leq 360°$. The step-width increment was set to $\Delta\theta = 2°$ and $\Delta\varphi = 1.8°$. This results in approximately 6000 individual XPS spectra, recorded in the hemisphere above the sample as shown in Fig. 2.10 (a).

In order to detect the structural information of the sample, the correct intensity of the XPS signal is needed. The intensity I is given by the area under the peak

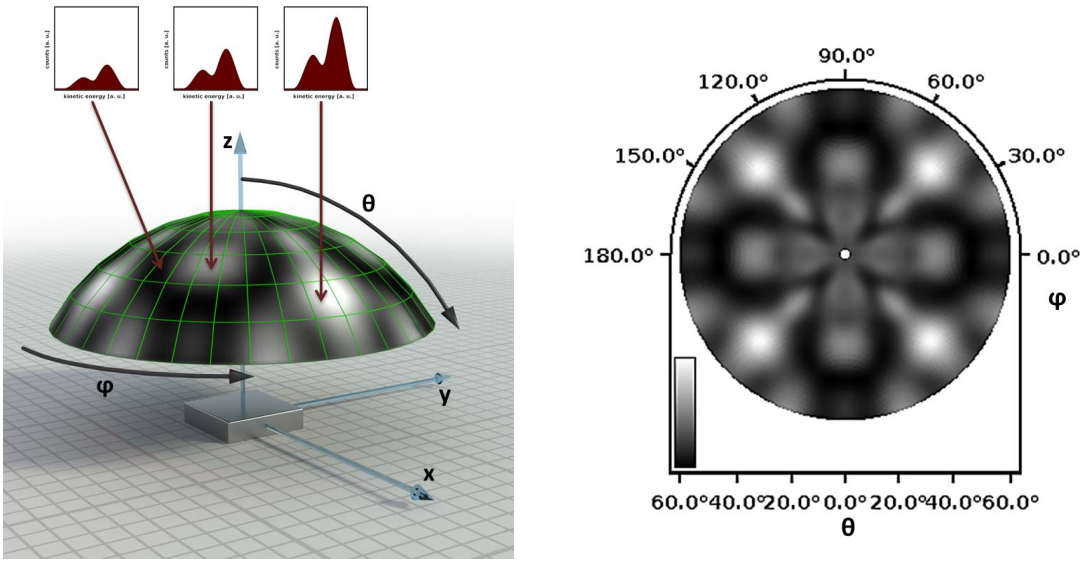

(a) Angle-resolved geometry (b) Polar-plot

Figure 2.10: Geometry of the XPD pattern acquisition in the hemisphere above the sample (a) and the resulting color-coded polar plot (b). Figure (a) was made by [51].

less the background and can be calculated using numerical integration. Within the illustration and analysis of the XPD pattern the normalized sum of deviation squares is used. This *anisotropy function* restrict the measured intensity to its modulated part by offset the decrease of the intensity for increasing angles and the leap of intensities due the injections using synchrotron radiation (see chapter 3.1.5). The anisotropy function $\chi(\theta, \phi)$ is defined as

$$\chi(\theta, \phi) = \frac{I(\theta, \phi) - I_0(\theta)}{I_0(\theta)} \ , \tag{2.13}$$

where $I(\theta, \phi)$ and $I_0(\theta)$ denote the intensity at the emission direction (θ, ϕ) and the average intensity at emission direction (θ), respectively.
The experimental data are transferred to a two dimensional color coded polar plot shown in Fig. 2.10 (b). In this example high intensities are depict in white, mean intensities in grey and low intensities in black. This XPD pattern contains all structural and chemical information about the local emitter environment of one element within the sample.

2.2.2 Analysis of XPD pattern

The real space structure cannot be directly recalculated from the experimental XPD pattern due to the strong anisotropy of the phase and amplitude of the scattered waves. The analysis is carried out by simulations of atomic structure models and comparison between simulated and experimental data. In this work, the full **M**ultiple **S**cattering code for low energy **PH**otoelectron **D**iffraction program (MSPHD) is used for the simulation of XPD pattern. A detailed explanation of this code is given in References [52–56].
In a first step an atomic structure model is build based on a possible structure conceived for the sample. This *cluster* depends on the sample system and is size limited due to the small electron mean free paths in the considered energy range of $E_{\mathrm{kin}} = 30\,\mathrm{eV} - 350\,\mathrm{eV}$. Corresponding to this structure a diffraction pattern is simulated. Generally, the simulation can be described by four steps [52]:

1 A cluster potential is calculated using the muffin-tin approximation.

2 The system symmetry is taking into advantage by symmetrized basis functions, which reduce the size of the scattering matrix and describe the final state wavefunction.

3 Computation of the complex phase shifts, electric dipole matrix elements, and solving the multiple scattering through inverting the scattering matrix.

4 Calculation of the angular cross-section $\frac{d\sigma}{d\hat{k}}$, which is proportional to the photoelectron intensity.

Thereby, parameters like the kinetic energy, the scattering radius, or the maximum angular momentum cutoff for the MSPHD simulations are set as constants. In this thesis, the kinetic energy is given by the experimental pattern, the radius depends on the cluster, and the angular momentum is set up to $l_{\mathrm{max}} = 6$.
For a quantitative comparison between experimental and simulated XPD pattern the **R**eliability-factor (R-factor) is used, which is defined as

$$R = \frac{\sum_{\mu}(\chi_{\mathrm{exp}_{\mu}} - \chi_{\mathrm{sim}_{\mu}})^2}{\sum_{\eta}(\chi^2_{\mathrm{exp}_{\eta}} - \chi^2_{\mathrm{sim}_{\eta}})} \ . \tag{2.14}$$

In this definition [57] an R-factor of 0 correspond to exact accordance, whereas an R-factor of 2 describe a totally anti-correlated system. A very good agreement is

given by R-factors of $R \leq 0.1$.
The atomic cluster has to be varied until the required agreement is achieved. Thus, the simulations are performed for a large number of possible atom positions, which causes a high numerical effort. Therefore, a **G**enetic **A**lgorithm (GA) is applied, which avoids local minima of the R-factor. The GA uses affine transformations $\vec{r}' = \underline{\underline{A}}\vec{r} + \vec{b}$ to vary the starting structure from the atom position $\vec{r}$ to $\vec{r}'$. The matrix $\underline{\underline{A}}$ and the vector $\vec{b}$ represent the respective transformation process. These can be adapt to a single atom, a group of atoms, or the whole cluster. In this work, three processes for varying the structure are applied:

$$\text{translation} : \vec{r}'_T = \mathbb{1}\vec{r} + \alpha \cdot \vec{T} \tag{2.15}$$

$$\text{rotation} : \vec{r}'_R = \underline{\underline{R}}(\alpha) \cdot \vec{r} \tag{2.16}$$

$$\text{scaling} : \vec{r}'_S = \underline{\underline{S}}(\alpha) \cdot \vec{r}\,. \tag{2.17}$$

The gene α describes a floating-point number. In the case of transformation α corresponds to the modulus of the translation vector $\vec{T}$, for rotation it is the rotation angle within the rotation matrix $\underline{\underline{R}}$, and in the case of scaling it serve as the scaling factor in the scale matrix $\underline{\underline{S}}$ [58]. The procedure of the genetic algorithm is illustrated schematically in Fig. 2.11.

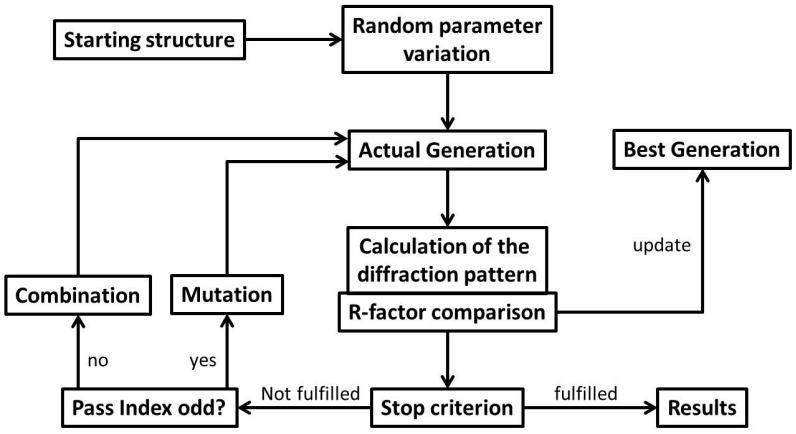

Figure 2.11: Illustration of the procedure of the used genetic algorithm.

The starting structure model and required variations are inputted to the program. This generates various clusters named *Generation*, which are simulated and analyzed using the R-factor. If the stop criterion is fulfilled the algorithm is completed by printing the best result. Otherwise new generations are built by a combination or mutation of the previous best simulated pattern. These are updated in every

generation. The detailed description of the used genetic algorithm and general information are given in [58–60].

2.3 Magneto-Optical Kerr Effect

In 1845 Michael Faraday detected a rotation of the polarization vector of linearly polarized light by transmit trough a lead glass, which was located in an external magnetic field [61]. About 31 years later John Kerr observed that linearly polarized light is reflected from a pole of a magnet by a rotation of the plane of the polarization [62]. In other words, Kerr discovered the analogon of the Faraday-Effect in reflection, the **M**agneto-**O**ptical **K**err **E**ffect (MOKE).

In general, the magneto-optical Kerr effect describes the alteration of the light polarization reflected from a ferromagnetic medium [63].
The Kerr effect arises from the simultaneous occurrence of spin-orbit coupling and exchange interaction in a ferromagnet. The incidental photons generate selected intra- and inter-band transitions within the atoms. The probability of an electron transition depends on the initial and final state as well as on their density of states [64]. Further, due to the fact that for such a transition the spin and the angular momentum are conserved quantities, several selection rules have to be adhered. These apply

$$\Delta s = 0 \tag{2.18}$$

$$\Delta l = \pm 1 \tag{2.19}$$

$$\Delta m = 0; \pm 1 \ , \tag{2.20}$$

with the quantum numbers of the spin s, the angular momentum l, and the magnetic quantum number m. The angular momentum of a photon is $l_{\mathrm{ph}} = \pm 1$ for circular polarization and $l_{\mathrm{ph}} = 0$ for linear polarized light. Depending on the orientation of the samples magnetization different transitions of the magnetic quantum number are possible [65]. The example in Fig. 2.12 illustrates a $p \rightarrow d$ transition.
Due to the spin-orbit coupling Δ_{SOC} the p-orbital splits into the $p_{1/2}$ and $p_{3/2}$ (see section 2.1.1). In turn, the degeneration is further lifted due to the exchange interaction Δ_{ex}, resulting in six energetically distinguishable p core levels. Furthermore,

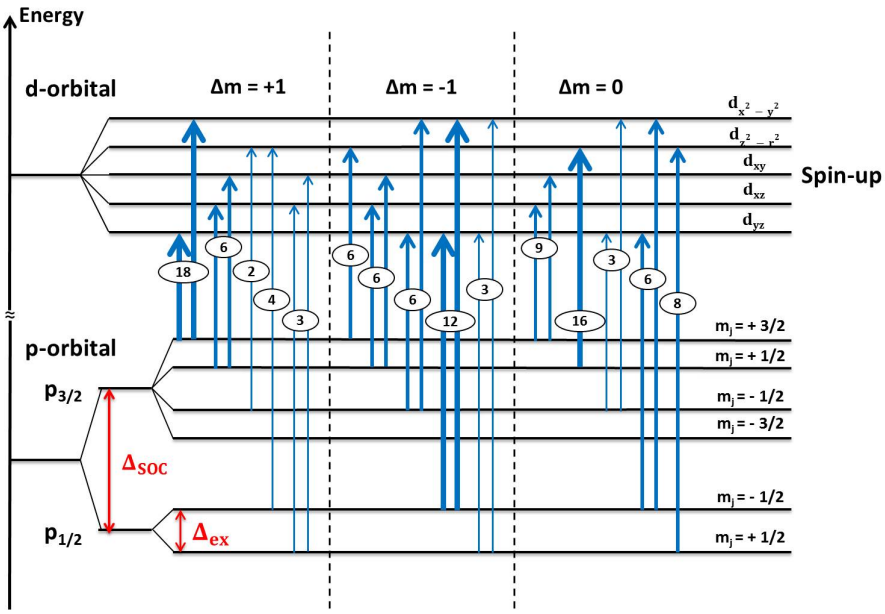

Figure 2.12: Schematic illustration of the possible $p \rightarrow d$ transition for the spin-up geometry. Due to the spin-orbit coupling and exchange interaction six individual p-core level states are distinguishable. The numbers indicate the relative transition probabilities. This figure is based on Reference [66].

the energy states of the valence electrons within a metal are energetically shifted for spin-up and spin-down electrons. In the example of Fig. 2.12 the transition into the d-orbital are illustrated for the spin-up geometry only for reasons of clarity and comprehensibility. A detailed description of the theory of MOKE and magneto-optical spectroscopy can be found for instance in References [66, 67].

In this thesis, the magnetic measurements were performed by means of magneto-optical spectroscopy using the **T**ransversal **M**agneto-**O**ptical **K**err **E**ffect (T-MOKE). It is based on the discussed magnetization direction dependent selection rules and transition probabilities for a defined polarization state of the incoming light. Hence, a suitable measure condition allows a detection of electronic and magnetic properties of the sample. The experimental geometry of T-MOKE is illustrated in Fig. 2.13. The magnetization of the sample is perpendicular to the plane of incidence, whereas the electric filed of the incoming linear p-polarized light is parallel. The intensity after the reflection at the sample is dependent on the two opposite orientations of the magnetization $M^{\pm}$. If the incidence is stripping or the angle is $\alpha = 90°$, the T-MOKE signal disappears. Certainly, a rotation of the polarization does not occur. To determine the magnetic properties of a sample using T-MOKE, two reflectivity spectra at the element specific edges for various orientations of the magnetic field

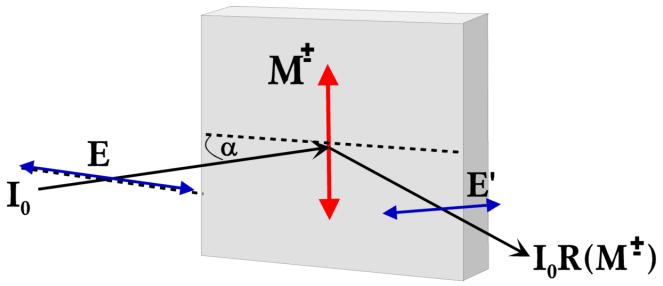

Figure 2.13: Illustration of the experimental geometry of T-Moke. The linearly polarized light incides to a transversally magnetized sample and causes a change in the reflected intensity. This picture is taken from Reference [68].

are recorded. The relative reflectivity $R(B)$ is measured by switching the sign of the magnetization, which leads to two different reflectivity spectra [68].
The T-MOKE asymmetry A is defined as the normalized difference of the relative reflectivity:

$$A = \frac{R(M^+) - R(M^-)}{R(M^+) + R(M^-)} \ . \tag{2.21}$$

Thereby, $R(M^+)$ describes the reflectivity in the case of the parallel orientation of the magnetization to the cross product of the incoming and out-going electric fields. Accordingly, $R(M^-)$ defines the anti-parallel geometry. The T-MOKE asymmetry provides the magnetic information about the sample and it becomes stronger at angles around the Brewster-angle [69]. Further hysteresis measurements allow an analysis of the magnetic response of each individual element within an external field. A further detailed description of the measuring conditions and explanations of T-MOKE are given in References [65–67].

3 Experimental aspects

A detailed analysis of the surfaces of solid states requires a clean sample. This implies that no contaminations from ambient air like Carbon or Oxygen are located at the surface. Therefore, the preparation and the measuring are carried out in a **U**ltra **H**igh **V**acuum chamber (UHV) with a base pressure of $p = 5 \times 10^{-11}$ mbar. In this pressure range 1% of the surface will be covered by residual gas molecules in $t = 100$ h, whereas at air pressure the contamination needs $t = 10^{-11}$ s only [31]. All measurements were performed at room temperature.
The used UHV chamber equipment includes a manipulator, a spectrometer, a channeltron detector, a sputter gun, electron beam evaporators, and a LEED-system. All of these components and the characteristics of the sample holder for XPS/XPD measurements are described in detail in the following chapters. Furthermore, the UHV chamber used for the T-MOKE investigation and the synchrotron source DELTA are introduced.

3.1 Experimental set-up

The XPS and XPD measurements were performed in the UHV-chamber illustrated schematically in Fig. 3.1. The small chamber is used for sample transfer into the main chamber by using a linear transfer rod. This submits a sample exchange without a break of the vacuum. The manipulator enables movements of the sample in every spatial direction, as well as in azimuthal and polar angle rotations. This movement can be controlled manually or with a computer by three individual motors.

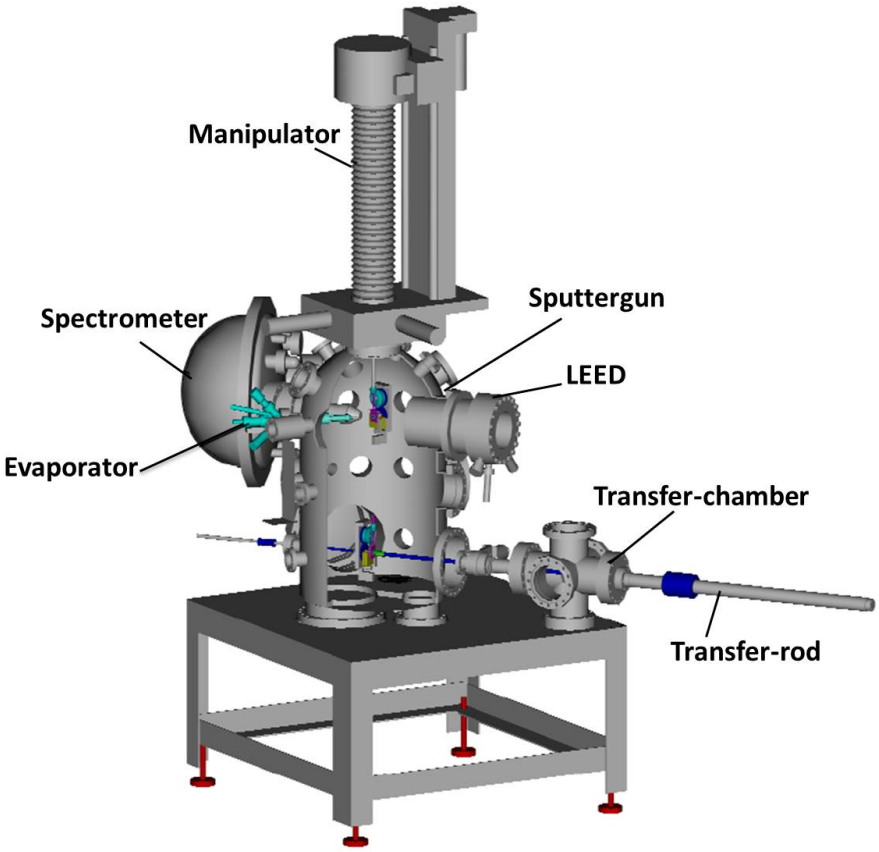

(a) UHV chamber

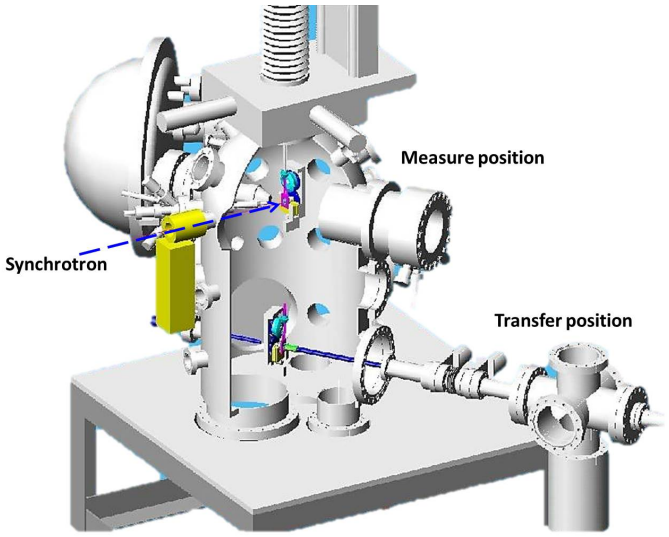

(b) Sample positions

Figure 3.1: Schematic illustration of the UHV chamber used for XPS and XPD investigations (a). With the help of the manipulator the sample (magenta) can be located at every requested position (b).

The detection elements consists of a **C**oncentric **H**emispherical **A**nalyzer (CHA) and a channel electron multiplier detector (short *channeltron*). The CHA spectrometer and the channeltron detector are schematically illustrated in Fig. 3.2.

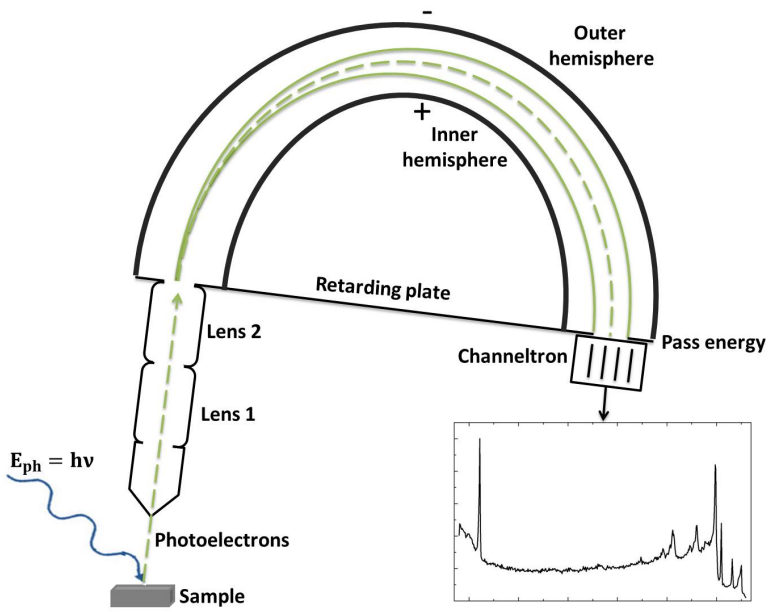

Figure 3.2: Illustration of the detection element consisting of a CHA spectrometer and a channeltron detector.

The photoelectrons emitting from the sample are focused by a lens system and retarded afterwards to the adjusted pass energy of the spectrometer. Thereby, the retarding field is varied in order to scan different kinetic energies. Photoelectrons which are too slow or too fast get sidetracked to the inner or outer hemisphere, respectively. On leaving the CHA the electrons pass a thin semiconducting plate consisting of smaller channel plates with distances of about $D = 10\,\mu$m. These channel plates are 10° tilted with respect to the plate axis to ensure that the electrons hits the wall of the channel plates several times. Every collision emits further electrons, which are accelerated again. This electron avalanche is counted by an electronic part depending on their kinetic energy. These counts are proportional to the intensity of the emitting photoelectrons within a XPS spectrum.
The T-MOKE measurements were carried out in the *XMAPS* chamber shown in Fig. 3.3. The incoming light passes a set of pinholes, filters, and monitoring devices. The sample is located in the middle of the magnetization device *TetraMag* [70] placed on a two circle goniometer. The light reflected at the sample can be detected using

photo-diodes or photo-multipliers. The polarization state of the light can either be analyzed by a Rabinovich detector or a Wollaston prism based detector. A further detailed description of the experimental T-MOKE set-up can be found in [67].

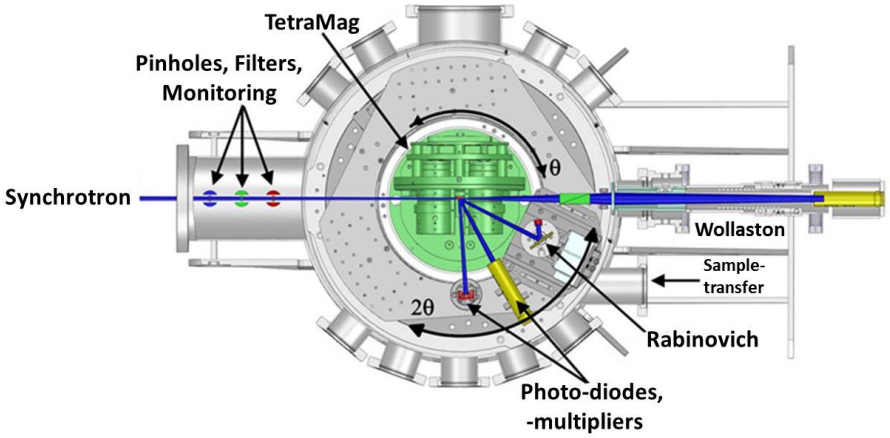

Figure 3.3: Top view of the chamber used for the T-MOKE measurements. The figure is extracted from Reference [67].

3.1.1 Sputter gun

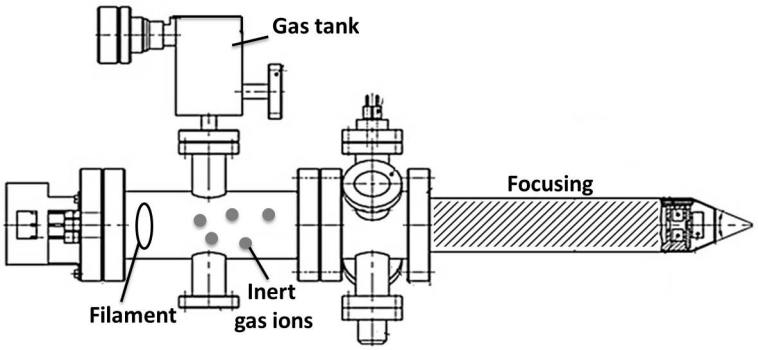

Figure 3.4: Illustration of the sputter gun from SPECS GmbH.

The sputter gun is used for a specifically bombardment of the sample with ions of inert gases. Thereby a material can either be implemented or removed from a solid state surface. In most cases, *sputtering* denotes the removal of atoms from the first layers of a sample. Figure 3.4 illustrate schematically the composition of a sputter gun. In this thesis, the GaAs-sample was sputtered in order to clean and reconstruct the surface.

The inert gas can be let into the gun from an external pressure tank. Electrons

emitting from a filament inside the gun collide with the gas atoms and ionize them. Electrostatic lenses focus these ions and additional deflecting plates rasterize the ion-beam over the sample surface. Thereby, the inert gas ions collide with the surface atoms and if the energy transfer is high enough, the surface atoms remove. Certainly, due to the sputtering the sample surface becomes rough, thus the ion energy should not be too high, and the sputter process should not last too long. In order to remove only atoms from the first layers the sample is located in an angle of 45° with respect to the sputter gun normal. If this angle is too big the inert gas ions can be implemented within the sample and if it is too small the ions do not reach enough atomic layers. In contemplation of smoothing the surface, the sample is heated after a sputter process. This procedure, referred to *anneal*, provides a rearrange of the atoms. Nevertheless, foreign atoms (contaminations) from deeper parts of the sample can diffuse to the surface due to this annealing part. Hence, a preparation procedure mainly consists of several sputter and anneal cycles until the sample is clean or reconstructed.

3.1.2 Electron beam evaporator

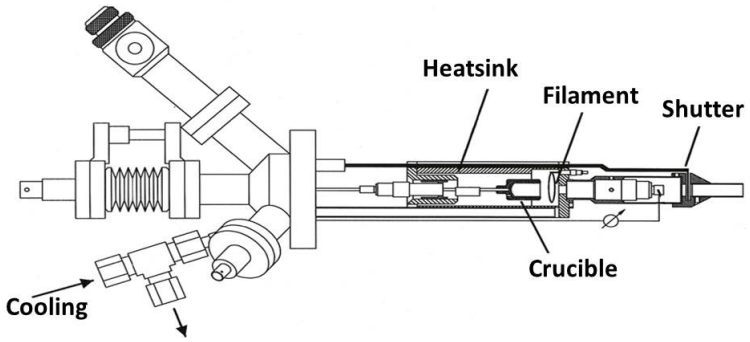

Figure 3.5: Illustration of the electron beam evaporator from OMICRON.

The evaporation of materials is a suitable method to prepare adsorbate layers, especially for multilayer-systems. In this work, an electron beam evaporator is used where the material is evaporated by pointedly electron bombardment. The electron beam evaporator is sketched in Fig. 3.5.
The material is located in a crucible or attached itself. It is encompassed by a circular formed filament of Tungsten (W). By thermionic emission the material is heated up to its boiling point. An additional high voltage directly attached at the material focusses the evaporation beam towards the sample. To blind the voltage,

the filament and the material are in an isolated copper cylinder. This heatsink is water cooled, due to the high temperatures during the evaporation. In order to regulate the evaporation time a shutter is located at the end of the evaporator. The sample stays mostly at room temperature and is rotated around its surface normal to ensure a smooth growth of the adsorbate.

3.1.3 Low energy electron diffraction system

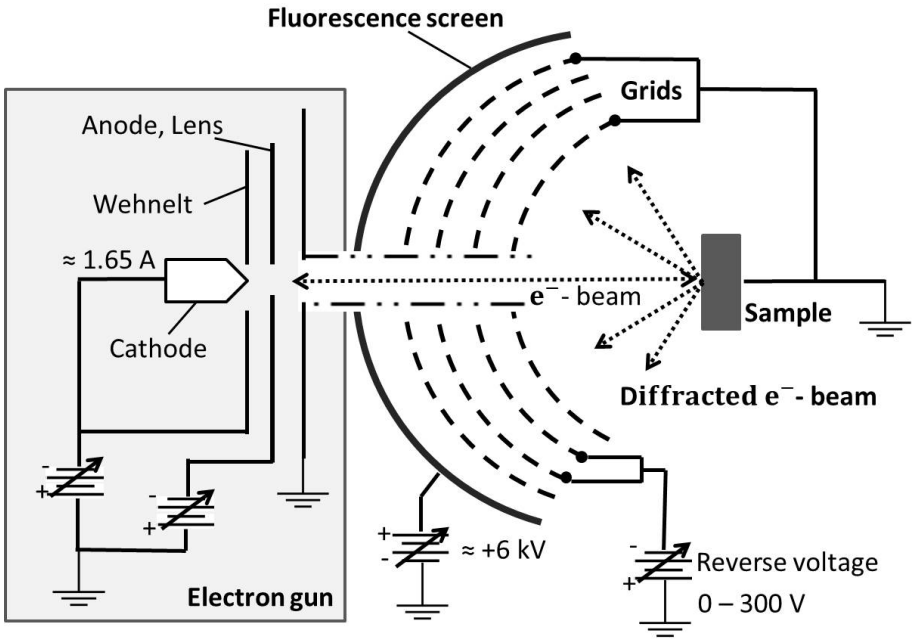

Figure 3.6: Schematic illustration of the LEED-system by SPECS GmbH.

The **L**ow **E**nergy **E**lectron **D**iffraction (LEED) is a valid method to investigate surface structures. It is especially used to examine the sample surface reconstruction after a preparation procedure. The diffraction of electrons at a crystal was first observed by Clinton Davisson and Lester Germer in 1927 [71]. A schematic illustration of the LEED-system is shown in Fig. 3.6.

An electron gun generates electrons with a low but constant energy in the range of $E_{\text{kin}} = 10\,\text{eV} - 500\,\text{eV}$. A system consisting of a wehnelt and three lenses focus the electron beam directly towards the sample. These electrons are scattered at the surface atoms. Afterwards, the diffracted electrons pass through an assembly of four grids and are detected by a fluorescence screen. The locations where the diffracted electrons impinged light up on the screen, hence they are named *reflex*. The third

and second grid have an external potential to filter the inelastic scattered electrons. The remained electrons are accelerated by the high screen voltage of $U_{\text{screen}} = 6\,\text{kV}$ in order to increase the intensity of the reflexes. The first and the fourth grid are grounded just like the sample. This ensures a zero field between sample and the LEED-system, as well as between the diffracted beam and the screen. The reflexes detected at the screen illustrate the surface structure of the sample.
The successfully preparation of a structure coating the full surface area can be verified by a rotation of the sample around its azimuth angle during the LEED measurement. If the reflexes rotate evenly without vanishing, the structure is located area wide at the surface. Furthermore, possible islands of different structures can be identified within one LEED pattern. If the surface is not reconstructed or the structure has no long-range order, the screen shows a dead green luminescence only. Due to the fact that the inelastic mean free paths of electrons with low energies are small, the LEED method is a very suitable tool to investigate the structure of sample surfaces. In comparison to x-ray photoelectron diffraction LEED is not sensitive to chemical bonds and energy states. In this work, LEED was used to verify the successful reconstruction of the GaAs-substrate. A detailed description of the LEED method and the dynamic multiple diffraction theory can be found in Reference [72].

3.1.4 Sample holder

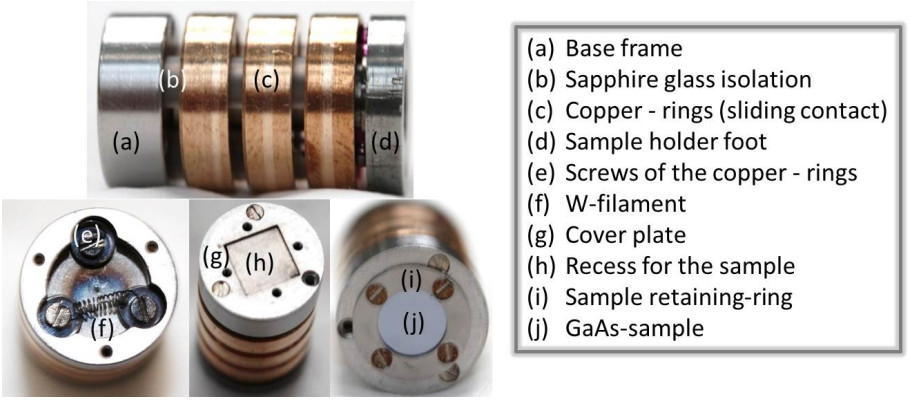

Figure 3.7: Pictures of the sample holder being used for XPS/ XPD measurements. Its specific properties are displayed and denoted in the box.

The sample holder is shown in Fig. 3.7. The base frame consists of premium steel, the foot is molybdenum, and the three rings are made up of copper. These are

insulated to each other and to the base frame by sapphire glass. The filament of Tungsten (W) is kept by the screws of the topmost rings. The sample is located in a recess of the cover plate and is held by a retaining-ring. Therefore, the sample can be heated indirectly by applying a voltage at the filament. The third copper ring acts as an additional ground. The sample holder is fixed directly by a screw into the bottom of the foot on the manipulator of the UHV chamber shown in Fig. 3.1.

3.1.5 Synchrotron source

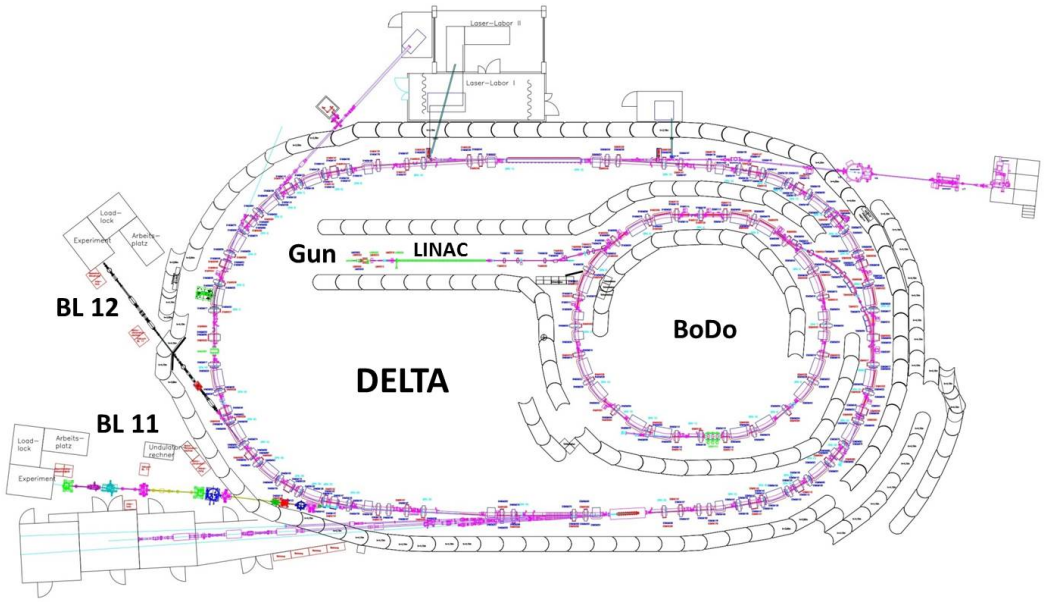

Figure 3.8: Illustration of the electron storage ring DELTA, Dortmund. The electrons emitting from the gun are pre-accelerated in LINAC and BoDo to almost light speed and injected to the DELTA-ring afterwards. By the acceleration of the electrons radially moving through the magnetic fields synchrotron radiation is emitted, which is a special form of the bremsstrahlung. This radiation has a characteristic polarization and the generated frequencies range over the entire electromagnetic spectrum.

The XPS and XPD experiments were performed with soft x-ray radiation of the U-55 PGM beamline 11 at the electron storage ring DELTA (**D**ortmunder **EL**ek**T**ronen-Speicherring **A**nlage) at the Technical University in Dortmund, Germany. Figure 3.8 shows a sketch of the storage ring with its electron gun, linear accelerator (LINAC), and booster system Dortmund (BoDo).
The synchrotron light generates by undulator beamlines deliver high photon flux

with very good energy resolution simultaneously. Beamline 11 is directly located behind the undulator 55 of the storage ring. The electrons incide with almost speed of light into the U-55, which generates the synchrotron light for the beamline. An undulator consists of dipole magnets, which are arranged alternating in north and south pole direction. By passing through the U-55, the electrons are forced on a sinusoidal orbit, due to the changing of the magnetic field. Based on this movement the electrons are relativistic electric dipoles and emit roentgen radiation in their propagation direction. Various mirrors focus the radiation into the beamline. A **P**lane-**G**rating **M**onochromator (PGM) consisting of a plane grating and a plane mirror is used to select one special wavelength from the spectrum delivered by the undulator. The beamline 11 provides photon energies in the range of $E_{\mathrm{ph}} = 50\,\mathrm{eV} - 1500\,\mathrm{eV}$ with a resolution of $\frac{E}{\Delta E} = 10.000$. The focus size is about $70\,\mu\mathrm{m} \times 30\,\mu\mathrm{m}$ and in an energy range of $E_{\mathrm{ph}} = 100\,\mathrm{eV} - 800\,\mathrm{eV}$ the photon flux is maximal with about 10^{13} photons per second.

The T-MOKE investigations are carried out at the TGM beamline 12 at DELTA, in cooperation with Marc Tesch.[1] This beamline was chosen, because its synchrotron light coming from a dipole magnet has a linear and a circular polarized part. It covers the energy range of $E_{\mathrm{ph}} = 20\,\mathrm{eV} - 150\,\mathrm{eV}$ by a **T**oroidal **G**rating **M**onochromator (TGM). The degree of the polarization are $P_{\mathrm{L}} = 0.91$ for linear polarized light and $P_{\mathrm{C}} = \sqrt{1 - P_l^2} = 0.43$ for circular polarized at $E_{\mathrm{ph}} = 60\,\mathrm{eV}$. The spectral resolution was set to $\frac{E}{\Delta E} = 300$. An aluminum-filter within the beamline was used to suppress higher orders [67].

After a while new electrons have to be injected into the DELTA storage ring, due to the finite lifetime of the electrons. During this injection, no XPS, XPD, or T-MOKE measurements could be performed and an offset in the intensity appears, which has to minded within the analysis.

[1] AG Prof. Dr. H.-Ch. Mertins, Physikalische Technik, Fachhochschule Münster

4 Preparation of the system

The investigated three layer system MgO/Fe/GaAs(001) is prepared in situ in the UHV-chamber to ensure the purity of every single layer. The GaAs-samples are cut from an n-conducting Te-doped 3-inches wafer from CrysTec GmbH. The samples are 500 μm thick, 6.5 mm $\times$ 6.5 mm large, and the orientation is better than 5°. Before the sample is transferred into the UHV-chamber it was cleaned in Acetone and Isopropyl in an ultra-sonic bath for 10 minutes each times.
In the following section, the sample-elements are particular introduced and their specific preparation procedure is described.

4.1 Preparation of the GaAs(001) substrate

The III-V-compound semiconductor Gallium-Arsenide (GaAs) consists of the metal Gallium (Ga) and the metalloid Arsenic (As). This odorless grey crystal is used especially in the physical field of semiconductor optics. Due to the higher transit frequency in GaAs than for instance in Silicon, the electrons are able to move faster through the crystal, which directly results in a higher limiting frequency. Indeed, the production of GaAs is elaborate, but during its production the energy gap can be varied and consequently the electronic properties can be affected. This is one of the reasons why GaAs crystals are applied aggrandized in the research field of spintronics.
Gallium-Arsenide crystallizes in a zinc blende structure in which both Gallium and Arsenic are found in face-centered-cubic elementary cell. These single fcc lattices are merged one into another, so that they seem to be shifted against each other a quarter of a cubic diagonal of the elementary cell. Therefore, the (001)-crystal-plane can be either Ga- or As-terminated possessing two dangling bonds. Consequently, a clean (001)-surface is not ideally terminated but rather exhibits a number of different reconstructions [73], which will be discussed in detail in section 4.1.2.
The structure of GaAs is illustrated in Fig. 4.1. The lattice constant of the GaAs crystal is amount to $a_{\mathrm{GaAs}} = 5.654\,\text{Å}$. As a result of the small sublimation point of Arsenic, it will be completely removed from the sample at temperatures greater than $T_{\mathrm{As}} > 650\,^{\circ}\mathrm{C}$, which is known as *Arsenic-flux*.

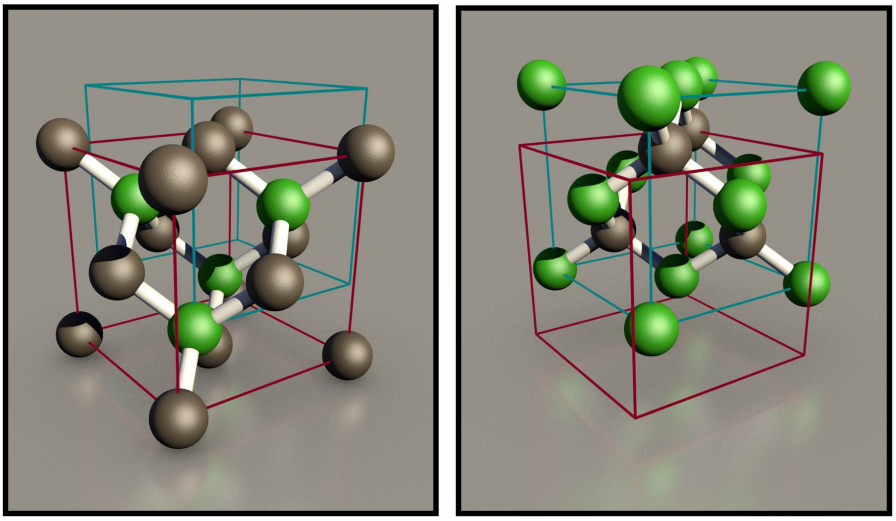

(a) Gallium fcc lattice (b) Arsenic fcc lattice

Figure 4.1: Elementary cell of a GaAs(001) crystal. The single fcc lattices of Gallium (a) and Arsenic (b) are illustrated in red and blue, respectively.
(Ga: brown, As: green)

The temperatures of the preparation process explained in the following are measured contactless by a pyrometer from LumaSense Technologies GmbH.

4.1.1 Preparation of a clean GaAs(001)-surface

In order to prepare a clean GaAs-surface the contamination from air mainly Oxygen (O) and Carbon (C) have to be removed. Due to the small sublimation point of Arsenic, Oxygen cannot be removed by a heating procedure only, because temperatures of $T \geq 850\,^{\circ}\mathrm{C}$ are needed. At these temperatures, Arsenic will be removed completely from the GaAs-crystal. Therefore, a procedure consisting of sputter and annealing parts are applied.
The GaAs-surface was sputtered with Ar-ions with the energy of $E_{\mathrm{Ar}^+} = 1000\,\mathrm{eV}$. The angle between the surface normal and the sputter gun was set to 45° in order to prevent implementation of the Ar-ions. After the sputter time of $t = 30\,\mathrm{min}$ the sample was annealed at $T = 300\,^{\circ}\mathrm{C}$. This low temperature was chosen, because a small Arsenic-flux at around $T > 350\,^{\circ}\mathrm{C}$ was detected during the preparation procedure illustrated by an abruptly increase and decrease of the vacuum pressure. The procedure was repeated twice until the XPS survey scan shows the GaAs core level signals only. This survey scan is shown in Fig. 4.2.

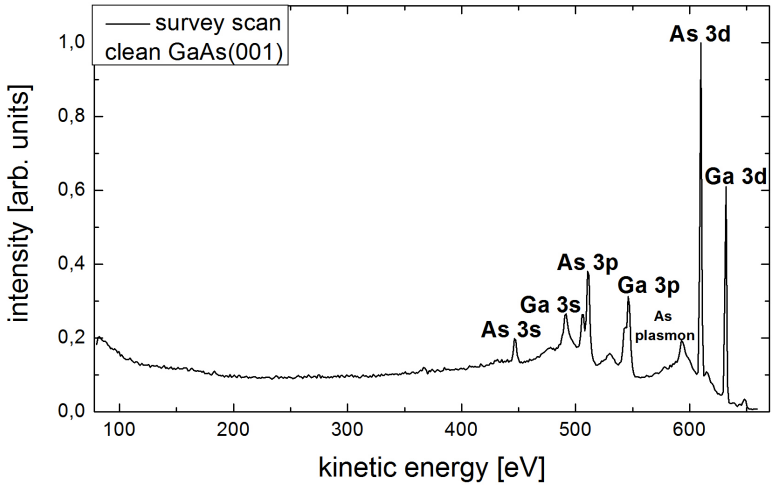

Figure 4.2: Survey scan of the clean GaAs(001)-surface after the preparation procedure detected with $E_{\mathrm{ph}} = 650\,\mathrm{eV}$ at $\theta = 0°$.

As can be clearly seen there are no signals at $E_{\mathrm{kin}} \approx 120\,\mathrm{eV}$ or $E_{\mathrm{kin}} \approx 360\,\mathrm{eV}$ corresponding to Oxygen and Carbon, respectively. Furthermore, a small signal conform to the As-plasmon-peak apparently occur, which is an indication of a clean surface. The subsequently recorded LEED pattern of the GaAs(001) surface does not show any reflexes certifying that the surface is not reconstructed.

4.1.2 Preparation of the GaAs (4×2)-reconstruction

Gallium-Arsenide forms sp^3-hybrid orbitals, which result in a high free energy of the system. The GaAs(001) surface shows a lot of different surface reconstructions to reduce the number of these dangling bonds. A surface reconstruction refers to the process where the atoms of a crystal-surface assume a different structure than the bulk. Basically, the mechanism of dimerization is responsible for the III-V-compound semiconductors (001)-surface reconstructions [73].
Some of the known reconstructions of GaAs(001) are listed below assorted in a descending order of its Arsenic-concentration [74].

$$c(4\times4)$$
$$(2\times4)\,;\,c(2\times8)$$
$$(1\times6)\,;\,(2\times6)\,;\,(3\times6)\,;\,(6\times6)$$
$$(4\times2)\,;\,c(8\times2)$$
$$(4\times6)$$

Decrease of As-concentration

In this so-called *Woods notation* [75] the reconstruction is indicated in relation to the lattice of the bulk. The (2×4) for example means that the plane-vectors of the reconstruction are 2 times and 4 times enlarged. A centered or primitive elementary cell could be indicated by a small c or p, respectively. Certainly, the indication of a primitive cell is dropped in most cases.
The property of the Arsenic-flux is utilized to reconstruct Ga-rich surface structures by means of heating and sputtering cycles. In this work, one of the most Ga-rich reconstruction, the (4×2), is chosen, because it is established as a very suitable substrate for epitaxial growth of Iron layers [59, 76, 77]. As-rich reconstruction are noted in literature to promote inter-diffusion [78, 79].
The preparation procedure of the (4×2) was found during my diploma thesis and explained in detail therein [80]. The five preparation steps are summarized in Tab. 4.1.

step	**parameter**	
degas	flush	$T_{\text{sample}} = 600\,^{\circ}\text{C}$, 1 min
	constant temperature	$T_{\text{sample}} = 540\,^{\circ}\text{C}$, ≈ 60 min
sputter	Argon-ions	$E_{\text{Ar}^+} = 1000$ eV, 20 min
anneal	heating ratio $r = \pm 20\,^{\circ}\text{C/min}$	$T_{\text{sample}} = 550\,^{\circ}\text{C}$, 45 min
sputter	Argon-ions	$E_{\text{Ar}^+} = 500$ eV, 10 min
anneal	heating ratio $r = \pm 20\,^{\circ}\text{C/min}$	$T_{\text{sample}} = 550\,^{\circ}\text{C}$, 45 min

Table 4.1: The five preparation steps of GaAs(4×2)-reconstruction.

In the first step the sample is heated up to $T = 600\,^{\circ}\text{C}$ observing the vacuum pressure. The degas temperature is held until the pressure in the UHV chamber

drops under $p < 1 \times 10^{-9}$ mbar again and afterwards the sample is cooled down to room temperature. During each sputter step the sample is rotated around its surface normal to support an evenly sputtering of the surface.
The LEED patterns measured after this procedure are illustrated in Fig. 4.3 for various azimuth angle positions φ_L.

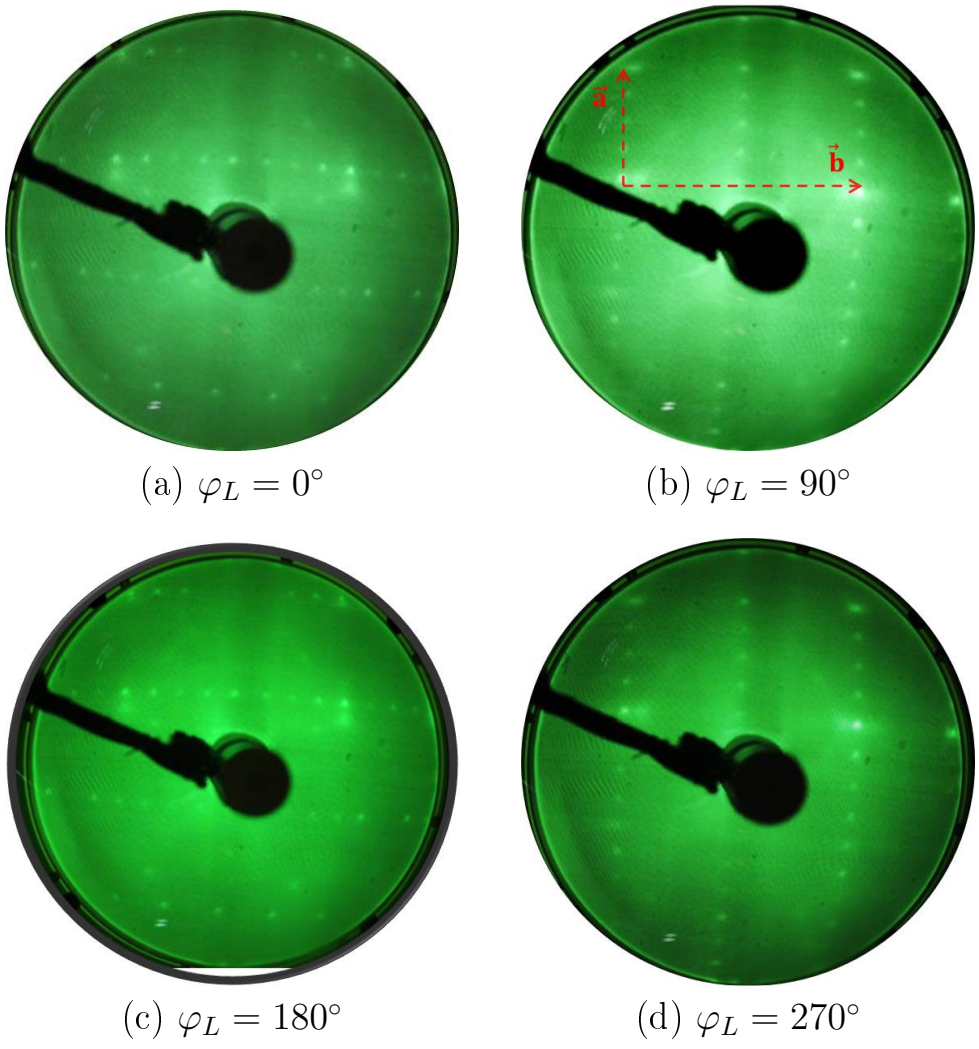

(a) $\varphi_L = 0°$ (b) $\varphi_L = 90°$

(c) $\varphi_L = 180°$ (d) $\varphi_L = 270°$

Figure 4.3: LEED patterns of the GaAs (4×2)-reconstruction at different azimuth angles φ_L and $E_{\text{kin}} = 111\,\text{eV}$. The red arrows illustrate the unit cell of the surface reconstruction.

The reflexes caused by the surface reconstruction are clearly visible as small bright dots and will be explained briefly. Considering the LEED pattern at $\varphi_L = 90°$, every fourth reflex in the direction of $\vec{a}$ is brighter as the others, because an atom of the reconstruction is located directly on top of a substrate atom. The reflexes

between them only originate from atoms of the reconstruction structure. Starting from this bright reflex in $\vec{b}$-direction every second reflex is brighter due to the same reason. In other words, these LEED patterns illustrate the (4×2)-reconstruction. All reflexes rotate evenly, if the sample is rotated around its azimuth angle confirming a successful preparation and a well ordered surface. LEED pattern confirming the (4×2) or (2×4) are indistinguishable, because LEED is not chemical sensitive. In this thesis, the high temperature during the preparation procedure resulting the visible strong As-fluxes exclude the As-rich (2×4)-reconstruction.

4.2 Preparation of the Fe-film

The silvery-white transition metal Iron (Fe) is one component of the Earth's crust, although it occurs mostly in chemical bonds. Such bonds can be found for example in catalysts and electrical engineering. The magnetization of a material due to collective electron-interaction, the *ferromagnetism*, receive its name from the famous ferromagnet Iron. Furthermore, Iron exhibits a high electron binding energy, which explains its preference in ferromagnet devices such as TMR-junctions or in spintronics-systems.
Iron crystallizes in a body-centered-cubic lattice with a constant of $a_{\mathrm{Fe}} = 2.866\,\text{Å}$ at room-temperature. The elementary cell of this bcc structure is illustrated in Fig. 4.4.

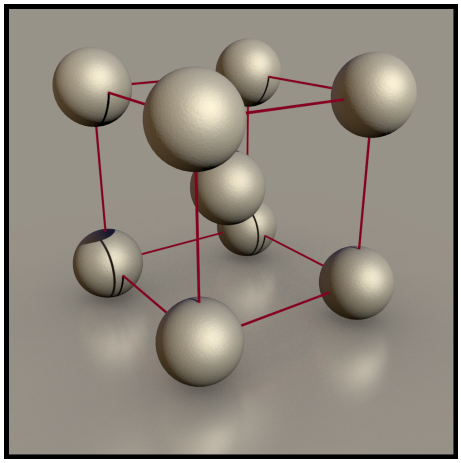

Figure 4.4: Elementary cell of a bcc structured Fe(001) crystal.

With increasing temperatures Iron forms different types of lattice-structures, which is known as the *polymorphism* of Iron. In contrast to the semiconductor GaAs,

the clean Fe(001) surface knows no reconstructions but forms a well ordered (1x1)-surface.
In this work, the Fe-film was prepared by a directly evaporation of an Iron wire with a purity of 99.99%. The reconstructed GaAs-substrate was kept at room temperature and rotated around its azimuth angle to ensure a smooth growth. The parameters of the electron-beam evaporator are listed in Tab. 4.2.

parameter	**value**
current of W-filament	$I_{\mathrm{Fil}} = 1.99\,\mathrm{A}$
high voltage	$U_{\mathrm{HV}} = 700\,\mathrm{V}$
current of emission	$I_{\mathrm{EM}} = 18\,\mathrm{mA}$
chamber pressure	$p < 5 \times 10^{-10}\,\mathrm{mbar}$
time	$t = 15\,\mathrm{min}$
thickness	$d_{\mathrm{Fe}} \approx 18\,\mathrm{Å}$

Table 4.2: Evaporation parameters for the preparation of the Fe-film.

Iron is known to grow crystalline at least 70 monolayers on a GaAs-substrate [81]. The relation between the lattice constants of GaAs and bcc structured Iron is $a_{\text{bcc-Fe}} \approx \frac{1}{2} a_{\mathrm{GaAs}}$. Hence, the base-centered cubic structure is preferred during the epitaxial growth of Fe on GaAs [76, 80, 82].

The Fe-layer thickness was calculated using the high resolution XPS spectra of the Fe 3p signal discussed in chapter 5.1.1. The equation for the layer thickness d_{XPS} is given by

$$d_{\mathrm{XPS}} = \lambda_{\mathrm{Fe}} \cdot \sin(\theta) \cdot \ln\left(\frac{N_b \lambda_b I_0}{N_0 \lambda_0 I_b} + 1\right) \ , \tag{4.1}$$

with the polar angle θ and the IMFP λ_{Fe} of electrons in Iron. The parameters N_b, I_b and N_0, I_0 represent the concentration and intensities with and without an adsorbate layer, respectively. The element specific inelastic mean free paths are given by λ_b and λ_0 [39]. In this study, the thickness of the Iron-film was calculated to be $d_{\mathrm{Fe}} \approx 18\,\mathrm{Å}$, which correlates to a layer-growth of $g_{\mathrm{Fe}} \approx 0.3\,\mathrm{monolayer/min}$.

4.3 Preparation of the MgO-film

Magnesium oxide (MgO) is the salt of the alkaline earth metal Magnesium. It forms a white powder or sheer crystals. In the medical and food industry MgO is a very important element due to its property to dissolve acids and converts them into salts. The factor of the band gap of MgO amounts to $\Delta = 7.8\,\mathrm{eV}$, thus MgO is technically used as an insulator. Since the year 2000, MgO is well established as the barrier between two ferromagnetic layers in TMR devices. This is mainly because MgO provides electronic states, which cause high spin polarizations of the electrons. Therefore, electrons originating from shells with high polarization tunnel through, whereas electrons with a specific symmetry of the orbitals can be completely suppressed [16]. This phenomenon leads to a high TMR-effect.
Magnesium oxide crystallizes in a halite structure with a lattice constant of $a_{\mathrm{MgO}} = 4.213\,\text{Å}$. Within this structure the Magnesium (Mg) and Oxygen (O) atoms are surrounded octahedral by each other, which is illustrated in Fig. 4.5.

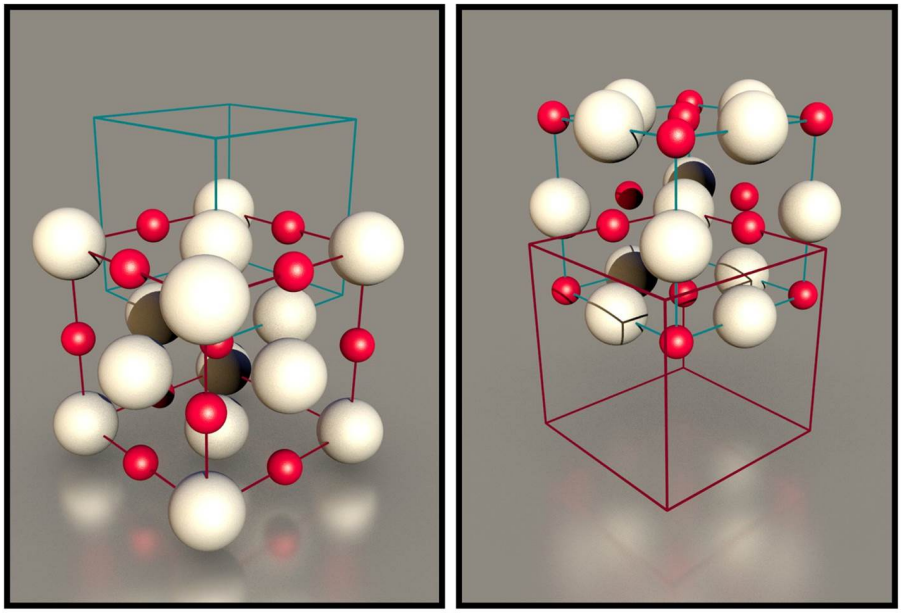

(a) Magnesium fcc lattice (b) Oxygen fcc lattice

Figure 4.5: Elementary cell of MgO(001) crystal. The single fcc lattices of Magnesium (a) and Oxygen (b) are illustrated. (Mg: white, O: magenta)

The clean MgO(001)-surface is likewise to the Fe(001) (1x1)-structured and has no more complex reconstructions like Gallium-Arsenide. In this work, the MgO-film was prepared by a directly evaporation of a MgO-crystal with a purity of 99.95%.

The parameters are summarized in Tab. 4.3.

parameter	**value**
current of W-filament	$I_{\mathrm{Fil}} = 2.6\,\mathrm{A}$
high voltage	$U_{\mathrm{HV}} = 1200\,\mathrm{V}$
current of emission	$I_{\mathrm{EM}} = 18\,\mathrm{mA}$
chamber pressure	$p < 5 \times 10^{-10}\,\mathrm{mbar}$
time	$t = 15\,\mathrm{min}$
mean thickness	$d_{\mathrm{MgO}} \approx 4.6\,\mathrm{Å}$

Table 4.3: Evaporation parameters for the preparation of the MgO-film.

The layer thickness in the case of the MgO-film was calculated by using the XPD data discussed in chapter 5.2.2. Thereby the equation for the layer thickness

$$d_{\mathrm{XPD}} = -\ln\left(1 - \frac{I}{I_0}\right) \cdot \lambda_{\mathrm{MgO}} \cos(\theta) \tag{4.2}$$

is used. The polar angle θ, the intensities corresponding to the surface state I and the most low-lying state I_0, and the IMFP λ_{MgO} of electrons in MgO are used [41]. In the case of the MgO/Fe-system the most low-lying component is the Iron bulk signal, so the calculation devotes a mean layer thickness for the MgO film of $d_{MgO} \approx 4.6\,\mathrm{Å}$. Thus the growth condition was $g_{\mathrm{MgO}} \approx 0.08\,\mathrm{monolayer/min}$.

5 Results and discussion

In order to determine the structure and chemical composition of the interfaces of the MgO/Fe/GaAs system, the initial conditions of each layer have to be known. The GaAs(4×2)-substrate was selected, because it is known to facilitate the epitaxial growth of iron layers [59, 76, 77]. During this thesis a deposition of Iron on a clean but unreconstructed GaAs-sample was additionally performed in order to verify this assumption. A crystalline Fe-film is indispensable to ensure an epitaxial growth of a thin MgO-layer.
First, the interface of the Fe/GaAs(4×2) system will be discussed in chapter 5.1 regarding to the XPS and XPD analysis. The following section 5.2 will be focused on the XPS and XPD investigation of the MgO/Fe-interface. The magnetic properties verified by T-MOKE measurements of MgO/Fe/GaAs(4×2) are discussed in chapter 5.3. A verification whether the reconstruction of the GaAs(001) substrate is essentially needed to achieve a crystalline Fe-film will be given in section 5.4.

5.1 Fe/GaAs(4×2)-interface

Survey spectra allow to identify all elements located in the sample. Furthermore, it is a sufficient tool to verify quickly, if an adsorbate is located on the sample after an evaporation procedure. The survey scans before and after the deposition of the Iron-film are shown in Fig. 5.1. The core-levels of the GaAs-substrate and the Fe-film, as well as the As plasmon-peak and the Fermi-edge are denoted. The Fe-signals became clearly visible after the preparation procedure, which indicates that Fe grows on the GaAs-substrate. No contaminations of the sample are appeared induced by elements like Carbon or Oxygen.

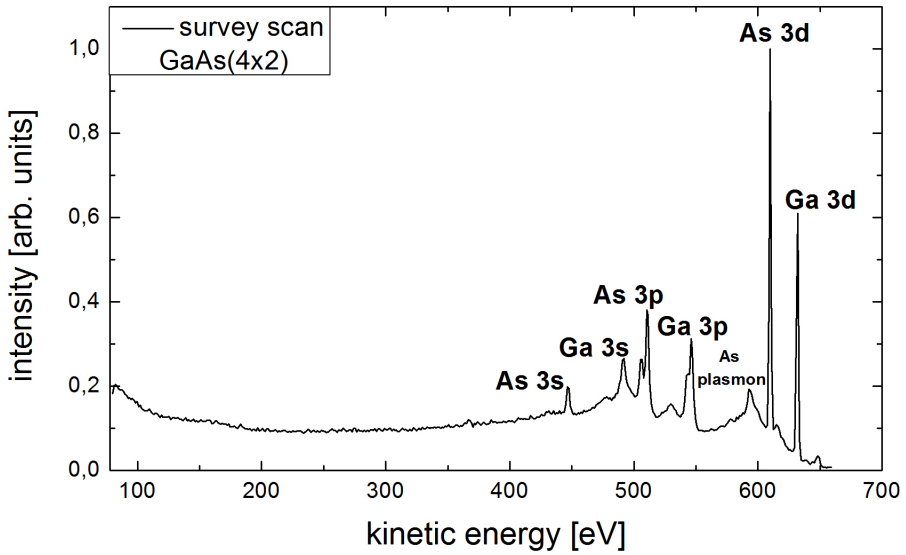

(a) GaAs(4×2)-substrate

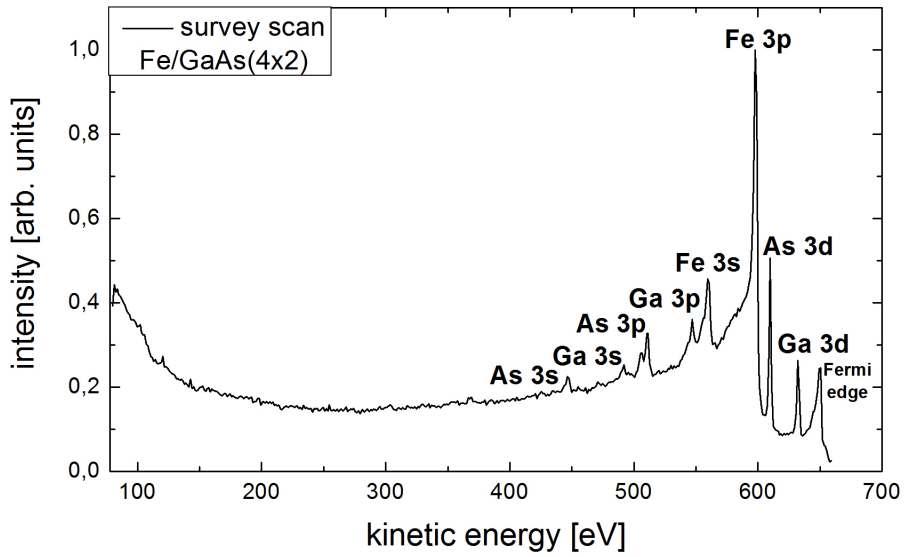

(b) Fe/GaAs(4×2)

Figure 5.1: Survey scan before (a) and after (b) the deposition of Fe on GaAs(4×2)-substrate. Both spectra are detected at the photon energy of $h\nu = 650\,\mathrm{eV}$ and normal emission $\theta = 0°$. The signals of the elements located within the sample are denoted.

5.1.1 XPS analysis

After the preparation procedure of the GaAs(4 × 2)-reconstruction high-resolution spectra of As 3*d* and Ga 3*d* core level signals were detected. With a view to further measurements a photon energy of $h\nu = 320\,\text{eV}$ was chosen, although it is not the most suitable energy for investigations of the GaAs-surface. However, this high energy is needed to investigate the GaAs-substrate beneath the Fe-film and equal measuring conditions have to be applied in order to identify possible changes. The high-resolution spectra were detected for two polar angles of $\theta = 0°$ and the more surface sensitive angle of $\theta = 60°$ in order to determine components in the subsurface and surface regions.

The *d*-orbital split into $d_{5/2}$ and $d_{3/2}$ doublets with a height ratio of $h_{\text{LS}}(d) = 3/4$. The value of the spin-orbit coupling in the case of Arsenic 3*d* is $f_{\text{LS}}(As3d) = 0.69\,\text{eV}$ [83]. The kinetic energies used for the identification of the chemical bonds are denoted relating to the As $3d_{5/2}$-level.
The best least squares fits using the Gaussian function in Eq. (2.9) of the As 3*d* XPS-signal without the additional Fe-layers are shown in Figure 5.2 (a) and (b). The best agreement was achieved by two components, a large component B_{As} and a smaller component $A1$. The strong component is located at the kinetic energy of $E_{\text{kin}}(B_{\text{As}}) = 274.18\,\text{eV}$ and corresponds to the bulk signal of As 3*d* in GaAs(4 × 2). The small component is found at $E_{\text{kin}}(A1) = 274.57\,\text{eV}$ resulting in a shift of about $\Delta E_{\text{A1}} = 0.25\,\text{eV}$ to higher kinetic energies with regard to the bulk signal. The component $A1$ increase compared to B_{As}, if the polar angle is increased to the more surface sensitive position of $\theta = 60°$. Hence, the small component can be related to a surface-state of the Arsenic in GaAs(4 × 2).
The high-resolution spectra of As 3*d* are detected after the Fe-deposition again. A comparison of the line shapes of the signals are shown in Figure 5.2 (c) and (d). A detailed analysis by a fitting procedure resulted in three components for the As 3*d*-signal. These high-resolution spectra are illustrated in Figure 5.2 (e) and (f) for the two polar angles of $\theta = 0°$ and $\theta = 60°$, respectively. They reveal a greater change within the signal as firstly expected. The component at $E_{\text{kin}}(B_{\text{As}}) = 274.18\,\text{eV}$ conforms to the bulk signal B_{As}. The additional component $A2$ located at $E_{\text{kin}}(A2) = 274.38\,\text{eV}$ is shifted about $\Delta E_{\text{A2}} = 0.20\,\text{eV}$ to higher kinetic energies with respect to the As bulk signal. This component becomes strongly dominant within the As 3*d*-signal for increasing polar angles. This directly illustrates that

it is located in the interface region and can be related to a Fe-As-bond originating from the Fe-deposition. Due to the Fe-covered GaAs-surface the As surface state $A1$ disbanded. The third component $A3$ at $E_{\mathrm{kin}}(A3) = 273.00\,\mathrm{eV}$ is shifted about $\Delta E_{\mathrm{A3}} = 1.18\,\mathrm{eV}$ to lower kinetic energies. This small component was essential to reach a good accordance between the experimental data and the Gauß-Fit in the low energy range. It decrease strongly for increasing polar angle and is hardly visible in the spectra recorded at $\theta = 60°$. Probably, it corresponds to As-atoms of the bulk, which rearrange due to new bonds between Fe and the GaAs-substrate. This can be elucidated by a structure analysis discussed in section 5.1.2.
All parameters of the least squares fit performed for the As 3*d*-signal before and after the Fe-deposition are summarized in Tab. 5.1.

system	**component**	**kinetic energy [eV]**	**FWHM [eV]**	**SOC [eV]**
(4×2)	As bulk	274.18	0.27	0.69
	A1	274.43	0.57	0.69
Fe/(4×2)	As bulk	274.18	0.29	0.69
	A2	274.38	0.55	0.69
	A3	273.00	0.50	0.69

Table 5.1: Parameters of the best least squares fit for As 3*d*-signal of the GaAs(4×2) before and after Fe-deposition. The photon energy was amount to $h\nu = 320\,\mathrm{eV}$.

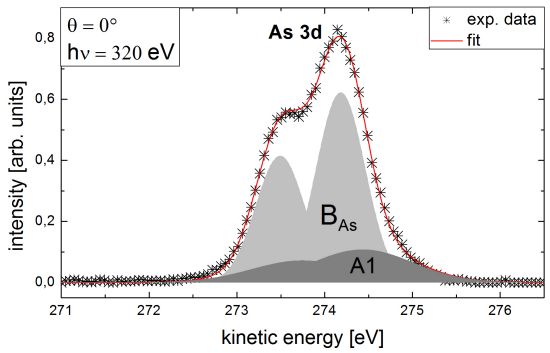

(a) (4×2)-reconstructed

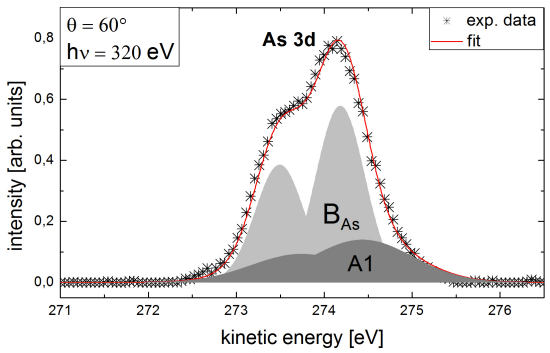

(b) (4×2)-reconstructed

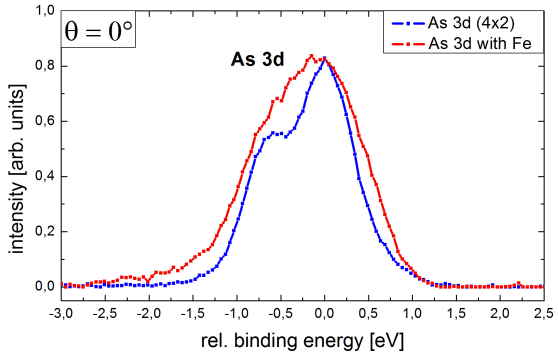

(c) comparison

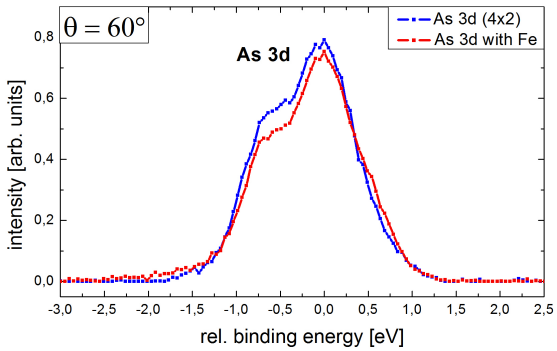

(d) comparison

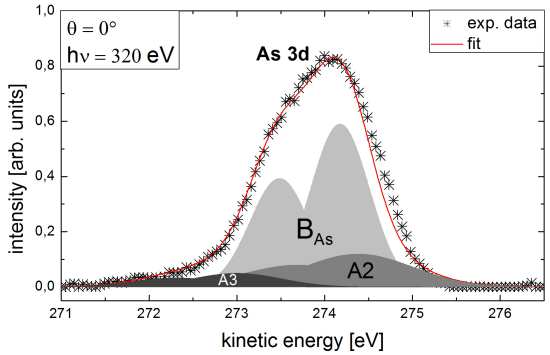

(e) Fe/GaAs(4×2)

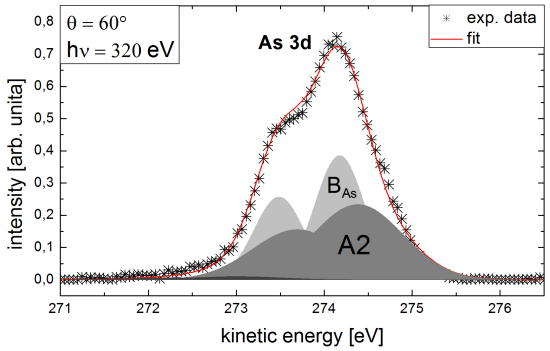

(f) Fe/GaAs(4×2)

Figure 5.2: High-resolution XPS spectra of As $3d$ core-level before (a), (b), in comparison (c), (d), and after Fe-deposition (e), (f). All spectra are detected at $E_{\mathrm{ph}} = 320\,\mathrm{eV}$ and compared for the two polar angles of normal emission $\theta = 0°$ and surface sensitive emission $\theta = 60°$ illustrated in left and right column, respectively.

According to the As $3d$-signal the Ga $3d$ core level split into the $d_{5/2}$ and $d_{3/2}$ multiplets. The height ratio amounts to $h_{\mathrm{LS}}(d) = 3/4$ likewise, because it only depends on the orbital. In the case of Gallium the energy shift caused by the spin-orbit coupling is $f_{\mathrm{LS}}(Ga3d) = 0.45$ [83]. The kinetic energies are related to the Ga $3d_{5/2}$-level.
The best least squares fits of Ga $3d$ without additional Fe-layers are shown in Figure 5.3 (a) and (b) for the both polar angles of $\theta = 0°$ and $\theta = 60°$, respectively. The best agreement during the fitting procedure was achieved with three components. The strong component located at $E_{\mathrm{kin}}(B_{\mathrm{Ga}}) = 295.97\,\mathrm{eV}$ corresponds to the Ga bulk-signal B_{Ga} of Gallium-Arsenide (4×2)-reconstruction. The two additional components $G1$ and $G2$ are found at $E_{\mathrm{kin}}(G1) = 295.45\,\mathrm{eV}$ and $E_{\mathrm{kin}}(G2) = 296.44\,\mathrm{eV}$, respectively. With regard to the Ga bulk signal, the component $G1$ is shifted about $\Delta E_{\mathrm{G1}} = 0.52\,\mathrm{eV}$ to higher kinetic energy, whereas $G2$ is shifted about $\Delta E_{\mathrm{G2}} = 0.47\,\mathrm{eV}$ to lower kinetic energies. A comparison between the two polar angles of normal emission $\theta = 0°$ and surface sensitive emission $\theta = 60°$ displays an increase of both components for increasing polar angles. This directly illustrates that they are located on the surface of the sample. Therefore, these additional components can be related to Ga-Ga bonds of the Ga-rich (4×2)-reconstruction [74]. Since the increase of $G1$ is larger than for $G2$ it can be assumed that the $G1$ atoms originate from the topmost layers of the surface. The atoms of $G2$ are located in the surface region, but subjacent to the $G1$ atoms. As been mentioned in section 4.1 in most cases dimerization is the mechanism for GaAs surface reconstructions. Therefore, the two components $G1$ and $G2$ could be describe Ga-dimers, which will be elucidated by the following structure analysis in section 5.1.2.
The measure of the Ga $3d$ high-resolution spectra is directly repeated after the Fe-deposition. A comparison between the Ga-signals are shown in Figure 5.3 (c) and (d) and display a fully change of the line shapes. Especially the Ga $3d$-signal recorded at the surface sensitive emission of $\theta = 60°$ seems to be shifted with respect to the former signal of the GaAs(4×2)-substrate. A detailed analysis performed by the Gaussian least squares fits resulted in three components of the Ga $3d$ anew. They are shown in Figure 5.3 (e) and (f) for $\theta = 0°$ and $\theta = 60°$, respectively. The component at $E_{\mathrm{kin}}(B_{\mathrm{Ga}}) = 296.00\,\mathrm{eV}$ conforms to the Ga bulk signal. The very small divergence of E_{kin} can be explained by numerical and measuring inaccuracy during the fitting and measure procedure. The additional components $G3$ and $G4$ are located at $E_{\mathrm{kin}}(G3) = 295.21\,\mathrm{eV}$ and $E_{\mathrm{kin}}(G4) = 296.88\,\mathrm{eV}$. They are shifted with respect to the bulk signal B_{Ga} about $\Delta E_{\mathrm{G3}} = 0.79\,\mathrm{eV}$ and $\Delta E_{\mathrm{G4}} = 0.88\,\mathrm{eV}$ to lower and higher kinetic energies, respectively. As can be clearly seen by a compar-

ison of Figure 5.3 (b) and (f), the Ga 3*d* peak is not shifted, but the component *G*3 dominate the complete signal. It increases greatly for increasing polar angles with respect to the two other components. Meanwhile, the component *G*4 decrease with respect to *G*3, but keep almost constant with regard to the bulk-signal. This illustrate, that both components originate from Ga-atoms located in the interface. Furthermore, the atoms originating from *G*4 are located subjacent to the atoms of the component *G*3. They can be explained by a disbandment of the Ga-Ga bonds *G*1 and *G*2 of the (4×2)-surface becoming Fe-Ga-bonds. Alternatively, the component *G*4 can be originate from Fe-GaAs-bonds minding the results of the As 3*d* analysis and the lightly decrease of *G*4 for increasing polar angles with respect to B_{Ga}.
The parameters of the Ga 3*d* best least squares fit of the GaAs(4×2)-substrate and the Fe/GaAs(4×2)-system are summarized in Tab. 5.2.

system	**component**	**kinetic energy [eV]**	**FWHM [eV]**	**SOC [eV]**
(4×2)	Ga bulk	295.97	0.25	0.45
	G1	295.45	0.40	0.45
	G2	296.44	0.38	0.45
Fe/(4×2)	Ga bulk	296.00	0.26	0.45
	G3	295.21	0.50	0.45
	G4	296.88	0.31	0.45

Table 5.2: Parameters of the best least squares fit for Ga 3*d*-signal of GaAs(4×2) before and after Fe-deposition using the photon energy of $h\nu = 320\,\mathrm{eV}$.

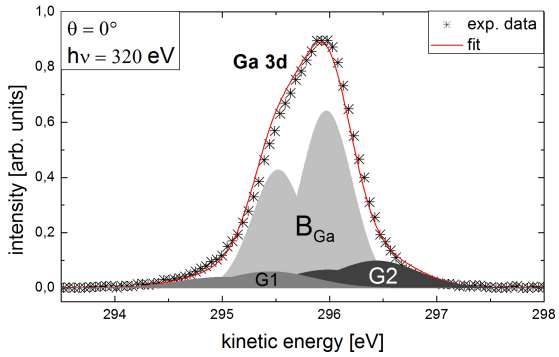

(a) (4×2)-reconstructed

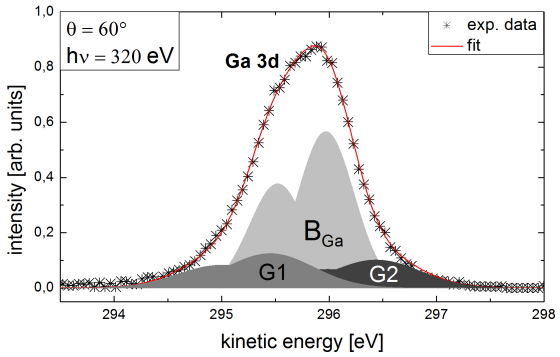

(b) (4×2)-reconstructed

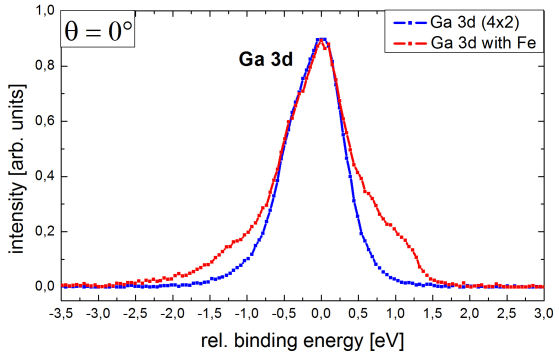

(c) comparison

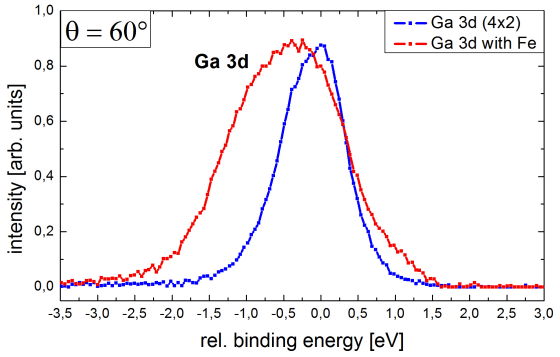

(d) comparison

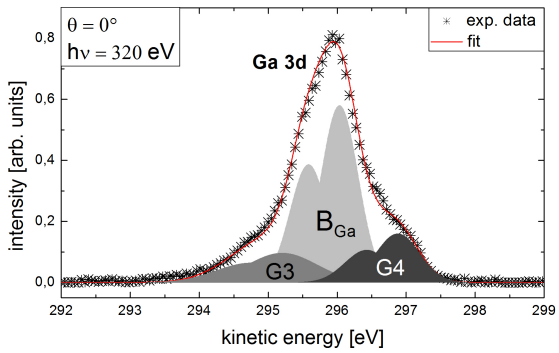

(e) Fe/GaAs(4×2)

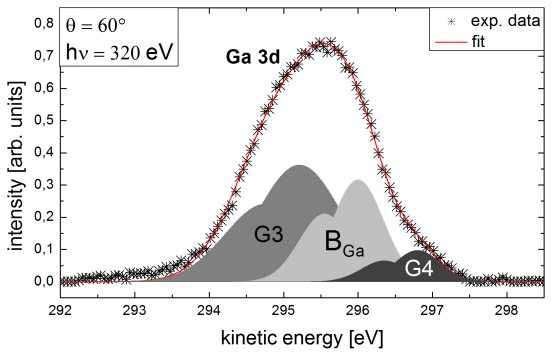

(f) Fe/GaAs(4×2)

Figure 5.3: High-resolution XPS spectra of Ga $3d$ core-level before (a), (b), in comparison (c), (d), and after Fe-deposition (e), (f). The spectra are recorded at two polar angles of $\theta = 0°$ (left column), $\theta = 60°$ (right column), and photon energy of $h\nu = 320\,\mathrm{eV}$.

In order to investigate the only $d_{\mathrm{Fe}} \approx 18\,\text{Å}$-thick Fe-film (see Sec. 4.2) a low photon energy of $E_{\mathrm{ph}} = 180\,\mathrm{eV}$ was chosen, because it ensures surface sensitivity with an excellent cross section of the Fe $3p$ core level [40] at the same time. The p-level split up into a $p_{3/2}$ and a $p_{1/2}$ doublet, separated by $f_{\mathrm{LS}}(Fe3p) = 0.80\,\mathrm{eV}$ due to the spin-orbit coupling in the case of the Fe $3p$-signal [84]. The height ratio for a p-level is $h_{\mathrm{LS}}(p) = 1/2$ and the energy position are denoted in relation to the Fe $3p_{3/2}$-level. As discussed in Sec. 2.1.2, the Gaussian influence of the measure equipment dominates the XPS high-resolution spectra and even suppresses lightly the asymmetry of a metal peak. The small difference between the Gauß-Fit and an asymmetric-fit in the case of the here investigated Fe $3p$-signal will be discussed in Appendix A.1. The high-resolution spectra of the deposited Fe-film are shown in Figure 5.4 (a) for $\theta = 0°$ and (b) for $\theta = 60°$.

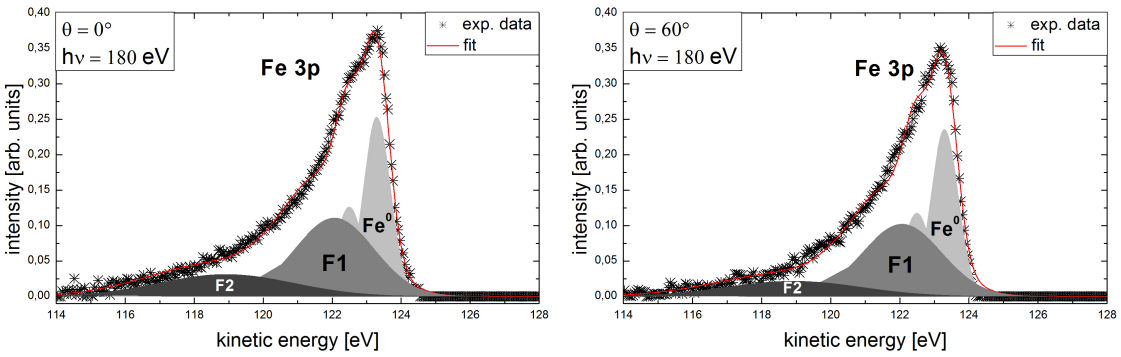

(a) (b)

Figure 5.4: High-resolution XPS spectra of Fe $3p$ core-level at $\theta = 0°$ (a) and $\theta = 60°$ (b) detected at $E_{\mathrm{ph}} = 180\,\mathrm{eV}$.

The best agreement between experimental data and the least squares fit was achieved for three components within the Fe $3p$-signal. The strong component Fe^0 located at $E_{\mathrm{kin}}(Fe^0) = 123.29\,\mathrm{eV}$ corresponds to the energy state of pure Iron. The components $F1$ and $F2$ are found at the kinetic energies of $E_{\mathrm{kin}}(F1) = 122.07\,\mathrm{eV}$ and $E_{\mathrm{kin}}(F2) = 118.92\,\mathrm{eV}$. With respect to the Fe^0-signal they are shifted about $\Delta E_{\mathrm{F1}} = 1.29\,\mathrm{eV}$ and $\Delta E_{\mathrm{F2}} = 4.47\,\mathrm{eV}$ to lower kinetic energies. Due to their energy positions the components $F1$ and $F2$ are identified as the Fe^{2+} and Fe^{3+} ionized-states of the Iron, respectively. In most cases these states occur from an oxidation, but the values of the energy shifts detected in this work are not in line with literature [85–87]. Furthermore, the survey scan directly detected after the Fe-deposition on GaAs

shown in Figure 5.1 (b) reveal no Oxygen O 1*s*-signal, which have to occur if the Fe-film is oxidized. By comparing the spectra for the two polar angles of $\theta = 0°$ and $\theta = 60°$ a decrease of both additional components with respect to the bulk signal is observed. This clearly illustrates that these components are located in the interface between the GaAs-substrate and the Fe-adsorbate. Therefore, they cannot be explained by an oxidation, but by bonds to the GaAs-substrate. Iron is in its second and third oxidation state in a Fe-As and Fe-Ga compound, respectively [88, 89]. The component $F2$ related to the Fe-Ga bond decrease stronger than the component $F1$, which can be explained by the Fe-As bond being located superior to the Fe-Ga-bonds. This fact could be a hint of an out-diffusion of the Arsenic into the Fe-film. The Fe-GaAs bonding states $F1$ and $F2$ are perfectly in line with the additional components $A2$, $G3$, and $G4$ of the As 3*d* and Ga 3*d* spectra after the Fe-deposition.
In the interest to get further information of the Fe/GaAs-interface high-resolution spectra of Fe 3*p* are detected with a higher photon energy of $E_{\mathrm{ph}} = 320\,\mathrm{eV}$. They are shown in Fig. 5.5.

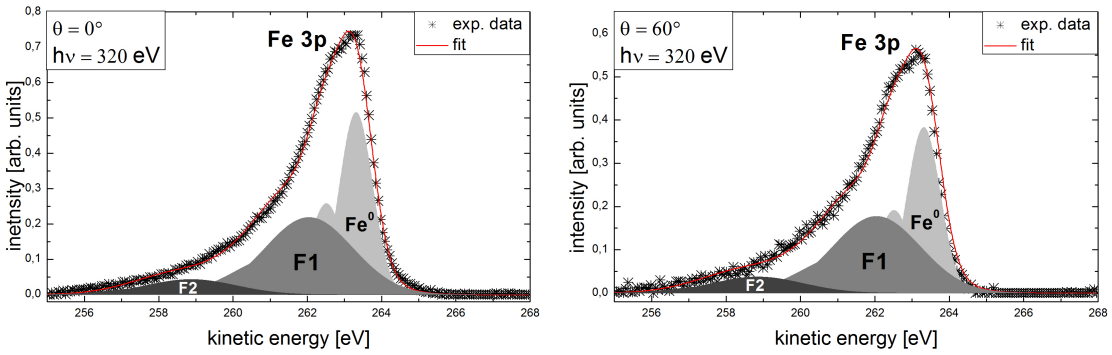

(a) (b)

Figure 5.5: High-resolution XPS spectra of Fe 3*p* core-level at $\theta = 0°$ (a) and $\theta = 60°$ (b) detected at $E_{\mathrm{ph}} = 320\,\mathrm{eV}$.

The best agreement was achieved with three components at the kinetic energies of $E_{\mathrm{kin}}(Fe^0) = 263.31\,\mathrm{eV}$, $E_{\mathrm{kin}}(F1) = 262.04\,\mathrm{eV}$, and $E_{\mathrm{kin}}(F2) = 258.86\,\mathrm{eV}$. The strong component correspond to the Fe^0-state of pure Iron. The additional components $F1$ and $F2$ are shifted about $\Delta E_{\mathrm{F1}} = 1.27\,\mathrm{eV}$ and $\Delta E_{\mathrm{F1}} = 4.45\,\mathrm{eV}$ and decrease for increasing polar angle. They are perfectly in line with the Fe-Ga and Fe-As components discussed for the lower energy spectra of Fig. 5.4. The differences

within the energy positions can be explained by measure and numerical uncertainty. The spectra using higher energy do not offer further information, nevertheless they confirm the former results.
The parameters of the least squares fit for the Fe $3p$ spectra with the two excitation energies are summarized in Tab. 5.3. Thereby, $\Delta E' = E_{\mathrm{ph}} - E_{\mathrm{kin}}$ defines the differences between exciting energy E_{ph} and kinetic energy E_{kin} in order to aid comparison.

E_{ph}	component	E_{kin} [eV]	$\Delta E'$ [eV]	FWHM [eV]	SOC [eV]
180 eV	Fe^0	123.29	56.71	0.36	0.80
	F1	122.07	57.93	1.15	0.80
	F2	118.92	61.08	1.95	0.80
320 eV	Fe^0	263.31	56.69	0.42	0.80
	F1	262.04	57.96	1.17	0.80
	F2	258.86	61.14	1.20	0.80

Table 5.3: Parameters of the best least squares fit for the Fe-film using the Gaussian fit-function. The two photon energies were set to $E_{\mathrm{ph}} = 180\,\mathrm{eV}$ and $E_{\mathrm{ph}} = 320\,\mathrm{eV}$.

The analysis of the core level XPS spectra of As $3d$, Ga $3d$, and Fe $3p$ resulted in Fe-As and Fe-Ga bonds located in the interface between the substrate and the deposited Fe-film. An inter-diffusion of the GaAs-substrate and a Fe-adsorbate is part of several works [78, 79, 90, 91]. The Fe-GaAs components $A3$ of the As $3d$-signal, $G4$ of Ga $3d$-signal, and the greater increase of the Fe-As component $F1$ of Fe $3p$-signal allow the assumption that Gallium and Arsenic atoms diffuse into the Fe-film. The interface may consist of several layers of Fe-As, Fe-Ga, or Fe-Ga-As. The Arsenic seems to interact stronger with the Iron, so that the As-diffusion is stronger. Nevertheless, the presence of a possible amorphous interface structure due to out-diffusion can be examined by the performed XPD measurements discussed in the following section.

5.1.2 XPD analysis

The atomic structure model of the GaAs(001) (4×2)-reconstruction was verified during my diploma thesis [80] as the Ga-rich *two-dimers model*. Therein, low energy XPD patterns with an exciting photon energy of $h\nu = 90\,\text{eV}$ was used, because it is the most suitable energy for investigations of the GaAs-surface. As mentioned in section 4.1 the single layers of the (001)-plane of a GaAs-crystal consists either of Gallium or Arsenic atoms only. In the (4×2)-reconstruction the Gallium dimers are located in the first and third layer of this system. Thereby, every forth As-row is missing in the [001]-direction. The pure zinc blende structure of the GaAs-crystal is found from the fourth layer below. This two-dimers model first proposed by Biegelsen *et al.* [92] is illustrated in Figure 5.6.

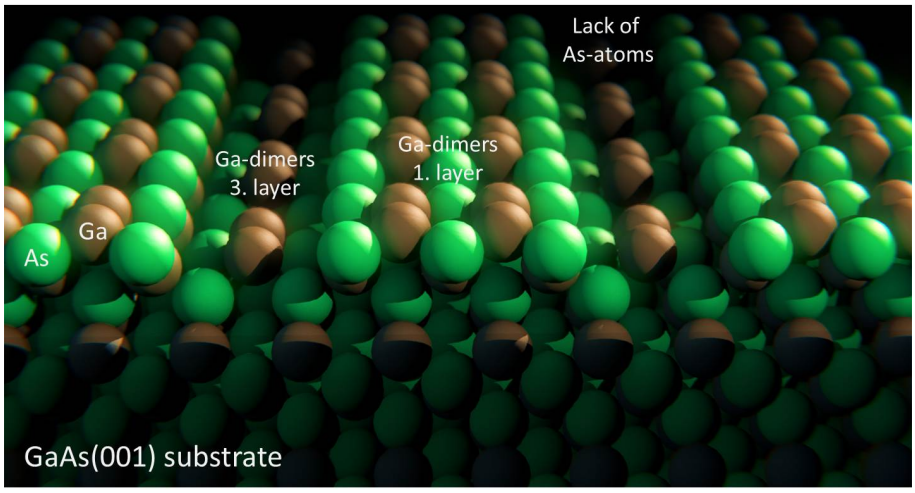

Figure 5.6: Atomic structure model of (4×2)-reconstruction of GaAs(001). In this two-dimers model the Ga-dimers are found in first and third layer of the system, resulting in a lack of As at the surface. The zinc blende structure is found from the fourth layer below. (As: green, Ga: brown)

The Ga-dimers of the (4×2)-reconstruction are located in the first and third layer. They explain the Ga-Ga-bonding states $G1$ and $G2$ of the Ga $3d$ core level spectra in Figure 5.3 (a) and (b). Furthermore, the surface-state component $A1$ of the As $3d$ can also be explained by the structure of the (4×2) yielding a rearrange of the As at the surface. The local symmetry of the Arsenic changes due to the gap of As-atoms. In a zinc blende structure both Gallium and Arsenic are in a twofold-symmetry environment. The structure of the (4×2) surface reconstruction with the lack of As-atoms causes a change of the environmental symmetry. The As-atoms at the surface are now found in a locally fourfold symmetry environment [59].

The XPD patterns recorded for the As 3*d*- and Ga 3*d*-signal with the photon energy of $E_{\mathrm{ph}} = 320\,\mathrm{eV}$ are shown in Figure 5.7.

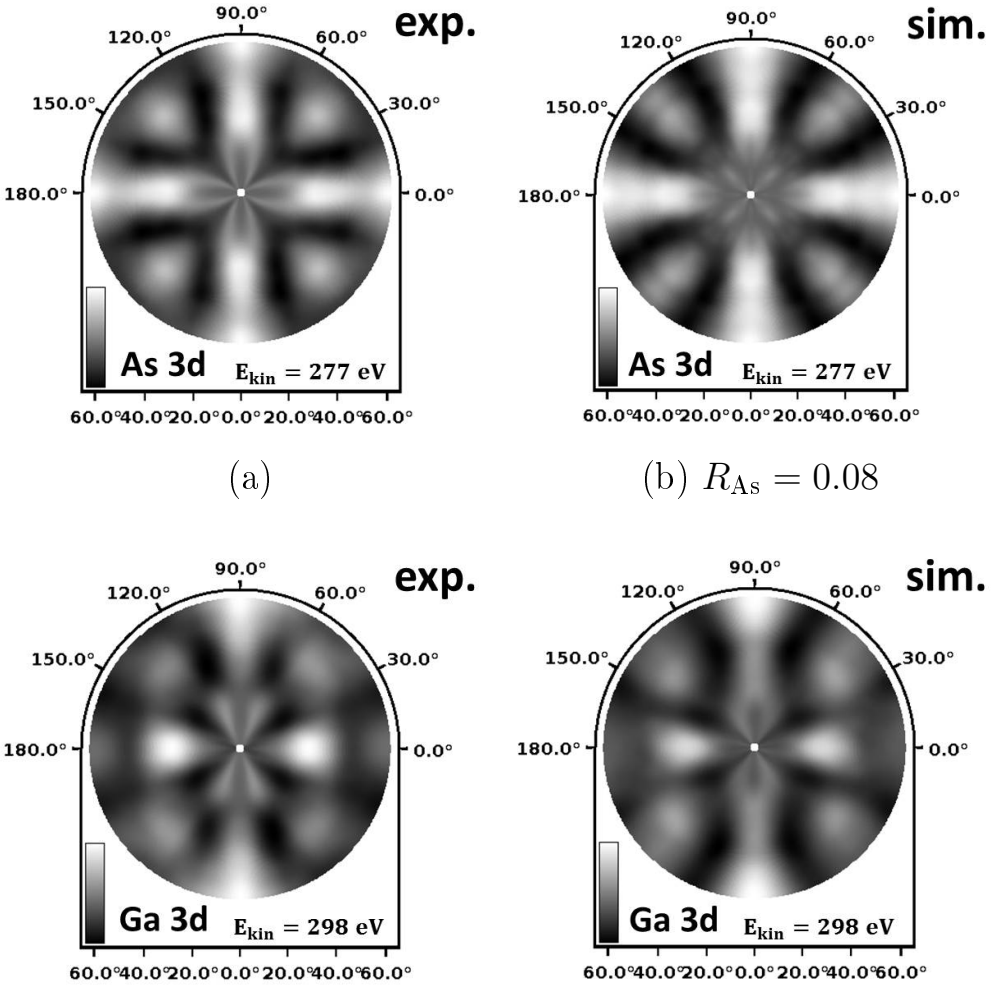

(a) (b) $R_{\mathrm{As}} = 0.08$

(c) (d) $R_{\mathrm{Ga}} = 0.10$

Figure 5.7: Experimental and best simulated XPD pattern of As 3*d* (a), (b) and Ga 3*d* (c), (d) for GaAs(4 × 2)-reconstruction based on the two-dimers model. A photon energy of $E_{\mathrm{ph}} = 320\,\mathrm{eV}$ was used as the excitation energy.

The Ga 3*d*-pattern show a twofold rotational symmetry, whereas the As 3*d* show a fourfold symmetry. In the view of the resulting high kinetic energies of $E_{\mathrm{kin}}(As) = 277\,\mathrm{eV}$ and $E_{\mathrm{kin}}(Ga) = 298\,\mathrm{eV}$, both patterns are expected to show the twofold symmetry caused by the zinc blende structure. Indeed, the surface structure influences the diffraction pattern strongly, because all emitting photoelectrons have to pass the

surface, which explains the still fourfold symmetry of the As 3*d* pattern. A simulation using the MSPHD-program based on the two-dimers model shown in Figure 5.6 resulted in excellent R-factors of $R_{\mathrm{As}} = 0.08$ and $R_{\mathrm{Ga}} = 0.10$. Further simulations with varied structures deteriorated the accordance between experimental and simulated patterns strongly. The best simulated As 3*d* and Ga 3*d* patterns are shown in Figure 5.7 (b) and (d). The cluster consists of about 122 atoms within the simulations. They display the crystalline and well ordered (4×2)-reconstruction of the GaAs(001)-surface. Furthermore, the high energy patterns confirm the previous results using low energies of $E_{\mathrm{kin}}(As) = 47\,\mathrm{eV}$ and $E_{\mathrm{kin}}(Ga) = 69\,\mathrm{eV}$ for As 3*d* and Ga 3*d*, respectively [80].

Again, As 3*d* and Ga 3*d* XPD patterns are directly detected after Fe-deposition, in order to identify structural differences of the GaAs(4×2)-substrate. The analysis of the XPS high-resolution spectra of the Fe/GaAs-system discussed in chapter 5.1.1 yielded in several Fe-As-Ga layers in the interface. Therefore, the XPD patterns are expected to illustrate a structural change of the GaAs. The As 3*d* and Ga 3*d* patterns beneath the Fe-adsorbate are illustrated in Figure 5.8 (b) and (d) in comparison to the patterns of the pure (4×2)-surface. For time reasons during the measurement the GaAs patterns after the Fe-deposition are measured downto $\theta = 6°$ instead of $\theta = 0°$, however the main structure information are provided by the higher polar angles.

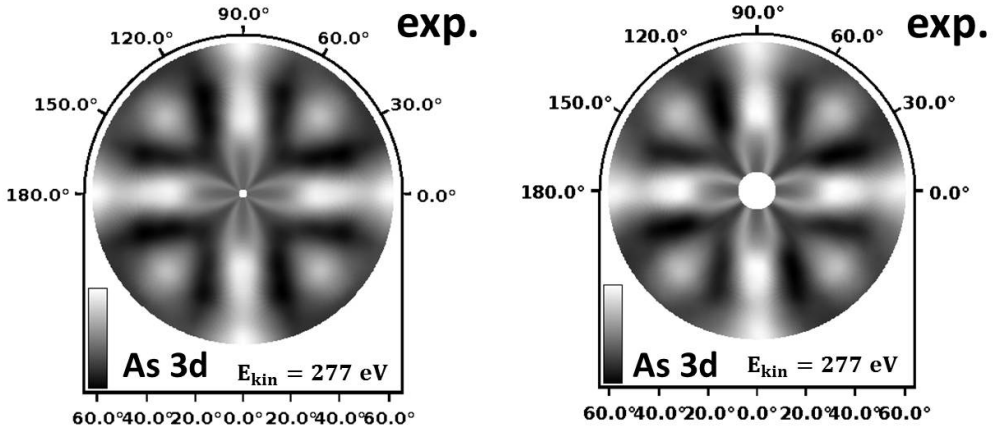

(a) (4×2) (b) with Fe-layers

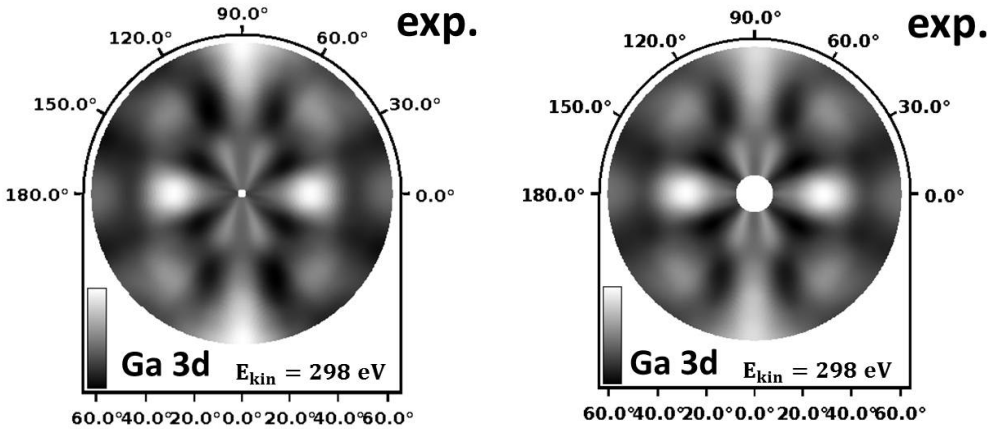

(c) (4×2) (d) with Fe-layers

Figure 5.8: Comparison of experimental XPD patterns of the (4×2)-reconstruction, As $3d$ (a), (b), and Ga $3d$ (c), (d) before and after the deposition of the Fe-film.

Surprisingly, no differences can be recognized at a first sight. The patterns before and after the Fe-deposition were compared using the R-factor to display a possible divergence. Hence, only a very weak difference can be observed demonstrated by the very low R-factors of $R_{\text{diff}}(As) = 0.02$ and $R_{\text{diff}}(Ga) = 0.03$ for Arsenic and Gallium, respectively. The XPD analysis clearly demonstrate, that the base frame structure of the GaAs (4×2)-substrate is not lifted. Although Fe-Ga and Fe-As bonds are located in the interface, they do not form a crystalline structure.
Furthermore, the analysis of the high resolution XPS spectra of As $3d$ and Ga $3d$ reveal a possible out-diffusion into the Iron film. The structure investigation by XPD pattern does not show any great structural changes. An amorphous structure

cause destructive interference of the out-going photoelectrons. Therefore, crystalline layers are not visible within XPD pattern, if the amorphous layers are numerous. The inter-diffusion of the GaAs-substrate was proposed especially for As-rich reconstructions [78, 79]. In this study diffusion cannot be excluded strictly, but due to the thin Fe-film and the results from the XPD investigation, it is rather improbable. Especially the fact that the local emitter environment of Arsenic is still fourfold disapproves an inter-diffusion. Therefore, the weak difference within the XPD pattern of As 3*d* and Ga 3*d* can be explained by a rather weak signal-to-noise ratio of the GaAs-signals due to the deposition of the Fe-film. The Fe-As and Fe-Ga bonds located in the interface may only illustrate the Ga-dimers and topmost As-atoms banded to the Fe-film.

In order to get further information about the deposited Fe-film and the interface structure XPD patterns of the Fe 3*p*-signal are detected using the photon energies of $E_{\mathrm{ph}} = 180\,\mathrm{eV}$ and $E_{\mathrm{ph}} = 320\,\mathrm{eV}$, respectively. This results in a low energy pattern of $E_{\mathrm{kin}}(Fe_I) = 125\,\mathrm{eV}$ and a high energy pattern of $E_{\mathrm{kin}}(Fe_{II}) = 265\,\mathrm{eV}$. They are shown in Fig. 5.9 (a) and (c). Both patterns show a fourfold rotational symmetry. The lower energy pattern Fe_I was first analyzed during my diploma thesis and resulted in a bcc structured Fe-film yielding an R-Factor of $R = 0.12$ [80]. Therefore a bcc structure with the lattice constant of $a_{\mathrm{Fe}} = 2.8\,\mathrm{Å}$ was used as a starting model for the simulations.

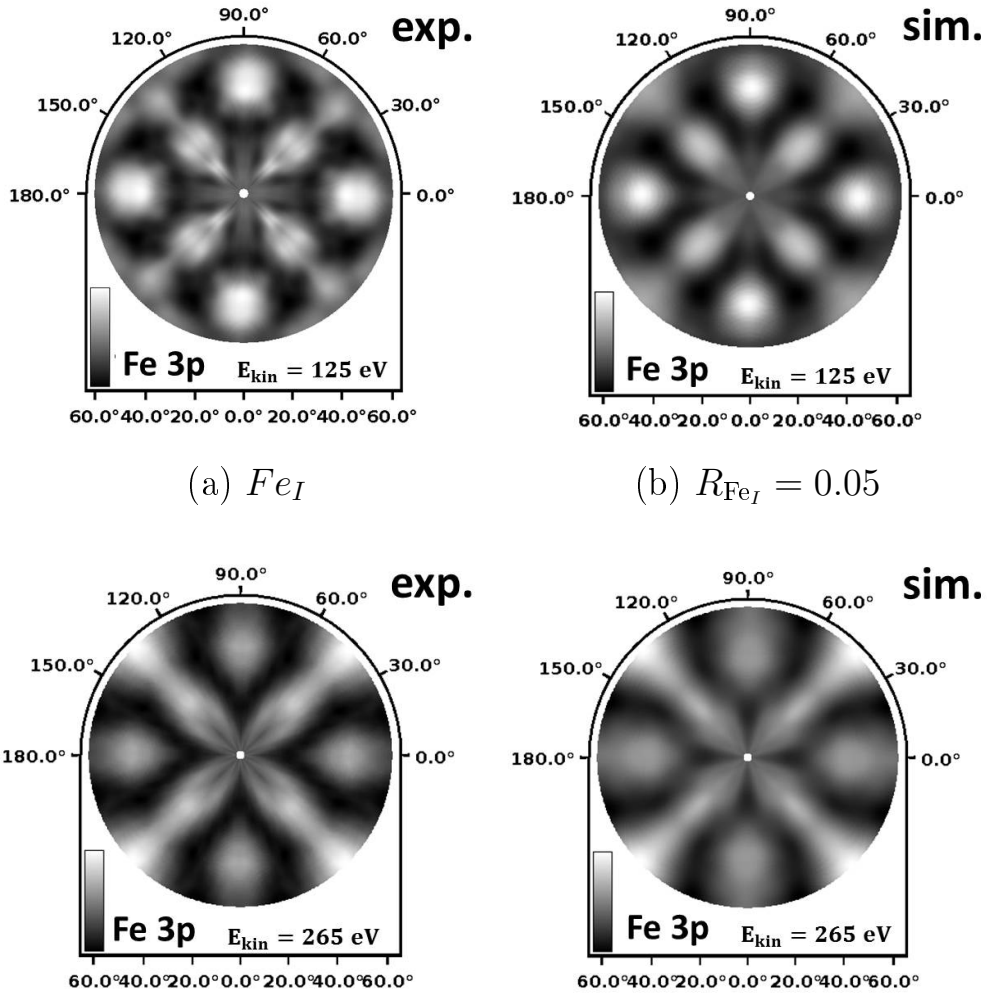

(a) Fe_I (b) $R_{\mathrm{Fe}_I} = 0.05$

(c) Fe_{II} (d) $R_{\mathrm{Fe}_{II}} = 0.07$

Figure 5.9: Experimental and best simulated Fe 3p patterns for the low energy $E_{\mathrm{kin}}(Fe_I) = 125\,\mathrm{eV}$ (a), (b), and the high energy $E_{\mathrm{kin}}(Fe_{II}) = 265\,\mathrm{eV}$ (c), (d), respectively.

During the simulations the cluster size varied between 50 and 100 atoms. The accordance between the simulation and the experimental data was not good, because of R-factors greater than $R \gg 0.1$. Especially the simulations for the higher energy pattern of $E_{\mathrm{kin}}(Fe_{II}) = 265\,\mathrm{eV}$ resulted in bad agreement due to four missing reflexes illustrated in Figure 5.10 (a). Because of the polymorphism of Iron it crystallizes in a face-centered cubic structure with $a_{\mathrm{Fe}}(fcc) = 3.6\,\text{Å}$ at high temperatures of $T \geq 910\,^{\circ}\mathrm{C}$. Kalki *et al.* observe a phase transition between bcc and fcc during the deposition of a Fe-film on a Copper-sample [93]. Therefore, various structure models consisting of several layers of bcc and fcc structured Iron, as well as pure fcc

structures were simulated. However, none of them resulted in R-factors better than $R > 0.5$. These simulated patterns are shown in Fig. 5.10 exemplarily.
Considering these simulations a bcc structure was kept as the model for the Fe-film.

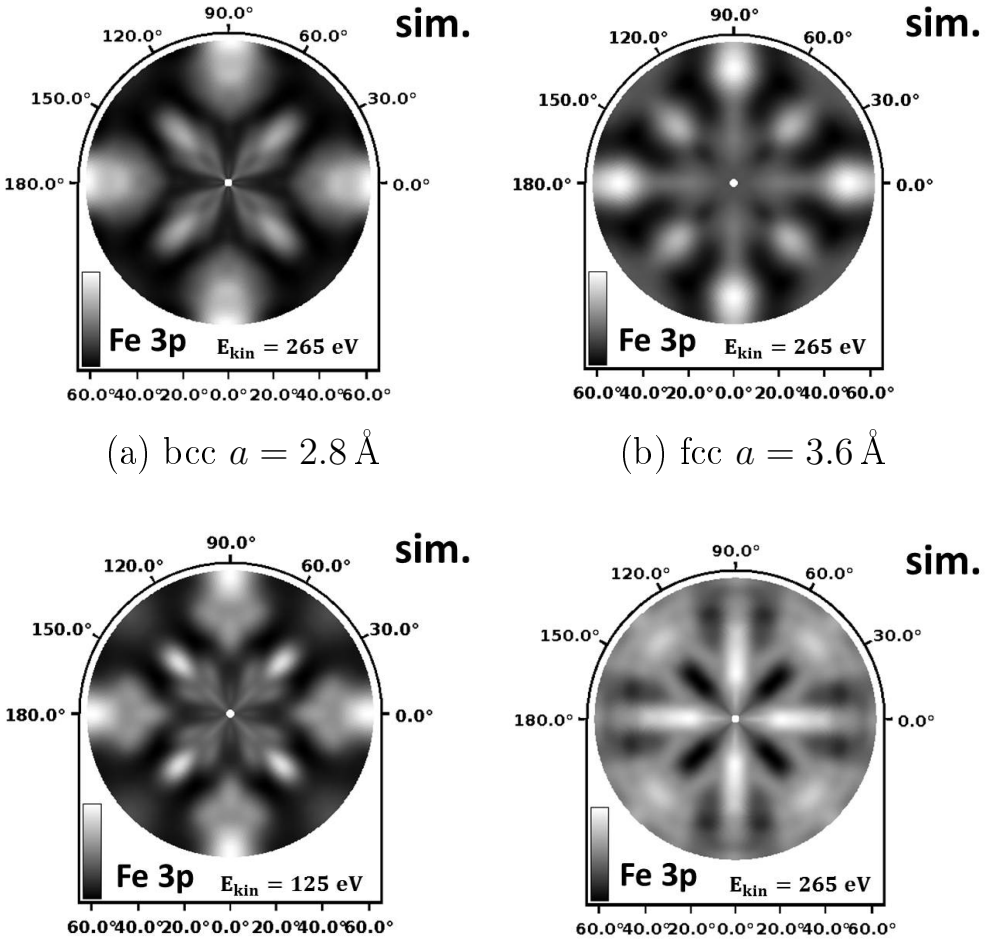

(a) bcc $a = 2.8\,\text{Å}$ (b) fcc $a = 3.6\,\text{Å}$

(c) bcc/fcc mixture (d) bcc/fcc mixture

Figure 5.10: Simulated XPD patterns for various manner of structure models for the Fe-film of the Fe/GaAs(4×2)-system.

Due to the higher exciting energy of $E_{\text{ph}} = 320\,\text{eV}$ the GaAs-substrate may influence the Fe $3p$ patterns. Therefore a structure model consisting of the GaAs(4×2) surface and a bcc structured Fe-film on top are simulated. An R-factor analysis resulted in bad agreement for the low energy pattern Fe_I and even for the high energy pattern Fe_{II} displayed by $R \approx 1.2$. In order to improve the accordance to the experimental data the genetic algorithm mentioned in Sec. 2.2.2 was applied. In

the case of the high energy pattern Fe_{II}, the R-factor was minimized by a strained bcc-lattice with the constant of $a_{\mathrm{Int}} = 3.2\,\text{Å}$. Certainly, this is in contradiction with the simulations for the low energy pattern Fe_I, which results in the known lattice constant of $a_{\mathrm{Fe}} = 2.8\,\text{Å}$. Accordingly, a modified model was build where the Fe-film is bcc structured, the lattice constant was set to $a_{\mathrm{Fe,int}} = 3.2\,\text{Å}$ in the interface, and $a_{\mathrm{Fe}} = 2.8\,\text{Å}$ at the surface layers. In between several amounts of lattice constants in the range of $a_{\mathrm{Fe,int}} > a_{\mathrm{sim}} > a_{\mathrm{Fe}}$ were simulated. The best agreement was achieved where the lattice constant decrease evenly to $a_{\mathrm{Fe}} = 2.8\,\text{Å}$ with every additional Fe-layer. This *pyramid-like* structure resulted in an excellent agreement between the simulations and the experimental data with $R_{\mathrm{Fe}_I} = 0.05$ and $R_{\mathrm{Fe}_{II}} = 0.07$ for the low and high energy pattern, respectively. This phenomenon is named *tetragonal distorsion* of crystalline films [94]. Here, it is along the [110]-direction and represented by the strained lattice of the Fe-interlayer. The tetragonal distorsion can be explained by the known simultaneous layer and island growth of the Iron on a GaAs-substrate [76,81,95]. The islands become greater and grow together the more iron is deposited. In this thesis, the thin Fe-film allows the observation of this growing condition within the XPD pattern. The best simulated patterns are shown in Fig. 5.9 (b) and (d). The development of the R-factors during the simulations are summarized in Fig. 5.11.

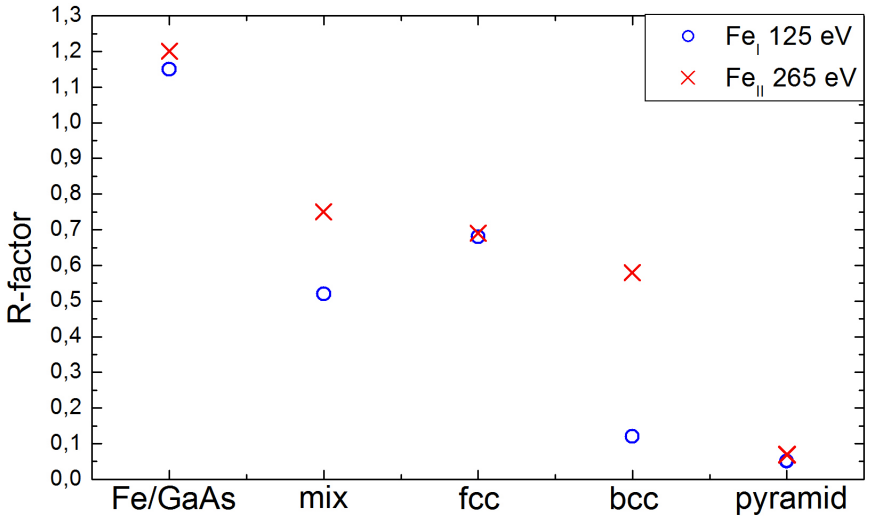

Figure 5.11: Illustration of the R-factors of the five basic Fe structure models described in the text. The best agreement for both Fe 3p patterns Fe_I and Fe_{II} are achieved for the pyramid-like bcc structure.

As can be clearly seen, the lowest R-factors are achieved for the pyramid-like structure model. Especially, the accordance to the high energy pattern Fe_{II} was significantly improved from $R_{\mathrm{Fe}_{II}}(bcc) = 0.58$ to $R_{\mathrm{Fe}_{II}}(\mathrm{pyramid}) = 0.07$. In comparison, the improvement for the low energy pattern Fe_I from $R_{\mathrm{Fe}_I}(bcc) = 0.12$ to $R_{\mathrm{Fe}_I}(\mathrm{pyramid}) = 0.05$ is smaller. This can be explained by the well bcc ordered Fe-surface, which has a stronger influence on the pattern due to the more surface sensitive energy of $E_{\mathrm{ph}} = 180\,\mathrm{eV}$. The interface sensitive measurement of $E_{\mathrm{ph}} = 320\,\mathrm{eV}$ reveals the pyramid-like structure strongly, because almost every layer has a lightly different lattice constant, which is not the case at the surface.
The resulting structure model of the Fe/GaAs-system is shown in Fig. 5.12 illustrating the pyramid-like grown Fe-film. The yellow triangles represent the elementary cells of the interface and surface lattices. As can be clearly seen, the bcc lattices are not centered to one another, underlined by the shifted apex of the triangles.

A XPD pattern show more detailed features of the structure the higher the kinetic photoelectron energy becomes [96]. In this thesis, neither the GaAs-substrate nor the higher energy of $E_{\mathrm{ph}} = 320\,\mathrm{eV}$ cause strongly detailed features in the Fe $3p$-pattern. This phenomenon is explained by a near-order of the Fe-atoms. The different lattice constants resulting from the pyramid-like structure lead to a destructive interference. On the other hand the local environment of one Fe-atom is identical due to the bcc structure. Hence, the near-order in the XPD pattern illustrating the main reflexes caused by the bcc-structure confirms the tetragonal distorsion of the Fe-film.

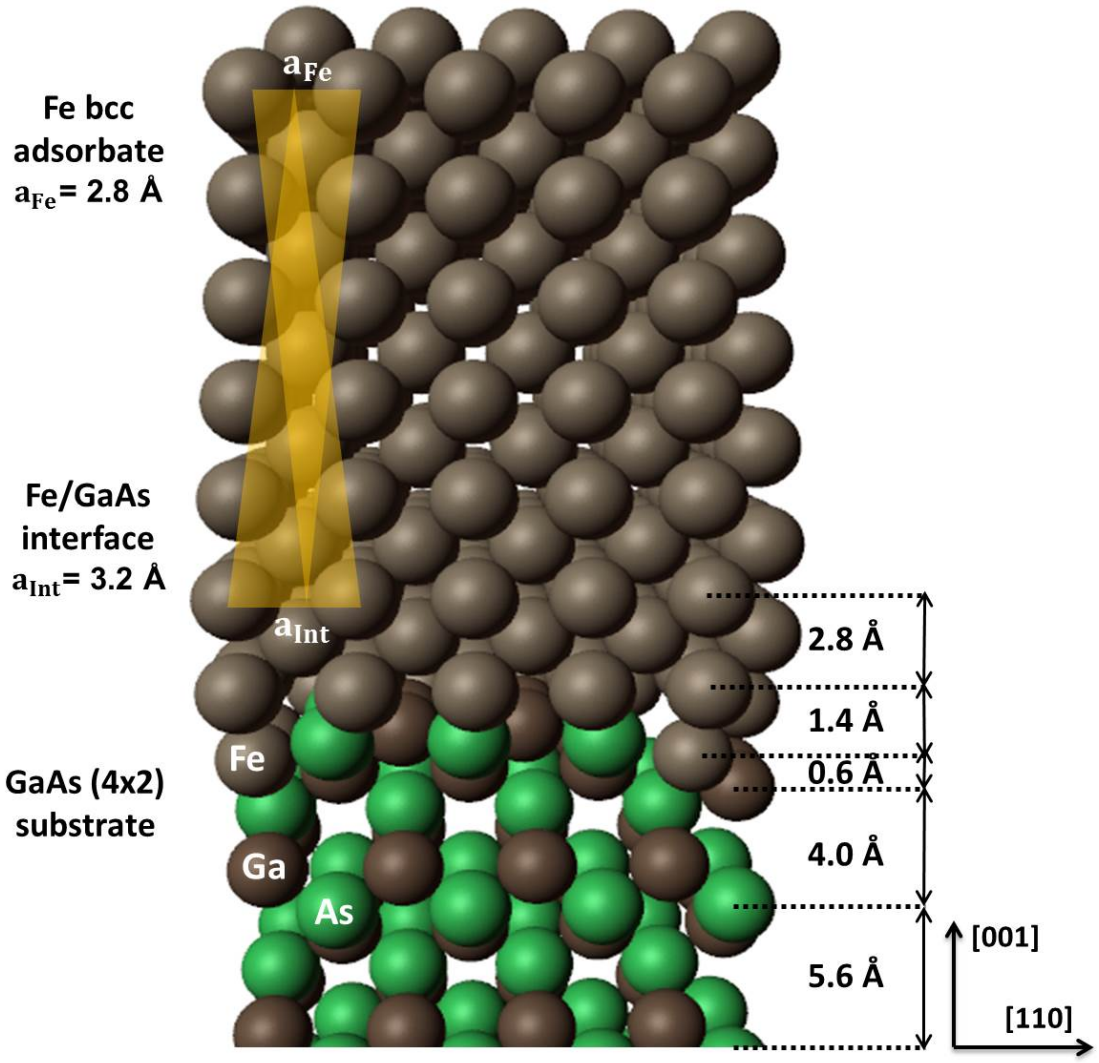

Figure 5.12: Illustration of the structure model of the Fe/GaAs(4×2)-system. The bcc structured Fe-film is located on top of the (4×2)-reconstructed GaAs(001)-substrate. The yellow triangles illustrate the shift between the interface and surface Iron layers. As can be seen, the apexes are not centered. The shift occurs along the [110]-direction and is amount to 0.4 Å with respect to the lattice constant of bcc-Fe $a_{\mathrm{Fe}} = 2.8$ Å. (As: green, Ga: brown, Fe: gray)

5.2 MgO/Fe-interface

Magnesium-oxide was deposited on the Fe/GaAs(4×2)-system as being the topmost film of the multilayer system. The survey scan directly detected after the deposition of the third layer is shown in Fig. 5.13. The Mg $2p$ and O $1s$ signals originating from the MgO are clearly visible additionally to the core level signals of the GaAs-substrate and Fe-interlayer. No Carbon signal occurs, which reveals the MgO-growth on the sample without any contaminations.

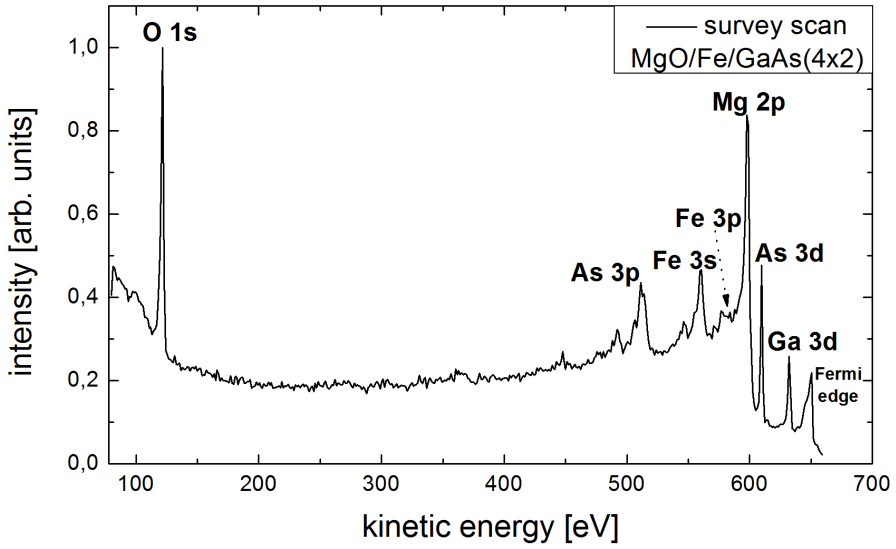

Figure 5.13: Survey scan of the three layer system MgO/Fe/GaAs(001) detected at $E_{\mathrm{ph}} = 650\,\mathrm{eV}$ and $\theta = 0°$.

5.2.1 XPS analysis

The XPS core level signals of Mg $2p$ and Fe $3p$ are separated by a few electron volt only, as shown in Fig. 5.14. As mentioned before, a p-level split into $p_{3/2}$ and $p_{1/2}$ with a height ratio of $h_{\mathrm{LS}}(p) = 1/2$. The energy shift caused by the spin-orbit coupling is $f_{\mathrm{LS}}(Mg2p) = 0.28\,\mathrm{eV}$ [97] and $f_{\mathrm{LS}}(Fe3p) = 0.80\,\mathrm{eV}$ for Mg $2p$ and Fe $3p$, respectively. The energy positions are marked according to the Mg $2p_{3/2}$ and Fe $3p_{3/2}$ levels. The fitted high-resolution spectra are shown in Fig. 5.14 (a) and (b) for the two polar angles $\theta = 0°$ and $\theta = 60°$, respectively.

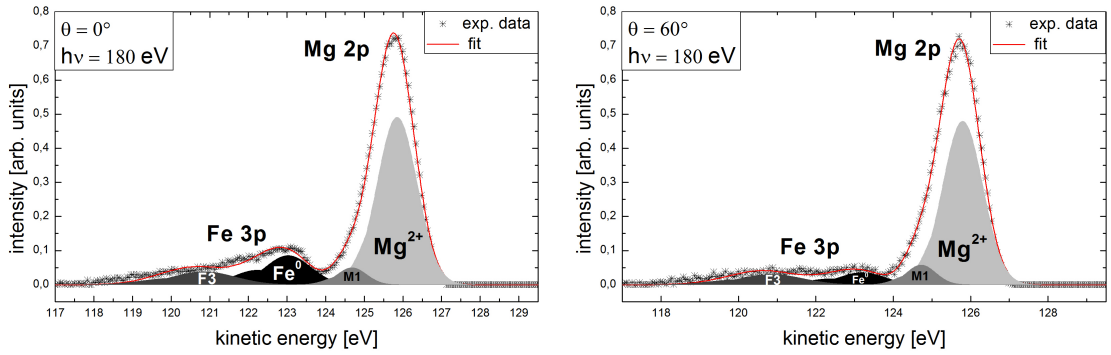

(a) (b)

Figure 5.14: High-resolution XPS spectra of Mg $2p$ and Fe $3p$ core-level at $\theta = 0°$ (a) and $\theta = 60°$ (b). The photon energy was set to $E_{\mathrm{ph}} = 180\,\mathrm{eV}$.

In general, the Fe $3p$-peak decreases strongly for increasing polar angles, which directly demonstrate that the MgO-film forms the topmost layers of the system. The overlap of Fe $3p$ and Mg $2p$ enlarges the Gaussian extension once more and justifies the use of the Gauß fit-function (2.9) for the Fe-signals in order to get comparable results. The best least squares fit using the Gaussian function resulted in two components for each individual signal.

The Mg $2p$ signal consists of a strong component Mg^{2+} located at $E_{\mathrm{kin}}(Mg^{2+}) = 125.86\,\mathrm{eV}$ and the component $M1$ at $E_{\mathrm{kin}}(M1) = 124.68\,\mathrm{eV}$. This small component was essential for reaching an excellent accordance between experimental data and fitting curve in the range of the overlap. The dominance of the Mg^{2+}-state is due to the twofold ionization of Magnesium in the chemical bond of Magnesium oxide. The component $M1$ is shifted about $\Delta E_{\mathrm{M1}} = 0.18\,\mathrm{eV}$ to lower kinetic energies with respect to Mg^{2+}. The intensity ratio between the Fe $3p$-signal and $M1$ increases for increasing polar angle, but keep almost constant between M^{2+} and $M1$. This shows, that the component $M1$ originates from bonds located between the Fe-interlayer and the topmost MgO-layers. Therefore, it can be related to a bonding between Magnesium oxide and Iron in the interface. The polar angle independent Mg^{2+}-signal can be explained by the very thin MgO-film.

The Fe $3p$-signal consists of one component at $E_{\mathrm{kin}}(Fe^0) = 123.03\,\mathrm{eV}$ and another at $E_{\mathrm{kin}}(F3) = 120.85\,\mathrm{eV}$. The component Fe^0 can be related to the signal of pure Iron by minding the size of the signal and the consequent enlargement, as well a measure and numerical uncertainty. The additional component $F3$ is shifted about $\Delta E_{\mathrm{F3}} = 2.18\,\mathrm{eV}$ to lower kinetic energies and increase for increasing polar angles

with respect to Fe^0. It corresponds to the ionized Fe^{1+}-state of an oxidized Fe-film and is located in the interface between MgO and Fe. The survey scan of Fe/GaAs in Fig. 5.1 reveals no oxygen signal, which confirms no oxidation of the Fe-surface. Therefore, the oxide-state $F3$ of the Fe-interlayer can be explained by an oxidation due to the deposition of MgO. An oxidized Iron-layer after a deposition of Magnesium oxide was proposed in several works previously [98, 99].
The parameters of the best least squares fits for Fe $3p$ and Mg $2p$ are summarized in Tab. 5.4.

component	kinetic energy [eV]	FWHM [eV]	SOC [eV]
Mg^{2+}	125.86	0.50	0.28
M1	124.68	0.35	0.28
Fe^0	123.03	0.57	0.80
F3	120.85	0.79	0.80

Table 5.4: Parameters of the best least squares fit for Mg $2p$ and Fe $3p$-core levels of the MgO/Fe-system. The photon energy was amount to $h\nu = 180\,\text{eV}$.

The deposited MgO-film bond to the Fe-layers displayed by the small component $M1$ and $F3$. The oxidation of the Iron leads to the assumption, that the MgO-film could be amorphous. This is examined by the following XPD analysis.

5.2.2 XPD analysis

The Mg $2p$ and Fe $3p$ XPS signals overlay, as it was discussed in the section before. Due to this overlap the experimental XPD pattern is a superposition of both intensities. The resulting pattern is illustrated in Fig. 5.15 (a) and show a fourfold rotational symmetry.

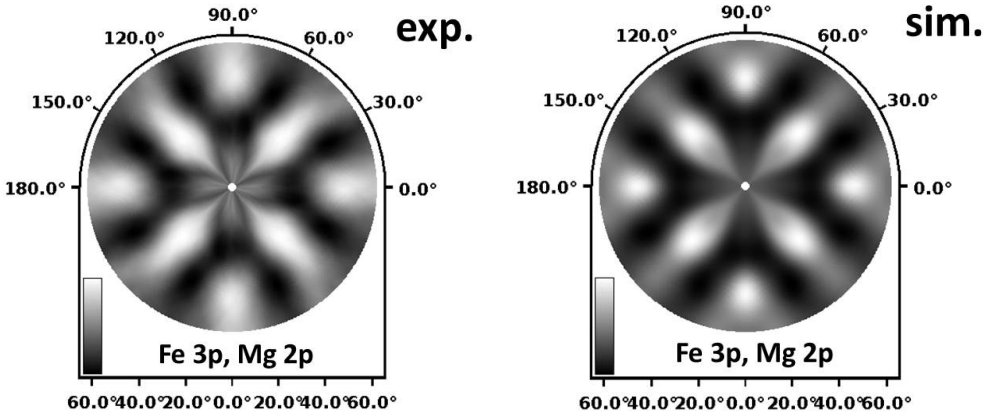

(a) (b) $R_{\mathrm{sup}} = 0.04$

Figure 5.15: Experimental (a) and best simulated XPD pattern (b) of the superposition of Mg $2p$ and Fe $3p$ signals.

For analyzing the structure of the MgO-film, Fe-interlayer, and its interface the experimental pattern was separated into two individual patterns related to the Mg $2p$ and Fe $3p$ photoelectron signal. Therefore, the 6000 individual XPS-signals yielding the XPD pattern are separated into two kinetic energy parts $E_{\mathrm{kin}} = 117\,\mathrm{eV} - 124\,\mathrm{eV}$ relating to Fe $3p$ and $E_{\mathrm{kin}} = 124\,\mathrm{eV} - 130\,\mathrm{eV}$ relating to Mg $2p$-signal. However, a perfect separation is not possible due to a overlap of the components, because they are Gaussian in energy. The truncation and the overlap are schematically illustrated in Fig. 5.16. The truncated experimental patterns related to Mg $2p$ and Fe $3p$ signal are shown in Fig. 5.17 (a) and (c), respectively.

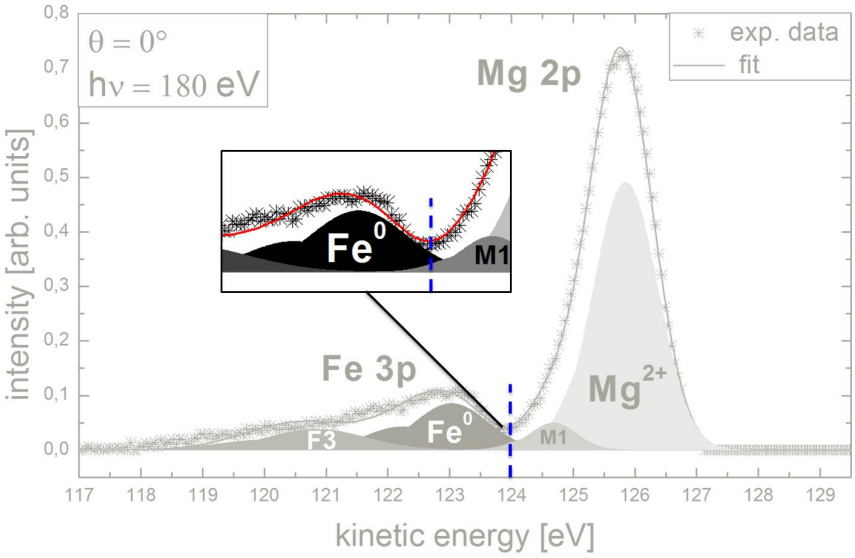

(a) $\theta = 0°$

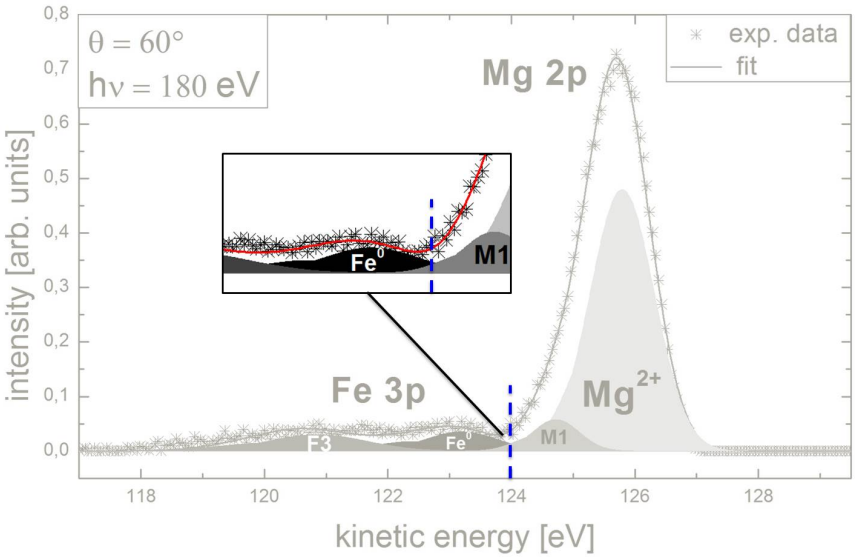

(b) $\theta = 60°$

Figure 5.16: Illustration of the truncation between the Mg 2*p* and Fe 3*p* intensities. The XPS signals yielding the XPD pattern are separated into two parts represented by the dashed blue line. The insets are enlarged picture to elucidate the overlap of the Mg 2*p* and Fe 3*p* XPS signals due to their Gaussian in energy and the energy position of truncation.

Both of the truncated patterns show a fourfold rotational symmetry and are analyzed successively. However, the goal is to find one structure model, which agrees with the two individual patterns as well as with the superposition.

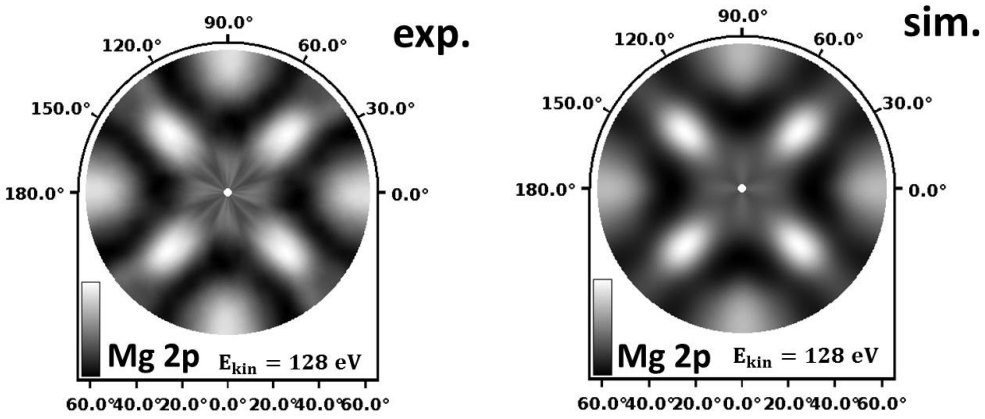

(a) (b) $R_{\mathrm{Mg}} = 0.03$

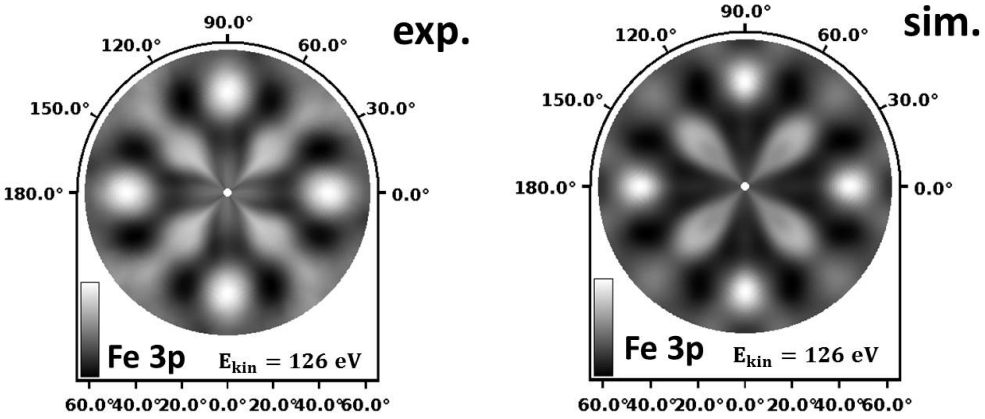

(c) (d) $R_{\mathrm{Fe_{MgO}}} = 0.06$

Figure 5.17: Experimental and best simulated XPD pattern of the truncated Mg $2p$ pattern (c) and (d), and Fe $3p$ pattern (d) and (f), respectively.

As a starting structure model for the MgO-film a halite structure with the lattice constant of bulk MgO $a_{\mathrm{MgO}} = 4.2\,\text{Å}$ is assumed. This simulation resulted in a bad agreement of $R_{\mathrm{halite}} = 1.14$ and is shown comparative to the experimental data in Fig. 5.18.

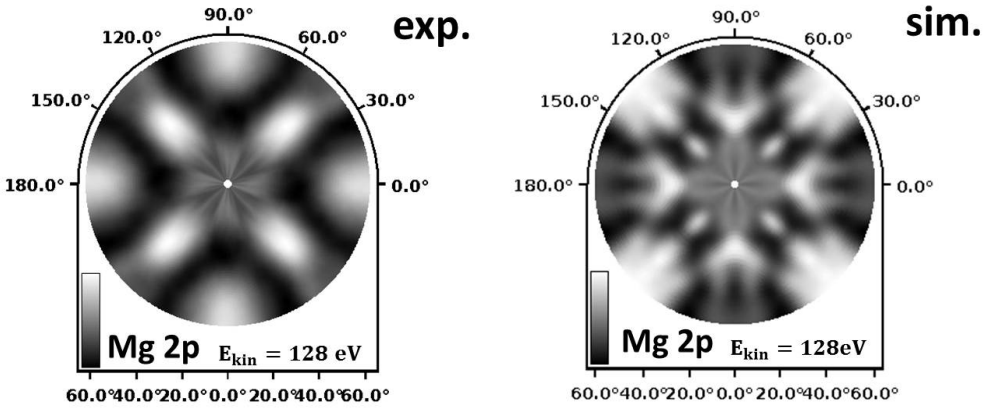

(a) (b) $R_{\mathrm{halite}} = 1.14$

Figure 5.18: Comparison of experimental XPD pattern of Mg 2p (a) and the simulated pattern for a pure halite structured MgO-film (b).

Nevertheless, a first important finding is the 45° rotation of the strongest intensities with respect to the experimental pattern. This is the result of the epitaxial correlation between the Fe(001) and MgO(001) surfaces [100, 101]. The very thin MgO-film and the non-prefect separation of the intensities induce a structure model of MgO on top of a Fe-film. The analysis in Sec. 5.1.2 results in a pyramidal bcc structured Fe-layer. However, the Fe surface layers are well ordered with the known lattice constant of $a_{Fe} = 2.8\,\text{Å}$, so the Fe/GaAs interface structure is not expected to influence the MgO/Fe-film. Hence a model consisting of a bcc structured Fe-layer with a 45°-rotated MgO-film on the top was build. The cluster size for these simulations was around 50 atoms. In fact, the simulation of this modified structure resulted in an improved accordance to the Mg 2p with $R_{\mathrm{Mg}} < 1$.
In order to achieve further improvement the genetic algorithm described in Sec. 2.2.2 was applied for the Mg 2p pattern. It yielded in a structure of the MgO-film, where every second Mg-layer is slightly shifted with respect to the other layers. The shift s is along the [110]-direction of the MgO/Fe-system. In Fig. 5.19 (a) the R-factors for various amounts of the lateral shift are illustrated.

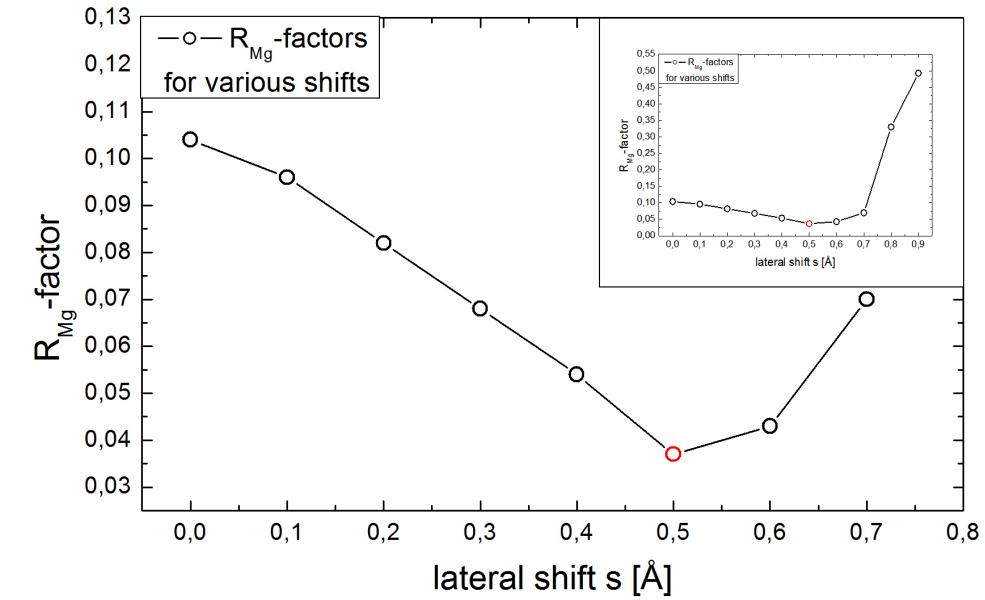

(a)

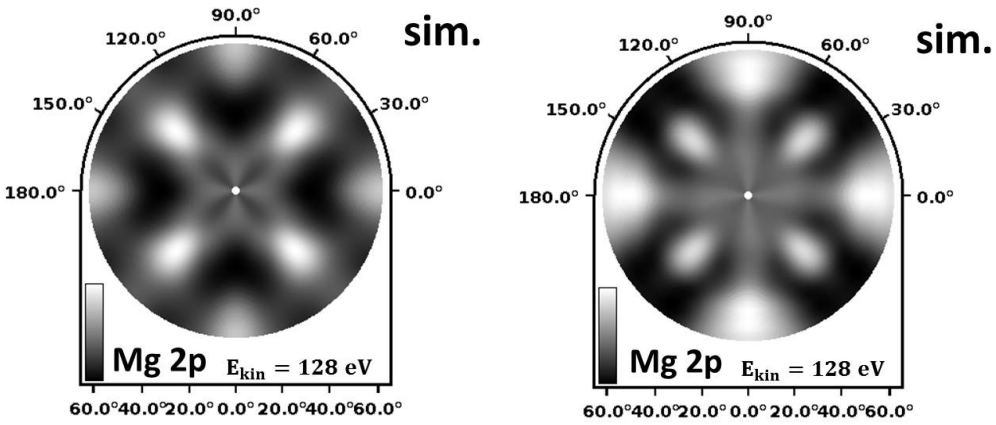

(b) $R_{\mathrm{Mg}} = 0.10$ (c) $R_{\mathrm{Mg}} = 0.33$

Figure 5.19: Illustration of the R_{Mg}-factors for various value of the lateral shift of the Mg-atoms. The red dot represents the best simulated Mg 2p-pattern shown in Fig. 5.17 (b). In the inset, the strong increase for shifts $s > 0.7$ Å are pictured. Exemplary the simulated Mg 2p pattern for no lateral shift (b) and a lateral shift of $s = 0.8$ Å (c) of the Mg-atoms are shown.

As can be clearly seen the minimum is found at $s = 0.5$ Å represented by the red circle. Additionally, two simulated Mg 2p XPD patterns are shown exemplary for a completely symmetric MgO-film of $s = 0$ Å and a lateral shift of $s = 0.8$ Å. The differences between these patterns shown in Fig. 5.19 (b),(c) and the experimental Mg

2p-pattern are significantly, displayed by R-factors of $R_{\mathrm{Mg}} = 0.1$ and $R_{\mathrm{Mg}} = 0.33$, respectively. The modified structure model based on the considerations yielded in a very good agreement between the simulated and experimental Mg 2p pattern with $R_{\mathrm{Mg}} = 0.05$. The lateral shift can be explained by a misfit dislocation of the Mg-atoms within the MgO-film.

In a next step the Fe 3p pattern was simulated by using a cluster based on the structure model found from the Mg 2p analysis. However, an R-factor analysis between experimental Fe 3p data and the simulation resulted in a rather poor agreement. A comparison between the low energy pattern Fe_I of Fe 3p of the Fe/GaAs(4×2)-system and the one of the MgO/Fe/GaAs(4×2)-system displays almost the same reflexes as shown in Fig. 5.20. However, an R-factor analysis resulted in $R_{\mathrm{diff}}(Fe) = 0.07$ revealing a distinct difference.

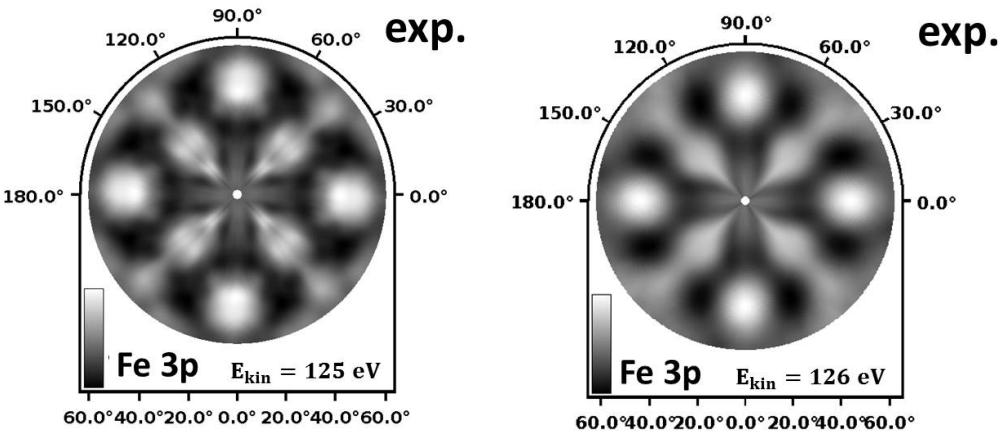

(a) Fe-film (b) Fe-interlayer

Figure 5.20: Comparison of Fe 3p XPD patterns before (a) and after (b) MgO-deposition. An R-factor analysis resulted in $R_{\mathrm{diff}} = 0.07$.

The Fe-film was not oxidized before the MgO was deposited, which is shown by the survey scan in Fig. 5.1 (b). To the contrary the high-resolution XPS spectra of Mg 2p and Fe 3p after the MgO-deposition shown in Fig. 5.14 reveal an oxidation of the Fe-surface, which explain the difference. An oxidation of the Fe-surface after the deposition of MgO was introduced by several works from calculations and x-ray diffraction measurements [99, 102]. Hence, several FeO-layers were added to the structure model resulted from the Mg 2p XPD pattern. The best agreement between experimental and simulated Fe 3p pattern of the MgO/Fe-system was achieved with

a two layer thick FeO-interface. The Oxygen atoms are located in the first and second Fe-layer. They serve as a bond between the Fe-interlayer and the MgO-film. Further, this explain the small component $M1$ of the Mg $2p$ XPS spectra to be Mg-atoms, which share one O-atom with the Fe-surface. The R-factor analysis resulted a very good agreement of $R_{\mathrm{Fe_{MgO}}} = 0.08$ for the Fe $3p$ pattern. In this thesis, more or less than two FeO-layers deteriorate the agreement between the simulated patterns and the experimental data greatly. Further, a simulation of the Mg $2p$ pattern based on the FeO modified structure model was performed. In fact, it revealed an improved accordance of $R_{\mathrm{Mg}} = 0.04$, too.

As described in chapter 5.1.2, the Fe-interlayer was found in a pyramid-like structure indicated by the simultaneously layer and island growth. The topmost MgO-layer is very thin with almost $d_{\mathrm{MgO}} \approx 4.6\,\text{Å}$ and the influence of the FeO-surface on the MgO-film was already shown. Therefore, the structure model was adjusted, by minding the pyramid-like structure of the Fe-interlayer, but a well ordered Fe-surface with two FeO-layers, to examine the influence of the Fe/GaAs-interface on the MgO/FeO/Fe-system. Indeed, a comparison between these simulations and the experimental Mg $2p$ and Fe $3p$ patterns yielded in an excellent agreement. This is elucidated by very small R-Factors of $R_{\mathrm{Mg}} = 0.03$ and $R_{\mathrm{Fe_{MgO}}} = 0.06$. These two best simulated patterns of Magnesium and Iron for the discussed structure model are shown in Fig. 5.17 (b) and (d), respectively. In order to examine the presence of the Mg-atom shift, simulations with various shift were performed anew but using the MgO/FeO/Fe(pyramid)-system. Indeed, the best accordance was again achieved for a lateral shift of $s = 0.5\,\text{Å}$.

The schematic picture of the final structure model for MgO/FeO/Fe is shown in Fig. 5.21. The green rectangle illustrates the centered cell of the system, whereas the red represents the cell of the shifted Mg-atoms. In the insets, increased pictures clearly illustrate the shift between these two cells. The interfacial Oxygen atoms are lightly shifted towards the first MgO-layer displaying to be the bonding atom between Fe and MgO.

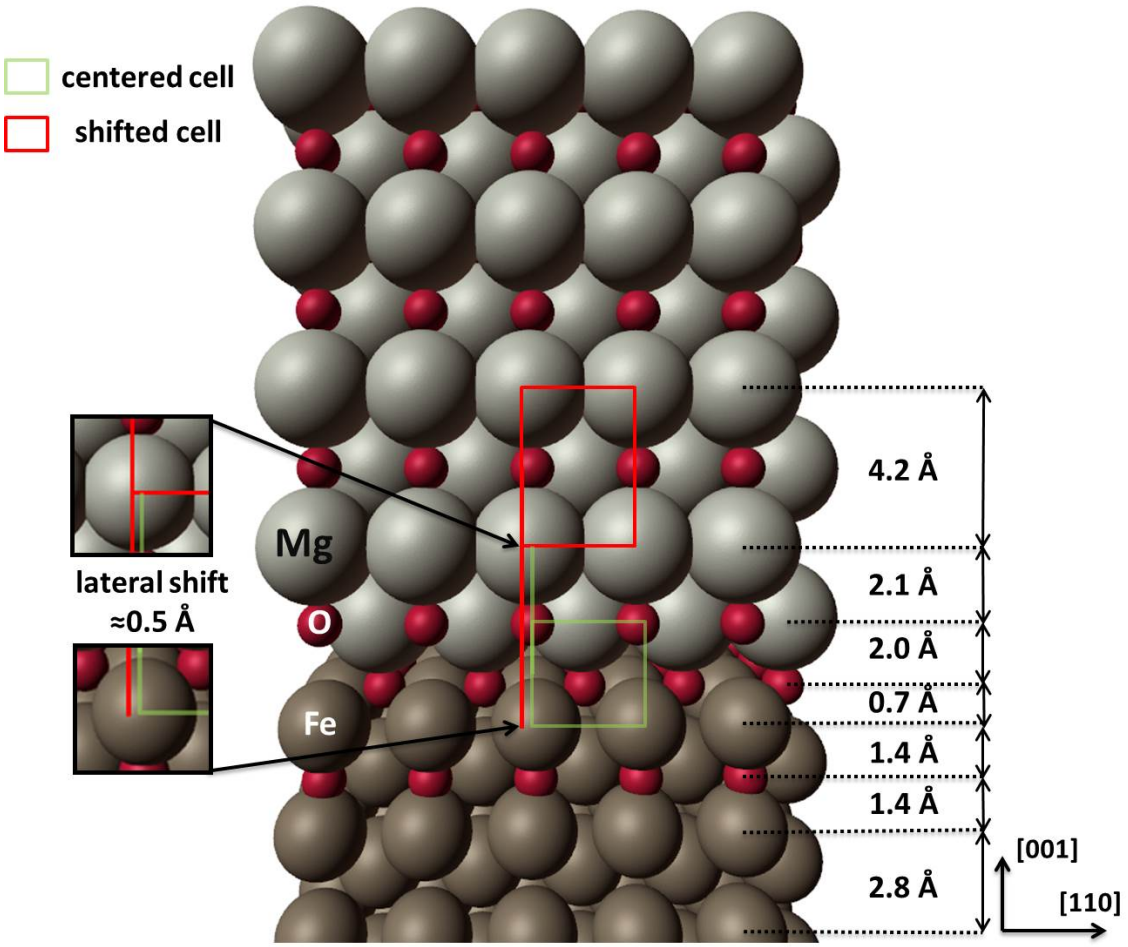

Figure 5.21: Schematic illustration of the structure model for the MgO/Fe-interface. The red and green rectangles display the cells of the shifted Mg-atoms and the centered cell of the system, respectively. As can be seen in the insets they do not lie on top of each other illustrating the 0.5 Å-shift along the [110]-direction. (Mg: white, O: magenta, Fe: gray)

In a final step the best simulated Mg 2*p* and Fe 3*p* XPD patterns are superimposed, in order to cross check the agreement to the original pattern shown in Fig. 5.15 (a). The R-factor analysis yielded in an excellent agreement with $R_{\mathrm{sup}} = 0.04$ for the superimposed pattern shown in Fig. 5.15 (b). This impressively reveals the significance of the described structure model of the MgO/Fe-interface.

The added pyramid-like structure of the Fe-interlayer found from the analysis in Sec. 5.1.2 significantly improved the agreement for the truncated Fe 3*p* XPD pattern. Furthermore, the influence on the Mg 2*p*-pattern is also apparent, although rather weak. This leads to the assumption, that the misfit of the MgO-film could be induced by the pyramid-like structure of the Fe-interlayer. This misfit is represented by a lateral shift of Mg-atoms. In literature, previous LEED investigations on MgO detected a misfit [103, 104], which disappeared for thicker films. Certainly, MgO is known to only grow crystalline on a Fe-substrate up to six monolayers due to the strong lattice mismatch of 3.8% [101, 105]. In order to verify this assumption a thicker MgO-film on the discussed Fe/GaAs(4 × 2)-substrate was prepared, see Sec. 5.1. Therefore, the evaporation time of the MgO crystal was increased to $t = 40\,\text{min}$. All other parameters were kept identical to the preparation described in Sec. 4.3. This results in a layer thickness of about $d_{\text{MgO}} \approx 13\,\text{Å}$ for the MgO-film.

First, high-resolution spectra according to Sec. 5.2.1 are recorded, which are shown in Fig. 5.22. As can be clearly seen the Fe 3*p*-signal at $E_{\text{kin}}(Fe) \approx 123\,\text{eV}$ is completely suppressed. A fitting procedure using the Gauß-function (2.9) resulted in exactly the same components Mg^{2+} and $M1$ as discussed in section 5.2.1 before. Hence, a detailed description is dispensed with here.
The resulting Mg 2*p* XPD pattern of the thick MgO-film is shown in Fig. 5.23 (a) and has a fourfold rotational symmetry. A simulation based on the structure model in Fig. 5.21 and described above resulted in an excellent agreement of $R_{\text{MgO}_{13}} = 0.07$. In order to verify this first result further simulations are performed. In fact, non of them resulted in agreements better than $R = 0.15$. Especially structures without the shift of Mg-atoms resulted in poor accordance. Vassnet *et al.* proposed a lattice misfit being the reason for an amorphous MgO-film on the Fe(001)-substrate thicker than six monolayers [101]. In this thesis, the MgO lattice misfit illustrated by the shifted Mg-atoms does not disappear for a three times thicker film. The misfit dislocation is not a feature of the interface structure and so probably not induced by the Fe-interlayer structure. Nevertheless, the shifted Mg-atoms might be the reason for only thin epitaxial MgO(001)-films on Fe(001)-substrates.

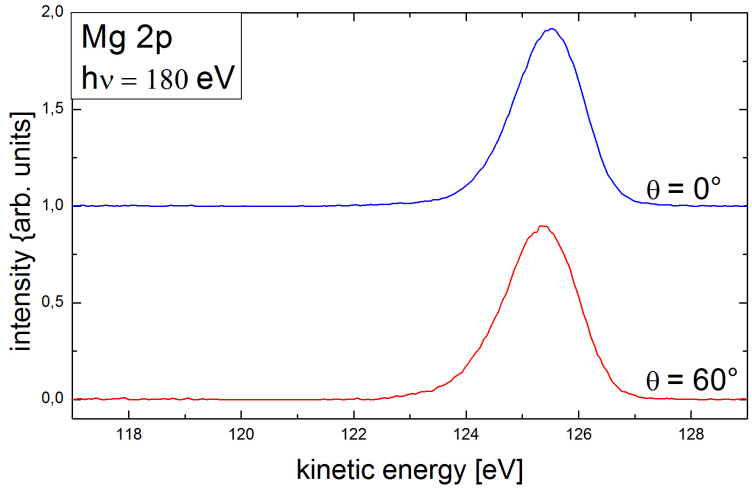

(a) $d_{\mathrm{MgO}} \approx 13\,\text{Å}$

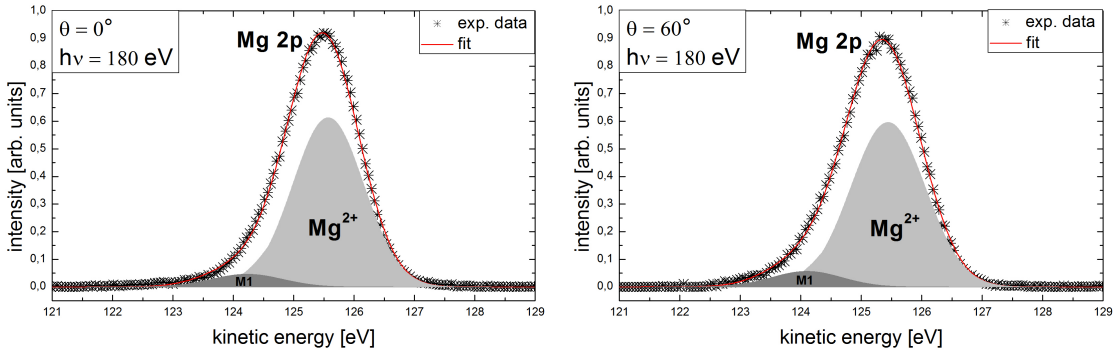

(b) (c)

Figure 5.22: XPS high-resolution spectra of a 13 Å-thick MgO film. Column (a) displays that the Fe 3*p*-signal is completely surpressed. The results of the fitting procedure are pictured in column (b) and (c). They yielded the identical information as the 4.6 Å-thin MgO film displayed in Fig. 5.14.

However, TMR-components require a thin and crystalline MgO-film. Both requirements were achieved during this thesis, as demonstrated by the XPD data. Despite the misfit, the MgO film was very stable over the full data acquisition time, which was verified by high resolution XPS spectra recorded at the beginning and the end of the measuring procedure. In these spectra no change in the intensity ratio or energy position of the Mg 2*p*-signal could be detected. The observed misfit indicated by the here shifted Mg layers could be an important hint for a stable but thin MgO-film growth on a Fe-substrate.

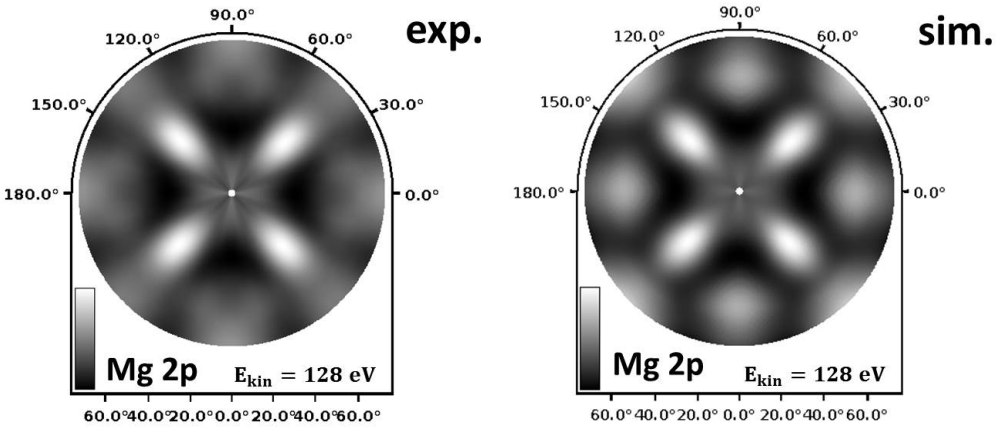

(a) (b) $R_{\mathrm{MgO}_{13}} = 0.07$

Figure 5.23: Comparison of Mg $2p$ experimental (a) and best simulated (b) XPD pattern of the 13 Å-thick MgO-film. The simulation was based on the described structure model shown in Fig. 5.21.

5.3 Magnetic properties

The pyramid-like structure of the Fe-interlayer and the oxidation of the Fe-surface due to the MgO-deposition raise the question, if the Fe-film has still its magnetic properties. Besides, the shifted Mg-atoms probably induce a magnetization and neglect the isolating character of the MgO-film. In order to examine if the structural and chemical modifications of the Fe-interlayer alter its magnetic properties, T-MOKE in reflection was applied, which allows an unproblematic investigation of partially oxidized buried magnetic films [67, 68].

After the XPS and XPD investigations the MgO/Fe/GaAs(4×2)-sample was transferred to the XMAPS chamber. Thereby the sample was exposed to air for a few minutes. However, the GaAs-substrate is completely covered, the MgO and the Fe-layers are already oxidized, and a contamination by carbon is rather weak.

In a first step, the relative reflectivity for two anti-parallel transversal magnetizations $R(B_T^{\pm})$ are measured. The incidence angle was set to $\alpha = 40°$ being streaking. This ensures a good information depth within the thin MgO- and Fe-films and a high T-MOKE signal at the same time. The external magnetic field flux density was set to $B_{\mathrm{T}} = \pm 450\,\mathrm{mT}$. This causes a magnetization of the sample parallel to the external field. The spectra of the two reflectivities as a function of the incoming photon energy are shown in Fig. 5.24.

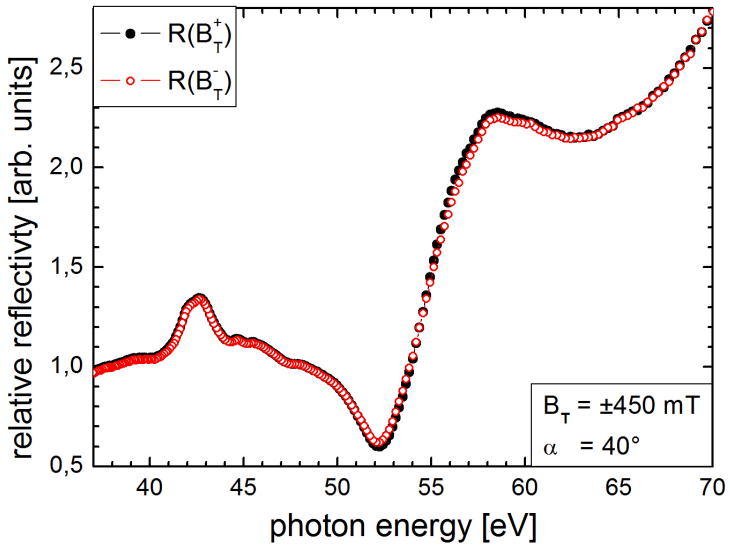

(a)

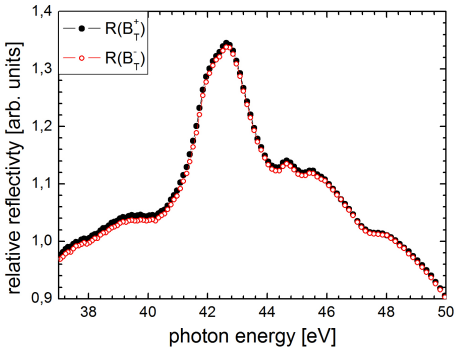

(b) As 3*d* edge

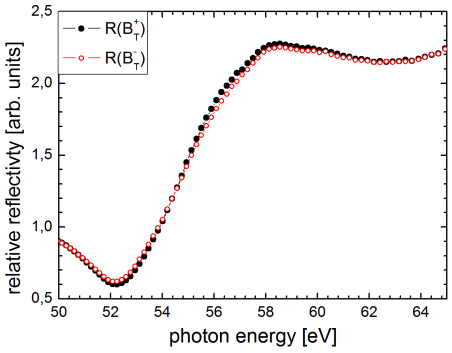

(c) Fe 3*p* edge

Figure 5.24: Relative reflectivity spectra of the MgO/Fe/GaAs sample. The black and red curves represent the reflectivity for the positive $R(B_T^+)$ and negative $R(B_T^-)$ external magnetic field, respectively. A closer look to the As 3*d* and Fe 3*p* edge is shown in column (b) and (c), respectively. Thereby, a different behaviour of $R(B_T^\pm)$ at these two edges can be observed.

In the spectra a small signal occurs at $E_{\mathrm{ph}} \simeq 42\,\mathrm{eV}$, which can be related to the As 3*d*-edge. At about $E_{\mathrm{ph}} \simeq 53\,\mathrm{eV}$ a strong structure appears corresponding to the Fe 3*p*-edge. Only a very weak shoulder arises in the energy-range of $E_{\mathrm{ph}} \simeq 49\,\mathrm{eV}$, where the Mg 2*p*-edge is expected. This might be due to the small layer thickness of the MgO-film. The reflectivity spectra corresponding to the positive (black) and negative (red) magnetic field alignment differ clearly from each other at the Fe-edge.

Meanwhile they lay almost one on top of the other at the As- and Mg-edge. This *asymmetry* illustrates the reaction of the Iron to the external B-field, but a rather weak reaction of the Arsenic. The resulting T-MOKE asymmetry spectrum obtained from the relative reflectivity of the sample using Eq. (2.21) is shown in Fig. 5.25.

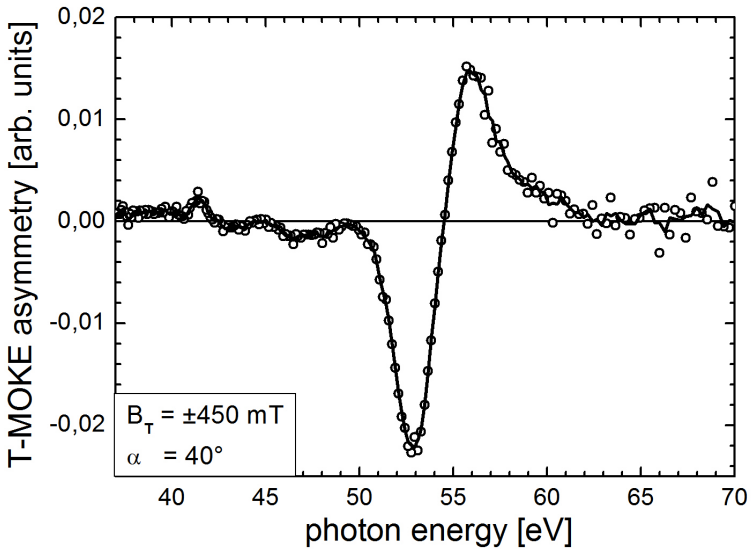

Figure 5.25: T-MOKE asymmetry spectrum calculated from the relative reflectivity spectra shown in Fig. 5.24.

Obviously, the T-MOKE asymmetry spectrum has a strong double lobe structure at around $E_{\mathrm{ph}} \simeq 54.5\,\mathrm{eV}$. This directly reflects a strong dependence on the external B-field in this energy range. It corresponds to the Fe $3p$-edge and confirms the strong reaction of the Fe-interlayer on the external magnetic field. Furthermore, it is in excellent accordance with the XPD results that only a small part of the Fe-film is oxidized. The chemical and structural modifications seems to do not destroy the ferromagnetic properties of the remaining Iron bulk.
At around $E_{\mathrm{ph}} \approx 41\,\mathrm{eV}$ an additional structure is visible within the asymmetry spectrum, which can be related to the As $3d$-edge. Regarding to the Fe-signal it is very small indicating a rather weak magnetic dependence. However, further investigation on the magnetic behavior of the Arsenic yielded no results.
Recently, no structure can be detected in the T-MOKE asymmetry spectrum at $E_{\mathrm{ph}} \approx 50\,\mathrm{eV}$ where the Mg $2p$-edge is expected. This indicates the MgO-film without ferromagnetic properties.

In order to verify the ferromagnetic characteristics of the Fe-film, a conclusive T-MOKE hysteresis measurement was performed. This hysteresis is shown in Fig. 5.26. The lightly relative intensity shift of the hysteresis loop could be explained by a misalignment of TetraMag, see Sec. 3.1. The lines illustrate a lightly smoothing of the experimental data and serve as a guide to the eye.

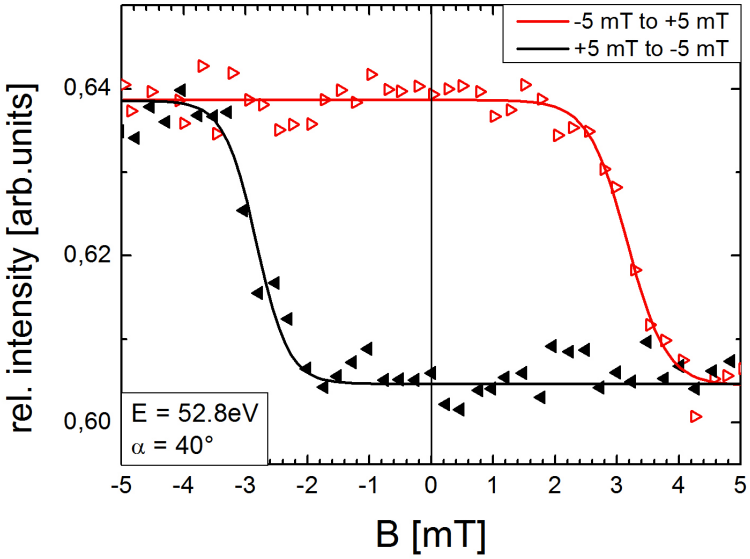

Figure 5.26: Hysteresis performed for the Fe-interlayer at $E = 52.8\,\mathrm{eV}$ and $\alpha = 40°$. The red curve displays the variation of $-5\,\mathrm{mT} \leq B_\mathrm{T} \leq +5\,\mathrm{mT}$ and the black curve $+5\,\mathrm{mT} \leq B_T \leq -5\,\mathrm{mT}$. The lines serve as a guide to the eye for the hysteresis shape, only.

The external magnetic field was aligned parallel to the magnetic easy $\langle 100 \rangle$-direction of bcc-Fe and varied in the range of $B_\mathrm{T} \pm 5\,\mathrm{mT}$. The T-MOKE asymmetry spectrum shows the maximum at around $E_\mathrm{ph} = 52.8\,\mathrm{eV}$, so this energy was used for the hysteresis measurements. The hysteresis measurement revealed a saturation field of $B_\mathrm{S} = 4\,\mathrm{mT}$ for the Fe-interlayer. The strength of this saturation filed is in an excellent agreement with results reported recently on crystalline Fe on GaAs(001) [106]. Furthermore, the center of the hysteresis curve is found at $B_T = 0\,\mathrm{mT}$. This clearly indicates that neither the FeO-layers nor the MgO-film are anti-ferromagnetic at room temperature. The linking of a ferromagnet to an anti-ferromagnet, like FeO on Fe or MgO on Fe, would cause an exchange bias [107]. The exchange bias effected a preferred magnetization direction within the ferromagnet, which resulted in a shift of the hysteresis curve to one side. This is not the case in this thesis for

the Fe-interlayer of the MgO/Fe/GaAs-system. Additionally, the Fe-film has still an in-plane magnetization. Otherwise, an out-off plane oriented direction of the magnetization would result in a distorted hysteresis loop at $B_{\mathrm{T}} = 0\,\mathrm{mT}$, which was for example observed for Fe/MgO-systems [108].
Further hysteresis measurements up to $B = \pm 450\,\mathrm{mT}$ resulted in no additional information of the magnetic properties.

The T-MOKE investigation directly confirm that neither the oxidized surface due to the MgO-deposition, nor the pyramid-like Fe/GaAs interface structure diminish the excellent ferromagnetic properties of the Fe-film. Additionally, no magnetization is being induced by the ferromagnetic Fe-interlayer to the non-magnetic MgO-film. This is clearly demonstrated by the lack of a T-MOKE asymmetry of a MgO-signal. Further, the T-MOKE analysis reveals no ferromagnetic properties of the GaAs-substrate nor the MgO-film due to the missing exchange bias.

5.4 Fe-deposition on a clean GaAs(001)-surface

During this thesis, the question about the need of the GaAs(001) reconstruction to ensure an epitaxial Fe growth arises. In order to examine the assumption, Iron was evaporated on a clean but unreconstructed GaAs-surface. The GaAs sample was cleaned as described in Sec. 4.1.
Figure 5.27 shows a survey scan, which was directly recorded after the Fe-deposition on a clean GaAs(001) surface. The evaporation parameters were identical to the preparation of the Fe-film on GaAs(4 × 2), see Sec. 4.2. The Fe 3*p*-signal clearly revealed that Iron is located on the unreconstructed GaAs sample.

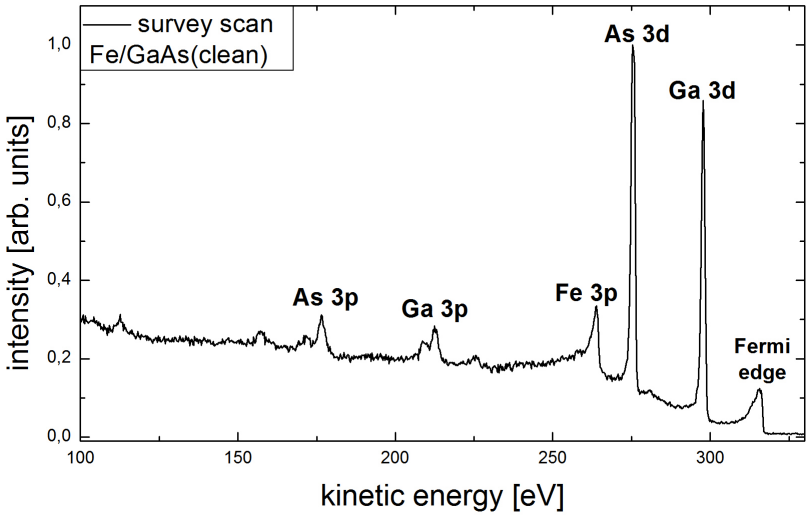

Figure 5.27: Survey scan of the Fe/GaAs-system with a clean but unreconstructed GaAs(001)-surface at $\theta = 0°$ and $E_{\mathrm{ph}} = 320\,\mathrm{eV}$.

XPS analysis

High-resolution spectra of the As 3*d* and Ga 3*d* core levels were directly detected after the cleaning procedure and the Fe-deposition. Then, an XPS analysis as described in section 5.1.1 has been performed. During the analysis, the spectra were compared to the spectra of the GaAs(4 × 2)-reconstruction, because the various reconstructions show individual XPS spectra [83, 109]. They are shown in Fig. 5.28.

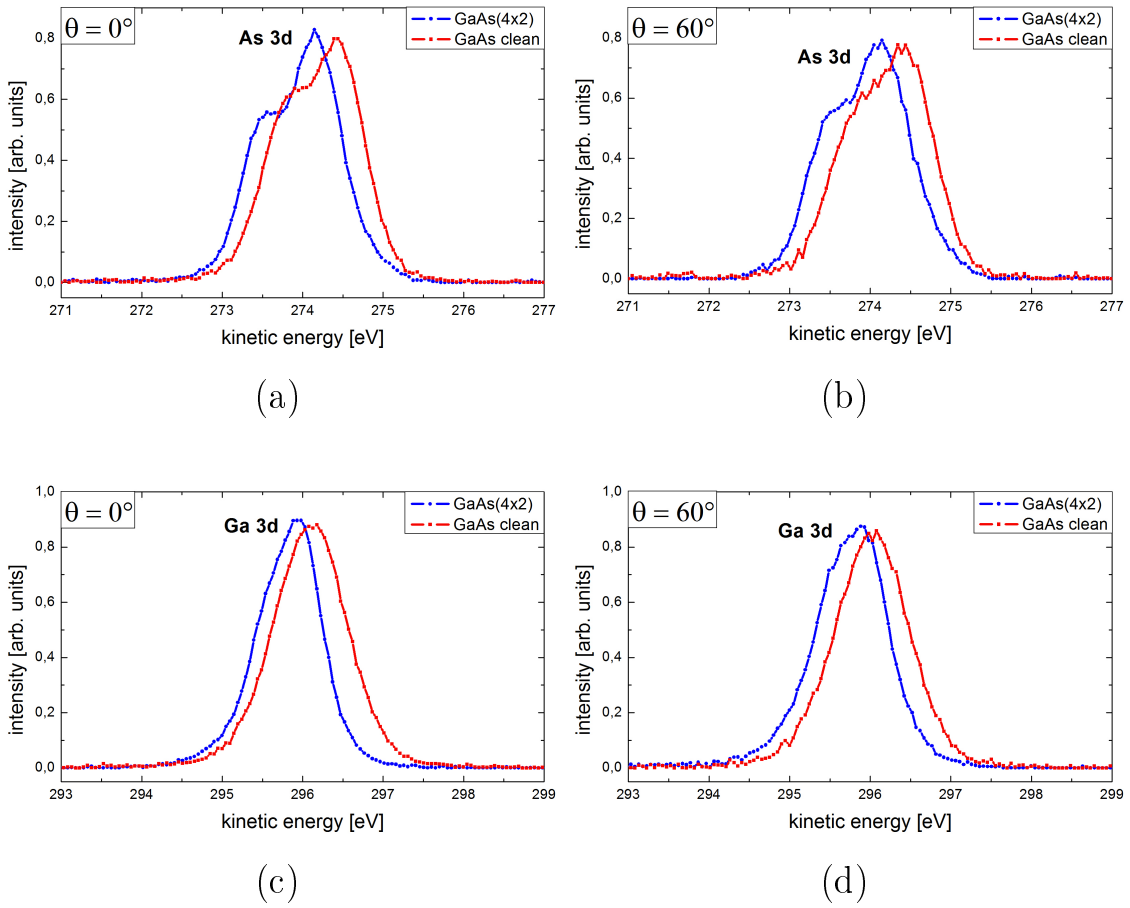

Figure 5.28: Comparison of high-resolution spectra of pristine and GaAs(4 × 2)-reconstructed surface, the As 3*d* signal (a), (b) and the Ga 3*d* signal (c),(d) recorded at $h\nu = 320\,\mathrm{eV}$.

As can be seen in these figures, the line shapes clearly differ to each other. The signals plotted in blue correspond to the GaAs(4 × 2)-surface and show the characteristic line shape of this reconstruction [80, 83]. Especially, the shoulder of the As 3*d* signal at around $E_{\mathrm{kin}} \approx 273\,\mathrm{eV}$ is a strong indication of the (4×2)-reconstruction. Again, this demonstrates a successful preparation of reconstructed and clean GaAs-surfaces.

Certainly, an amorphous surface results in various defects, correlated to different energetic states. Within an XPS spectrum the signals are superimposed displaying slight differences in the photoelectron signals at different sample positions. The surface of the GaAs(clean) sample is amorphous and a LEED pattern does not show any surface periodicity as discussed in Sec. 3.6 and Sec. 4.1. Hence, an analysis based on a Gaussian fit procedure applied to the XPS signals of the clean GaAs-

sample is not containing further new information. Nevertheless, least squares fits were performed in order to elucidate the changes within the bonding states due to the deposition of Iron.

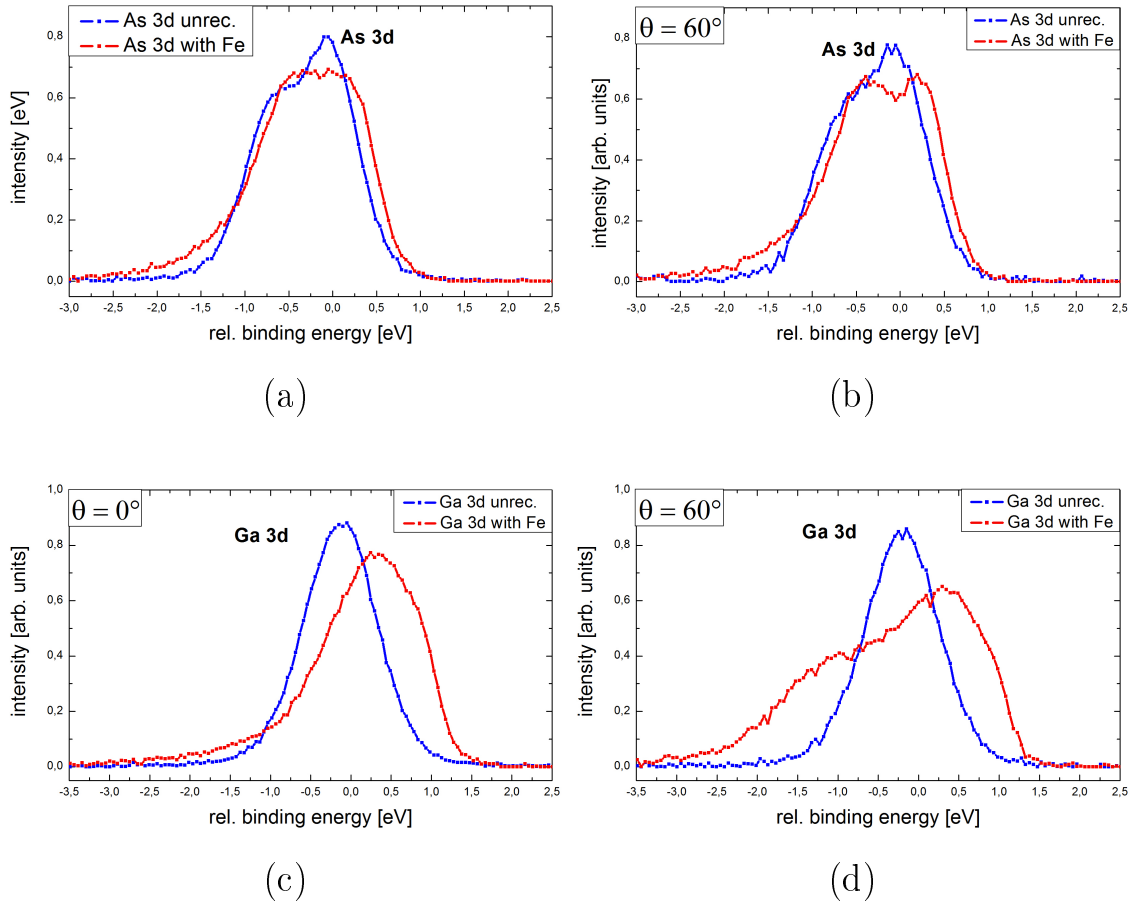

Figure 5.29: Comparison of the high-resolution XPS spectra of the core levels As 3*d* (a), (b) and Ga 3*d* (c), (d) of the clean GaAs(001) sample (blue) and after the Fe-deposition (red). The photon energy was set to $E_{\mathrm{ph}} = 320\,\mathrm{eV}$.

A comparison of the line shapes before and after Fe-deposition revealed a strong change for both the As 3*d* and Ga 3*d* signals. They are shown in Fig. 5.29 for polar angles of $\theta = 0°$ and $\theta = 60°$. For the amorphous surface, a small shift in binding energy of the single components were observed, even for an azimuth angle rotation only. Therefore, the parameters listed in Tab. 5.5 and obtained by the Gaussian fitting procedure represent averaged values. The following quantitative discussion serves as an illustration of the strong chemical changes at the GaAs(clean)-surface resulting from Fe-deposition.

system	component	kinetic energy [eV]	FWHM [eV]	SOC [eV]
clean GaAs	As bulk	274.5	0.3	0.69
	Ga bulk	296.3	0.4	0.45
Fe/GaAs	As bulk	274.7	0.3	0.69
	A1*	274.0	0.4	0.69
	A2*	274.5	0.3	0.69
Fe/GaAs	Ga bulk	296.8	0.4	0.45
	G1*	295.5	0.7	0.45

Table 5.5: Parameters of the 3*d* signals of clean GaAs before and after Fe-deposition. The values of kinetic energy and FWHM have been obtained by averaging over several azimuth angles.

The best accordance between experimental data and the fit procedure using the Gauß function in Eq. (2.9) resulted in one component for each of the As 3*d* and Ga 3*d* core level signals. They can be associated to the bulk signals of Arsenic and Gallium in the compound of GaAs. The difference in kinetic energy compared to the results presented in Sec. 5.1.1 can be explained by the different surface structures.

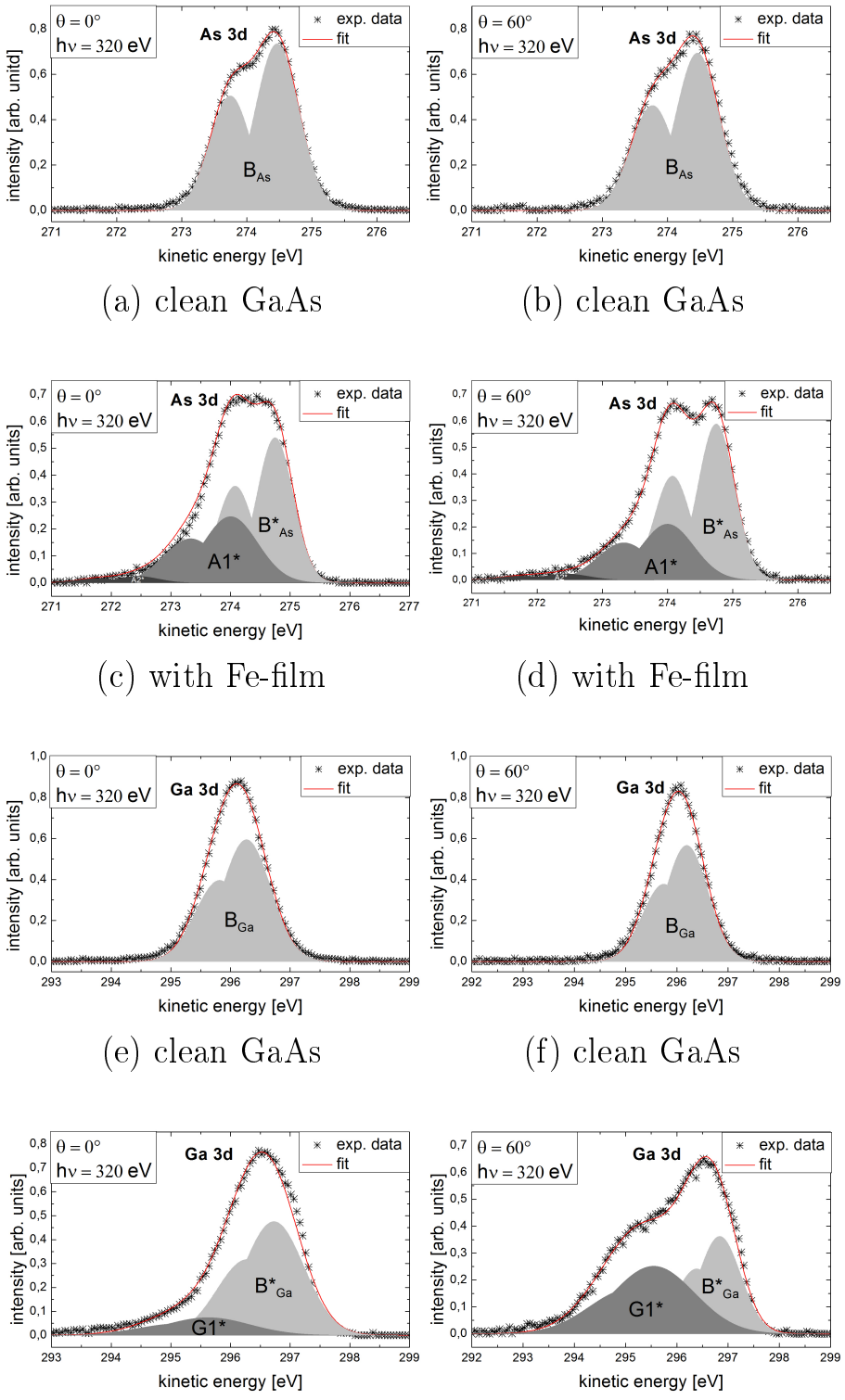

Figure 5.30: Results of a least squares fit of XPS spectra recorded before and after Fe-deposition. Left and right column display the spectra for of As 3*d* (a), (b), (c), (d) and Ga 3*d* (e), (f), (g), (h) at $\theta = 0°$ and $\theta = 60°$, respectively. The photon energy was set to $E_{\mathrm{ph}} = 320\,\mathrm{eV}$.

After Fe-deposition additional components clearly occur in both As and Ga XPS spectra. The fitting procedure resulted in three components for the As $3d$ and two components for the Ga $3d$ signal. The survey scan does not show any contamination of the Fe/GaAs(clean)-system. Hence, they can be explained by bonds of the Fe-film to the GaAs-substrate.

The three components of the As-signal may be associated to different As-Fe bonding strengths. At the interface sensitive angle of $\theta = 60°$ the As-bulk component is still strong after Fe-deposition. In contrast, the Ga-bulk component decreases strongly compared to the Fe-Ga bond component $G1^*$, which becomes dominant, see Fig 5.30 (d) and (h). This suggests the assumption of GaAs inter-diffuse into the Fe-film with a stronger As diffusion than Ga diffusion.

High-resolution spectra of the Fe $3p$ signal were recorded in order to achieve further information. However, even for long data acquisition times these spectra are rather noisy, as displayed in Fig. 5.31.

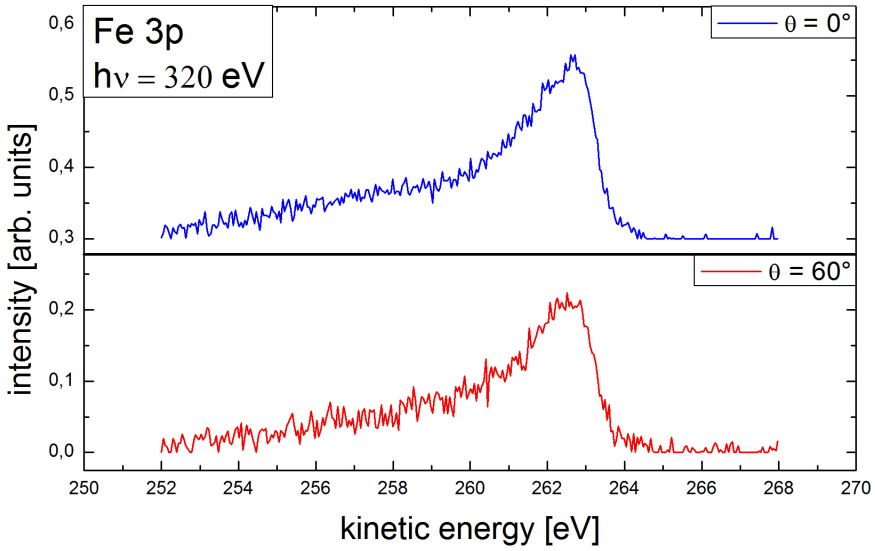

Figure 5.31: High-resolution XPS Fe $3p$ spectra of the Fe-film of the unreconstructed GaAs(001) surface at $\theta = 0°$ and $\theta = 60°$ at $h\nu = 320\,\mathrm{eV}$.

Unfortunately, a successful and non-ambiguous fitting is not possible since the data are too noisy. They can be explained by an amorphous, thin Fe-film, and a weak cross section of Fe $3p$ at $h\nu = 320\,\mathrm{eV}$. The maximum was found at around $E_{\mathrm{kin}} \approx 263\,\mathrm{eV}$, and is associated to the Fe^0-signal, which is in line with the analysis of the Fe/GaAs(4×2)-system in section 5.1.1. The shoulder at lower kinetic energies is very similar to the line shape shown in Fig. 5.4 and allows the assumption that there are further components relating to Fe-GaAs bonds.
In the following, an analysis of Fe/GaAs(clean) XPD pattern will allow to determine whether the GaAs-surface is amorphous, whether inter-diffusion occurs, and whether the Fe-film is amorphous, too.

XPD analysis

The XPD patterns of the As $3d$ and Ga $3d$ core level signals of the clean GaAs-sample are shown in Fig. 5.32. Both patterns show a twofold rotational symmetry, which can be associated to the zinc blende structure of the GaAs-crystal. Simulations based on a pure zinc blende structure are shown in Fig. 4.1, which has been performed for GaAs with a lattice constant of $a_{\mathrm{GaAs}} = 5.6\,\text{Å}$. The simulated patterns are shown in Fig. 5.32 (b) and (d) for Arsenic and Gallium, respectively. The main reflexes are caused by the monocrystalline substrate. An R-factor analysis resulted in a rather weak accordance of $R_{\mathrm{As}} = 0.23$ and $R_{\mathrm{Ga}} = 0.18$. This can be explained by the superimposed noise within the patterns due to scattering of the outgoing photoelectrons at the amorphous surface. An amorphous surface enlarges the boundary parameters to infinity within the XPD simulations, therefore no further simulations are performed. Nevertheless, the accordance between experimental and simulated pattern shows that the GaAs substrate is zinc blende structured and that no reconstructions occurs at the surface.

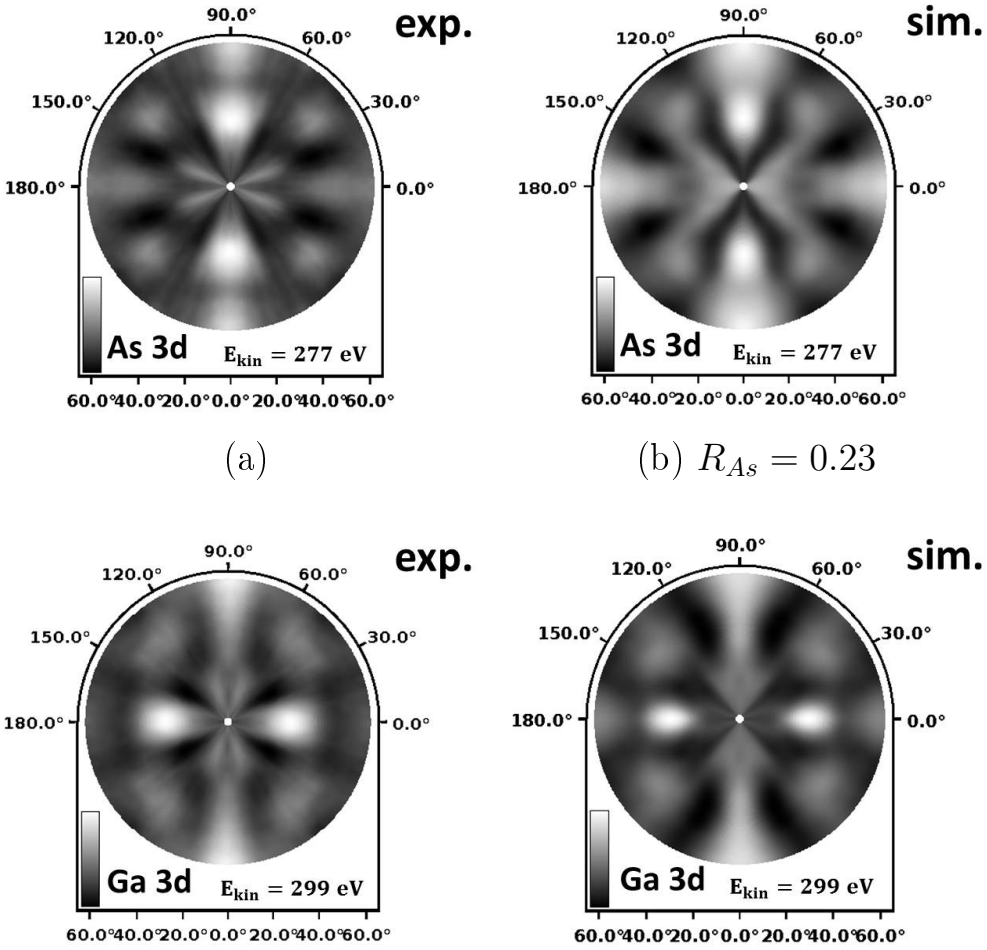

(a) (b) $R_{As} = 0.23$

(c) (d) $R_{Ga} = 0.18$

Figure 5.32: Experimental and simulated As 3*d* (a), (b), and Ga 3*d* (c), (d) XPD patterns of the unreconstructed GaAs(001)-surface.

In Fig. 5.33 the patterns of As 3*d* and Ga 3*d* signals recorded after Fe-deposition are compared to the patterns of the clean GaAs-sample. Obviously, both XPD patterns are noisy. The main reflexes of the zinc blende structure can hardly be identified. This directly illustrates an amorphous Fe/GaAs interface. Furthermore, a strong out-diffusion of GaAs into the Fe-film is confirmed here, as already discussed in the XPS spectra analysis. An indication for this finding is that within the Ga 3*d* pattern more zinc blende reflexes are displayed as in the As 3*d* pattern. Therefore, it can be assumed that the out-diffusion of Gallium is less than the out-diffusion of Arsenic.

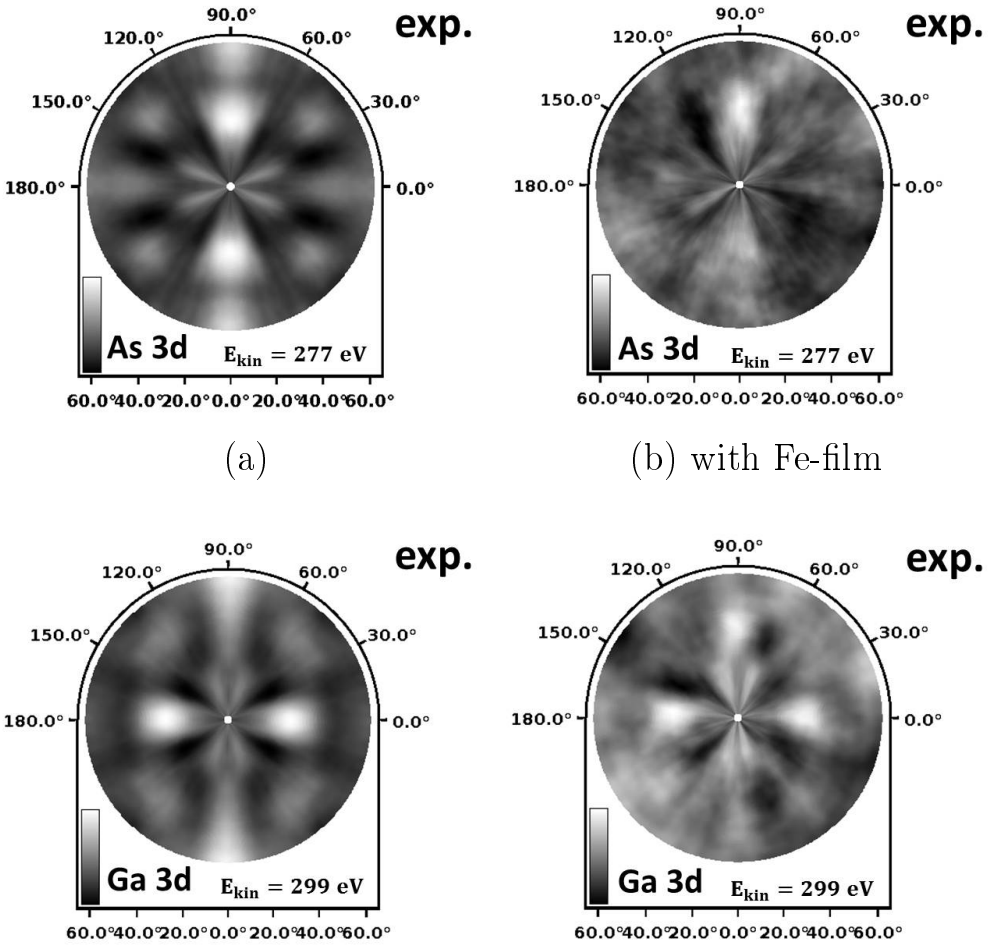

Figure 5.33: Experimental XPD patterns of As 3*d* (a), (b), and Ga 3*d* (c), (d). The patterns before and after Fe-deposition are displayed in the left and right column, respectively.

The Fe-film was investigated by an analysis of the Fe 3*p* XPD pattern, recorded at a photon energy of $E_{\mathrm{ph}} = 320\,\mathrm{eV}$. Indeed, its pattern is very noisy as can be seen in Fig. 5.34. Further, no rotational symmetry is displayed nor any crystalline structure reflexes are visible for the deposited Fe-film. This confirms the assumption of an amorphous interface and an out-diffusion of the GaAs-substrate. Furthermore, this pattern is a clear evidence that the deposited Fe-film has no short-range order crystalline properties on the unreconstructed GaAs-substrate.

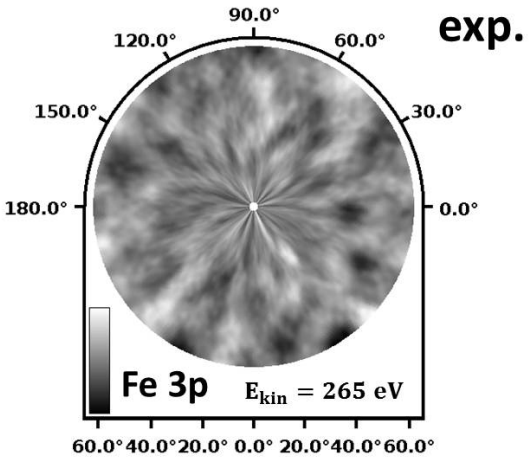

Figure 5.34: Experimental XPD pattern of the Fe 3*p* core level signal, grown on an unreconstructed GaAs(001)-surface.

An Iron film can be prepared on a clean and unreconstructed GaAs-sample. However, the analysis of XPS and XPD data confirms a non-epitaxial growth. Furthermore, Gallium and especially Arsenic strongly diffuse into the Fe-film. This can be an explanation, why both the interface and the complete Fe-film was found being amorphous. In literature, several activities propose an amorphous Fe/GaAs-interface, especially at room temperature [110–112]. Indeed, all those previous investigations used a clean and unreconstructed GaAs-surface. The XPD analysis impressively revealed an epitaxial growth, for one case only, which was found on a well reconstructed GaAs-substrate. On this surface a crystalline Fe-film and an almost perfect interface was reached for a preparation even at room temperature.
No further investigations of the Fe/GaAs(clean)-system were performed, because the Fe-interlayer is already amorphous. The epitaxial growth of a thin MgO-film as well as ferromagnetic properties requires a crystalline Fe-film.

6 Conclusion

In this thesis the Fe/GaAs and MgO/Fe interfaces of the three layer system MgO/Fe/GaAs(001) were successfully determined concerning electronic, chemical, structural, and magnetic properties. The main results for a suitable multilayer for spintronics MgO/Fe/GaAs(4 × 2) is illustrated and summarized in Fig. 6.1.

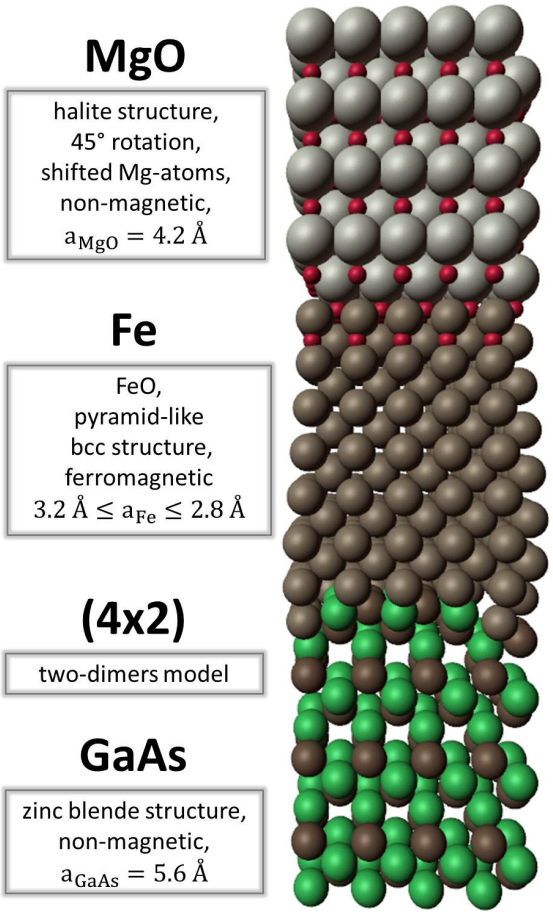

Figure 6.1: A schematic structure model of the complete MgO/Fe/GaAs(001) multilayer system. The main results of this thesis are summarized in the small boxes.

The GaAs(001) substrate crystallizes in a zinc blende structure and two different surface reconstructions were investigated during this thesis. Additionally, and for comparison, the clean and the Ga-rich (4 × 2)-reconstructed surface was analyzed. The high-resolution XPS signals of As 3*d* and Ga 3*d* reveal characteristic line shapes of both surfaces. Further, XPD patterns clearly illustrate the successful preparation and the different surface-structures.

The cleaned GaAs(001) surface showed strong reflexes of the zinc blende structure, whereas the patterns of the (4 × 2) reveal a great structural change, displayed in the As 3*d*-pattern. The two-dimers model, with two Ga-dimers being located in first and in third layer results in a lack of As-atoms at the surface, which changes the local symmetry of As from twofold to fourfold. This was observed for the XPD patterns at high kinetic energy, showing that the surface has a strong influence even on the structure in several layers beneath the surface.

An Fe-film was successfully prepared on both GaAs(001) surfaces using the identical evaporation parameters. The GaAs substrate XPS signals reveal a strong change in their line shapes displaying the dominance of chemical bonds between the Fe-film and the substrate. They are located at the interface, and they are confirmed by

Fe-As and Fe-Ga shifted signals in high-resolution Fe 3*p* spectra at two different excitation energies. The assumption of an inter-diffusion between GaAs-substrate and Fe-film was confirmed for the Fe/GaAs(clean)-system only. After Fe-deposition the As 3*d* and Ga 3*d* XPD patterns of the clean sample were noisy and the reflexes of the bulk were weakly detectable. Furthermore, the Fe 3*p* pattern displayed no symmetry indicating that the complete Fe-film is amorphous. In contrast, the As 3*d* and Ga 3*d* XPD patterns of Fe/GaAs(4 × 2)-system revealed no visible changes in comparison to the pure (4 × 2)-reconstruction. Especially, an out-diffusion of GaAs is excluded by the As 3*d* pattern, which still showed a fourfold rotational symmetry caused by the (4 × 2)-reconstruction. Furthermore, the analysis of the Fe 3*p* pattern of the Fe/GaAs(4 × 2)-system is a clear indication of a crystalline bcc structured Fe-film. Two patterns recorded at kinetic energies of $E_{\mathrm{kin}}(Fe_I) = 125\,\mathrm{eV}$ and $E_{\mathrm{kin}}(Fe_{II}) = 265\,\mathrm{eV}$ allowed a surface and interface sensitive analysis. It revealed an Fe-film being in a pyramid-like bcc structure, which can be explained by simultaneous layer and island growth of Fe on GaAs(4 × 2). The surface reconstruction of the GaAs(001) substrate prevents an out-diffusion into the Fe-film and further it promotes an epitaxial growth.

A very thin MgO-film was successfully prepared on top of the Fe/GaAs(4×2)-system. After MgO-deposition the high-resolution spectra of Fe 3*p* and Mg 2*p* displayed an additional signal, which can be associated to a bond between the Fe-interlayer and the MgO-film. The XPD pattern of Mg 2*p* and Fe 3*p* clearly illustrate the 45°-rotation between the Fe(001) and MgO(001) surfaces. MgO grew epitaxial in halite structure, with a misfit dislocation of some Mg-atoms. This is displayed by a slight shift of every second Mg-layer with regard to the Fe-surface. The oxidation of Fe due to MgO-deposition was impressively confirmed by the Fe 3*p* pattern of the Fe/MgO-system. Furthermore, it was found that oxygen mediates the bonding between Fe- and MgO. A possible misfit of MgO at the interface was investigated by the analysis of an approximately 4-monolayer thick MgO-film on Fe/GaAs(4 × 2). As a results, the misfit was confirmed and it might be the reason for an epitaxial growth of MgO on Fe up to six monolayers.

Additionally, magnetic measurements of the MgO/Fe/GaAs(4 × 2) multilayer system revealed its magnetic properties. An Mg 2*p* signal was not detectable within the T-MOKE spectra displaying no ferromagnetic properties of the MgO-film nor an induced magnetization by the misfit. Despite all structural and chemical changes of the Fe-interlayer, like its pyramid-structure and its oxidized surface, it showed a strong reaction on the external magnetic field during the measurements. Further

hysteresis measurements of the Fe $3p$ signal demonstrated impressively the ferromagnetic properties of the Fe-interlayer.
The material requirements on a TMR/GMR junction are provided by the MgO/Fe/GaAs(4×2) multilayer. The interfaces were well ordered and every single layer was crystalline. The MgO-film and the GaAs-substrate showed no magnetic properties, whereas the Fe-interlayer retained excellent ferromagnetism. This indicated that the MgO/Fe/GaAs(4×2) is an perspective system for spintronics devices.

7 Outlook

In order to complete a TMR-junction a fourth layer of Iron on the MgO/Fe/GaAs(001) multilayer system could be prepared. The Fe/MgO-interface may show the same characteristics as the MgO/Fe-interface. Certainly, this could be verified by further XPS and XPD investigations. In this thesis, it was shown that the interfacial Oxygen atom serves as the bonding between MgO and Fe, therefore an oxidation of the topmost layer becomes possible. At present it is an open question, whether the lattice misfit found for the MgO-film will suppress an epitaxial growth of the proposed fourth layer.

In this thesis, all preparation steps were performed at room temperature. A weak heating of the Fe/GaAs(4×2)-system during MgO evaporation could prevent an oxidation of the Fe-surface. Certainly, elevated temperature promotes an interdiffusion between GaAs and Fe due to different sublimations points. Since the temperatures were measured by a pyrometer, we estimate the uncertainty in temperature of around $\Delta T = \pm 10°\mathrm{C}$. During elevated temperatures a small As-flux was observed at $T \approx 350\,°\mathrm{C}$, hence knowing the precise GaAs-temperature is indispensable.

In this thesis the chemical, structural, and magnetic properties of MgO/Fe/GaAs(4×2) were determined. Certainly, further measurements, like spin-resolved spectroscopy would reveal further information on the magnetic properties of the system. Conclusively, the efficiency of the TMR and GMR effects of the MgO/Fe/GaAs(4×2)-system could be verified.

Finally, Fe could be substituted by Cobalt (Co), which is known having similar magnetic properties as Iron, but it crystallizes in a hexagonal lattice. Thus, it would be interesting to grow epitaxial Co on GaAs, and being covered by an crystalline MgO capping layer. Maybe the hexagonal structure of Co prevents a lattice misfit of the MgO-film. The magnetic properties of Co beneath MgO may be investigated in order to verify if Co could be an alternative to Fe in the MgO/Fe/GaAs(001) spintronics system.

A Appendix

During this thesis the Gaussian influence of the experimental equipment was observed to dominate the recorded XPS spectra. A verification of the use of a Gaussian function instead of the Voigt-profile was already given by Dreiner [113] and during a Bachelor thesis [114]. Below, a demonstration of the Gaussian influence even on a metal XPS peak will be given for the Fe $3p$ signal exemplarily.

A.1 Analysis of Fe $3p$-signal using an asymmetric line shape

A XPS core level signal of a conductive sample like metals show an asymmetric line shape, as mentioned in chapter 2.1.2. In this thesis, the signal of the metal Iron was analyzed by a Gaussian fit procedure due to the Gaussian dominance and achieving comparable results. In order to examine these assumptions an analysis of the Fe $3p$-signal using an asymmetric function was performed. In this section the results of two fitting procedures are compared.

The fits of the Fe $3p$ XPS core level are performed by a Gaussian function[2]

$$G(E_\mu) = A_\mu \cdot \exp\left(\frac{1}{2}\left[\frac{E - E_\mu}{\sigma_\mu}\right]^2\right) \tag{A.1}$$

and a function including an asymmetric line shape[3]

$$A(E_\eta) = A_\eta \cdot \exp\left(\exp\left[-\frac{E - E_\eta}{\sigma_\eta}\right] - \frac{E - E_\eta}{\sigma_\eta} + 1\right) . \tag{A.2}$$

Thereby, the binding energies were used as the parameters E_μ, and E_η, because then the asymmetric function was the most stable during the fitting procedures. The parameter A denotes the amplitude and σ the FWHM of the respective function. According to the analysis discussed in section 5 the spin-orbit coupling and the chemical shift within each peak have to be minded by various numbers of function terms. The results of the fitting procedure using the Gaussian (A.1) and the asymmetric function (A.2) are illustrated in Fig. A.1.

[2] Origin function name *GaussAmp*
[3] Origin function name *Extreme*

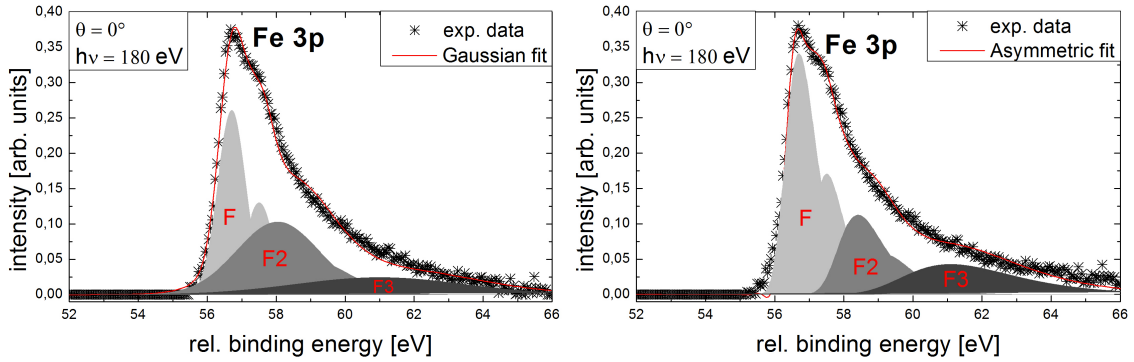

(a) Gaussian fit (b) Asymmetric fit

Figure A.1: In comparison for $\theta = 0°$, the Gaussian (a) and asymmetric (b) fitted Fe $3p$ high-resolution XPS signals. The photon energy was set to $E_{\mathrm{ph}} = 180\,\mathrm{eV}$.

The most relevant information about the sample-system getting from the XPS high-resolution spectra are the binding energies of the individual components and the relative intensity relations between them. Therefore, these parameters are compared for the two fit-functions in Tab. A.1.

fit-function	component	rel. binding energy [eV]	rel. intensity
Gauß-Fit	F	56.68	1
	F2	58.04	$\approx F/3$
	F3	61.10	$\approx F/9$
Asymmetry-Fit	F	56.67	1
	F2	58.03	$\approx F/3$
	F3	61.08	$\approx F/10$

Table A.1: Comparison of the fitting parameters of the Gauß and the Asymmetry function.

As can be seen, the numbers of components, the energy positions, as well as the intensity relations are similar. The spectra and the fitting parameters reveal differences in the experimental and numerical uncertainty. Furthermore, Fig. A.1 reveals a better accordance between experimental data and Gaussian fit-function. The asymmetric line shape differs clearly from the experimental data in lower energy range. Especially the overshoot around $E_{\mathrm{kin}} \approx 56\,\mathrm{eV}$ could not be eliminated during

the fitting procedure.
It can be inferred, that the Gaussian influence of the used experimental set-up dominates even a signal of a metal like Iron. The use of a Gaussian fit-function to get the chemical end electronic information about the sample do not neglect important parameters of the analysis discussed in this thesis.

Bibliography

[1] S.-H. Yang, B. Balke, C. Papp, S. Döring, U. Berges, L. Plucinski, C. Westphal, C.M. Schneider, S.S.P. Parkin, and C.S. Fadley. Determination of layer-resolved composition, magnetization, and electronic structure of an Fe/MgO tunnel junction by standing-wave core and valence photoemission. *Phys. Rev. B*, **84**:184410, 2011.

[2] G. Autès, J. Mathon, and A. Umerski. Theory of tunneling magnetoresistance of Fe/GaAs/Fe(001) junctions. *Phys. Rev. B*, **82**:115212, 2010.

[3] B. Kardasz, E.A. Montoya, C. Eyrich, E. Girt, and B. Heinrich. Spin dynamics and magnetic anisotropies at the Fe/GaAs(001) interface. *Journal of Applied Physics*, **109**(07D337):3, 2011.

[4] M.S. Xue, W. Li, F.J. Wang, J.P. Yao, and J.S. Lu. Interfacial interaction in Fe/MgO/Fe magnetic tunneling junctions. *Vacuum*, **85**(4), 2010.

[5] G.A. Prinz. Magnetoelectronics applications. *Journal of Magnetism and Magnetic Materials*, **200**(1-3):57 – 68, 1999.

[6] M. Jullière. Tunneling between ferromagnetic films. *Physics Letters A*, **54**(3):225 – 226, 1975.

[7] G. Binasch, P. Grünberg, F. Saurenbach, and W. Zinn. Enhanced magnetoresistance in layered magnetic structures with antiferromagnetic interlayer exchange. *Phys. Rev. B*, **39**:4828–4830, 1989.

[8] M.N. Baibich, J.M. Broto, A. Fert, F. Nguyen Van Dau, F. Petroff, P. Etienne, G. Creuzet, A. Friederich, and J. Chazelas. Giant magnetoresistance of (001)Fe/(001)Cr magnetic superlattices. *Phys. Rev. Lett.*, **61**:2472–2475, 1988.

[9] S. Datta and B. Das. Electronic analog of the electro-optic modulator. *Appl. Phys. Lett.*, **56**(665), 1990.

[10] D. Hägele, M. Oestreich, W.W. Rühle, N. Nestle, and K. Eberl. Spin transport in GaAs. *Appl. Phys. Letters*, **73**(1580):3, 1998.

[11] L.-N. Tong, F. Matthes, M. Müller, C.M. Schneider, and C.-G. Lee. Influence of MgO overlayers on the electronic states of Fe(001) thin films grown on GaAs(001). *Phys. Rev. B*, 77:064421, 2008.

[12] S. Tehrani, J.M. Slaughter, M. Deherrera, B.N. Engel, N.D. Rizzo, J. Salter, M. Durlam, R.W. Dave, J. Janesky, B. Butcher, K. Smith, and G. Grynkewich. Magnetoresistive random access memory using magnetic tunnel junctions. *Proceedings of the IEEE*, **91**(5):703 – 714, 2003.

[13] V.E. Henrich and P.A. Cox. *The Surface Science of Metal Oxides*. Cambridge University Press, Cambridge, 1999.

[14] J.S. Moodera, Lisa R. Kinder, Terrilyn M. Wong, and R. Meservey. Large magnetoresistance at room temperature in ferromagnetic thin film tunnel junctions. *Phys. Rev. Lett.*, **74**:3273–3276, 1995.

[15] W.H. Butler, X.-G. Zhang, T.C. Schulthess, and J.M. MacLaren. Spin-dependent tunneling conductance of Fe/MgO/Fe sandwiches. *Phys. Rev. B*, **63**:054416, 2001.

[16] S.S.P. Parkin, C. Kaiser, A. Panchula, P.M. Rice, B. Hughes, M. Samant, and S. Yang. Giant tunnelling magnetoresistance at room temperature with MgO(100) tunnel barriers. *Nature Materials*, **3**:862 – 867, 2004.

[17] J. Mathon and A. Umerski. Theory of tunneling magnetoresistance of an epitaxial Fe/MgO/Fe(001) junction. *Phys. Rev. B*, **63**:220403, 2001.

[18] G.X. Miao, J.Y. Chang, M.J. van Veenhuizen, K. Thiel, M. Seibt, G. Eilers, M. Münzberg, and J.S. Moodera. Epitaxial growth of MgO and Fe/MgO magnetic tunnel junctions on (100)-Si by molecular beam epitaxy. *Appl. Phys. Lett.*, **93**:142511, 2008.

[19] P. Torelli, M. Sperl, R. Ciancio, J. Fujii, C. Rinaldi, M. Cantoni, R. Bertacco, M. Utz, M. Soda, E. Carlino, G. Rossi, C.H. Back, and G. Panaccione. Growth of ultrathin epitaxial Fe/MgO spin injector on (0,0,1) (Ga, Mn)As. *Nanotechnology*, **23**:465202, 2012.

[20] H.J. Zhu, M. Ramsteiner, H. Kostial, M. Wassermeier, H.-P. Schönherr, and K.H. Ploog. Room-temperature spin injection from Fe into GaAs. *Phys. Rev. Lett.*, **87**:016601, 2001.

[21] P.R. Hammar, B.R. Bennett, M.J. Yang, and M. Johnson. Observation of spin injection at a ferromagnet-semiconductor interface. *Phys. Rev. Lett.*, **83**:203–206, 1999.

[22] H.J. Zhu, M. Ramsteiner, H. Kostial, M. Wassermeier, H.-P. Schönherr, and K. H. Ploog. Room-temperature spin injection from Fe into GaAs. *Phys. Rev. Lett.*, **87**:016601, 2001.

[23] E.I. Rashba. Theory of electrical spin injection: Tunnel contacts as a solution of the conductivity mismatch problem. *Phys. Rev. B*, **62**:R16267–R16270, 2000.

[24] G.X. Du, S.G. Wang, Q.L. Ma, Y. Wang, R.C.C. Ward, X.-G. Zhang, C. Wang, A. Kohn, and X.F. Han. Spin-dependent tunneling spectroscopy for interface characterization of epitaxial Fe/MgO/Fe magnetic tunnel junctions. *Phys. Rev. B*, **81**:064438, 2010.

[25] F. Bonell, S. Andrieu, A.M. Bataille, C. Tiusan, and G. Lengaigne. Consequences of interfacial Fe-O bonding and disorder in epitaxial Fe/MgO/Fe(001) magnetic tunnel junctions. *Phys. Rev. B*, **79**:224405, 2009.

[26] Y.B. Xu, E.T.M. Kernohan, D.J. Freeland, A. Ercole, M. Tselepi, and J.A.C. Bland. Evolution of the ferromagnetic phase of ultrathin Fe films grown on GaAs(100)-4 $\times$ 6. *Phys. Rev. B*, **58**(2):890–896, 1998.

[27] H. Hertz. Über den Einfluss des ultravioletten Lichtes auf die electrische Entladung. *Annalen der Physik*, **31**(983), 1887.

[28] W. Hallwachs. Über den Einfluss des Lichtes auf electrostatisch geladene Körper. *Annalen der Physik und Chemie*, **269**(2), 1888.

[29] W. Hallwachs. Über die Electrisierung von Metallplatten durch Bestrahlung mit electrischem Licht. *Annalen der Physik und Chemie*, **270**(8A), 1888.

[30] A. Einstein. Über einen die Erzeugung und Verwandlung des Lichtes betreffenden heuristischen Gesichtspunkt. *Annalen der Physik*, **17**:S. 132–148, 1905.

[31] M. Henzler and W. Göpel. *Oberflächenphysik des Festkörpers*. Teubner Studienbücher, Stuttgart, tenth edition, 1991.

[32] S. Hüfner. *Phototelectron spectroscopy, principles and applications*. Springer, Berlin, second edition, 1996.

[33] P. Auger. Sur les rayons β secondaires produits dans un gaz par des rayons X. *Comptes Rendus, Académie des sciences*, **180**, 1925.

[34] L. Meitner. Über die β-Strahl-Spektra und ihren Zusammenhang mit der γ-Strahlung. *Zeitschrift für Physik*, **11**, 1922.

[35] M.P. Seah. An accurate and simple universal curve for the energy-dependent electron inelastic mean free path. *Surface and interface analysis*, **44**:47–503, 2012.

[36] J.H. Lambert. *Photometria, sive de mensura et gradibus luminis colorum et umbrae.* Sumptibus Vidae Eberhardi Klett, Augsburg, 1760.

[37] A. Beer. Bestimmung der Absorption des rothen Lichts in farbigen Flüssigkeiten. *Annalen der Physik und Chemie*, **86**:78–88, 1852.

[38] J.F. Watts and J. Wolstenholme. *An introduction to surface analysis by XPS and AES.* John Wiley and Sons Ltd., Chichester, 2010.

[39] D. Briggs and M.P. Seah. *Practical Surface Analysis, Vol.1.* John Wiley and Sons Ltd., Chichester, 1990.

[40] J.J. Yeh and I. Lindau. Atomic subshell photoionization cross sections and asymmetry parameters $1 \leq Z \leq 103$. *Atomic Data and Nuclear Data Tables*, **32**:1–155, 1985.

[41] C.D. Wagner, W.M. Riggs, L.E. Davis, and J.F. Moulder. *Handbook of x-ray photoelectron spectroscopy.* Perkin-Elmer Co., Eden Prairie, 1978.

[42] F. Schwabl. *Quantenmechanik QM I.* Springer, Berlin Heidelberg, seventh edition, 2007.

[43] U. Gelius, P.F. Hedén, J. Hedman, B.J. Lindberg, R. Manne, R. Nordberg, C. Nordling, and K. Siegbahn. Molecular spectroscopy by means of ESCA. *Physica Scripta*, **2**(70-80), 1970.

[44] K. Siegbahn. Electron spectroscopy for atoms, molecules, and condensed matter. *Nobel lecture*, 1981.

[45] R.F. Bunshah. *Handbook of deposition technologies for thin films and coatings.* Noyes publications, Park Ridge, New Jersey, second edition, 1994.

[46] D.A. Shirley. High-resolution x-ray photoemission spectrum of the valence bands of gold. *Phys. Rev. B*, **5**:4709–4714, 1972.

[47] OriginLab Cooperation. Northampton, MA; http://www.originlab.de.

[48] A. Siegbahn, U. Gelius, H. Siegbahn, and E. Olson. Angular distribution of electrons in ESCA spectra from a single crystal. *Physica Scripta*, **1**(272), 1970.

[49] A. Liebsch. Theory of angular resolved photoemission from adsorbates. *Phys. Rev. Lett.*, **32**:1203–1206, 1974.

[50] M.-L. Xu, J.J. Barton, and M.A. Van Hove. Electron scattering by atomic chains: Multiple-scattering effects. *Phys. Rev. B*, **39**:8275–8283, 1989.

[51] T. Lühr. private communication, 2014.

[52] R. Gunnella, F. Solal, D. Sébilleau, and C.R. Natoli. MSPHD: A full multiple scattering code for low energy photoelectron diffraction. *Computer Physics Communications*, **132**(3):251 – 266, 2000.

[53] R. Gunnella, M. Shimomura, F. D'Amico, T. Abukawa, and S. Kono. Photoelectron diffraction of $C_6H_8/Si(001)$: A model case for photoemission study of organic molecules adsorbed on silicon surfaces. *Phys. Rev. B*, **73**:235435, 2006.

[54] C.R. Natoli, M. Benfatto, C. Brouder, M.F. Ruiz López, and D.L. Foulis. Multichannel multiple-scattering theory with general potentials. *Phys. Rev. B*, **42**:1944–1968, 1990.

[55] D. Sébilleau, R. Gunnella, Z.-Y. Wu, S. Di Matteo, and C.R. Natoli. Multiple-scattering approach with complex potential in the interpretation of electron and photon spectroscopies. *J. Phys.: Condens. Matter*, **18**:R175–R230, 2006.

[56] F. Da Pieve, D. Sébilleau, S. Di Matteo, R. Gunnella, R. Gotter, A. Ruocco, G. Stefani, and C.R. Natoli. Multiple scattering approach for two-electron resonant emission studied by angle-resolved coincidence spectroscopy. *Phys. Rev. B*, **78**:035122, 2008.

[57] D.P. Woodruff and A.M. Bradshaw. Adsorbate structure determination on surfaces using photoelectron diffraction. *Rep. Prog. Phys.*, **57**:1029–1080, 1994.

[58] T. Lühr. *Messung und Simulation von XPD-Mustern der Si(110)/SiO_2-Grenzschicht.* Diploma thesis, Technische Universität Dortmund, 2009.

[59] D. Handschak, T. Lühr, F. Schönbohm, S. Döring, C. Keutner, U. Berges, and C. Westphal. Structural investigation of the three-layer system MgO/Fe/GaAs(001) by means of photoelectron spectroscopy and diffraction. *Phys. Rev. B*, **88**:045313, 2013.

[60] R. Döll and M.A. Van Hove. Global optimization in LEED structure determination using genetic algorithms. *Surface Science*, **355**:L393 – L398, 1996.

[61] L. Bergmann and C. Schaefer. *Lehrbuch der Experimentalphysik Band 6 - Festkörper*. de Gruyter, Berlin, second edition, 2005.

[62] J. Kerr. *Rep. Brit. Ass. Adv. Sci.*, **40**(18), 1876.

[63] S.D. Bader. SMOKE. *Journal of Magnetism and Magnetic Materials*, **100**:440–454, 1991.

[64] M.F. Tesch. private communication, 2014.

[65] M.F. Tesch. *Magneto-optische Reflexionsspektroskopie mittels linear polarisierter Synchrotronstrahlung an dünnen einkristallinen Fe-, Co- und Ni-Schichten*. Dissertation, Universität Duisburg-Essen, 2014.

[66] J. Stöhr and H.C. Siegmann. *Magnetism*. Springer Series in Solid State Science, Berlin Heideberg, 2006.

[67] M.F. Tesch, M.C. Gilbert, H.-Ch. Mertins, D.E. Bürgler, U. Berges, and C M. Schneider. X-ray magneto-optical polarization spectroscopy: an analysis from the visible region to the x-ray regime. *Applied Optics*, **52**(18):4294–4310, 2013.

[68] D. Handschak, M.F. Tesch, F. Schönbohm, T. Lühr, C. Keutner, U. Berges, H.-Ch. Mertins, and C. Westphal. Structure and magnetic characterization of the interfacial regimes of MgO/Fe/GaAs(001). *submitted*, 2014.

[69] H.-Ch. Mertins, D. Abramsohn, A. Gaupp, F. Schäfers, W. Gudat, O. Zaharko, H. Grimmer, and P. M. Oppeneer. Resonant magnetic reflection coefficients at the Fe 2p edge obtained with linearly and circularly polarized soft x-rays. *Phys. Rev. B*, **66**:184404, 2002.

[70] M. Gilbert, H.-Ch. Mertins, M. Tesch, O. Berges, Herbert Feilbach, and C.M. Schneider. TetraMag: A compact magnetizing device based on eight rotating permanent magnets. *Review of Scientific Instruments*, **83**(2), 2012.

[71] C. Davisson and L.H. Germer. Diffraction of electrons by a crystal of Nickel. *Phys. Rev.*, **30**:705–740, 1927.

[72] G. Ertl and J. Küppers. *Low energy electrons and surface chemistry.* Wiley-VCH, Weinheim, 1974.

[73] W. Mönch. *Semiconductor Surfaces and Interfaces.* Springer Series in Surface Science, Berlin Heidelberg, third edition, 2001.

[74] Q.-K. Xue, T. Hashizume, and T. Sakurai. Scanning tunneling microscopy of III-V compound semiconductor (001) surfaces. *Progress in Surface Science*, **56**(1-2):1 – 131, 1997.

[75] E.A. Wood. Vocabulary of surface crystallography. *J. Appl. Phys.*, **35**:1306, 1964.

[76] R. Moosbühler, F. Bensch, M. Dumm, and G. Bayreuther. Epitaxial Fe films on GaAs(001): Does the substrate surface reconstruction affect the unaxial magnetic anisotropy? *J. Appl. Phys.*, **91**(8757):3, 2002.

[77] J.-M. Lee, S.-J. Oh, K.J. Kim, S.-U. Yang, J.-H. Kim, and J.-S. Kim. Kinetic stabilization of a pristine Fe film on (4×2)-GaAs(100). *Phys. Rev. B*, **75**:125421, 2007.

[78] E.M. Kneedler, B.T. Jonker, P.M. Thibado, R.J. Wagner, B.V. Shanabrook, and L.J. Whitman. Influence of substrate surface reconstruction on the growth and magnetic properties of Fe on GaAs(001). *Phys. Rev. B*, **56**:8163–8168, 1997.

[79] S.C. Erwin, S.-H. Lee, and M. Scheffler. First-principles study of nucleation, growth, and interface structure of Fe/GaAs. *Phys. Rev. B*, **65**:205422, 2002.

[80] D. Handschak. *Untersuchung der Dreischichtsystems MgO/Fe/GaAs(001) mittels Photoelektronenspektroskopie und Photoelektronenbeugung.* Diploma thesis, Technische Universität Dortmund, 2011.

[81] M. Doi, B.C. Roldan, W. Keune, T. Schmitte, A. Nefedov, H. Zabel, D. Spoddig, R. Meckenstock, and J. Pelzl. Magnetic and structural properties of epitaxial Fe thin films on GaAs(001) and interfaces. *Journal of Magnetism and Magnetic Materials*, **240**(1-3):407 – 409, 2002.

[82] M. Müller. *Electronic structure of Ferromagnet-Insulator Interfaces: Fe/MgO and Co/MgO*. Dissertation, Universität Duisburg-Essen, 2007.

[83] M. Larive, G. Jezequel, J.P. Landesman, F. Solal, J. Nagle, B. Lèpine, A. Taleb-Ibrahimi, G. Indlekofer, and X. Marcadet. Photoelectron spectroscopy study of Ga 3d and As 3d core levels on MBE-grown GaAs surfaces. *Surface Science*, **304**(3):298 – 308, 1994.

[84] A. Lebugle, U. Axelsson, R. Nyholm, and N. Mårtensson. Experimental L and M core level binding energies for the metals ^{22}Ti to ^{30}Zn. *Physica Scripta*, **23**(825), 1980.

[85] V. Di Castro, G. Polzonetti, S. Ciampi, G. Contini, and O. Sakho. Photoemission study of the Fe/MnO interface formation. *Surface Science*, **293**(1-2):41 – 46, 1993.

[86] F. Parmigiani and L. Sangaletti. Fine structures in the x-ray photoemission spectra of MnO, FeO, CoO, and NiO single crystals. *Journal of Electron Spectroscopy and Related Phenomena*, **98-99**(0):287 – 302, 1999.

[87] B. Handke, J.B. Simonsen, M. Bech, Z. Li, and P.J. Mller. Iron oxide thin film growth on Al_2O_3/NiAl(110). *Surface Science*, **600**(24):5123 – 5130, 2006.

[88] S. Hilpert and T. Dieckmann. Über Arsenide. I. (Eisen- und Manganarsenide). *Berichte der deutschen chemischen Gesellschaft*, **44**:2378–2385, 1911.

[89] B. Predel and W. Vogelbein. Thermodynamische Untersuchung der Systeme Eisen-Gallium und Kobalt-Gallium. *Thermochimica Acta*, **13**(2):133 – 145, 1975.

[90] S.A. Chambers, F. Xu, H.W. Chen, I.M. Vitomirov, S.B. Anderson, and J.H. Weaver. Simultaneous epitaxy and substrate out-diffusion at a metal-semiconductor interface: Fe/GaAs(001)-c(8×2). *Phys. Rev. B*, **34**(10):6605–6611, 1986.

[91] M.W. Ruckman, J.J. Joyce, and J.H. Weaver. Interdiffusion and reaction at the Fe/GaAs(110) interface. *Phys. Rev. B*, **33**:7029–7035, 1986.

[92] D.K. Biegelsen, R.D. Bringans, J.E. Northrup, and L.-E. Swartz. Surface reconstructions of GaAs(100) observed by scanning tunneling microscopy. *Phys. Rev. B*, **41**:5701–5706, 1990.

[93] K. Kalki, D.D. Chambliss, K.E. Johnson, R.J. Wilson, and S. Chiang. Evidence for martensitic fcc-bcc transition of thin Fe films on Cu(100). *Phys. Rev. B*, **48**:18344–18347, 1993.

[94] S.A. Chambers and V.A. Loebs. Elastic strain at pseudomorphic semiconductor heterojunctions studied by x-ray photoelectron diffraction: Ge/Si(001) and Si/Ge(001). *Phys. Rev. B*, **42**:5109–5116, 1990.

[95] M. Gester, C. Daboo, S.J. Gray, and J.A.C. Bland. Formation of pyramid-like structures in the growth of epitaxial Fe / GaAs(001) structures. *Journal of Magnetism and Magnetic Materials*, **165**, 1997.

[96] A. Winkelmann, C.S. Fadley, and F.J. Garcia de Abajo. High-energy photoelectron diffraction: model calculations and future possibilities. *New Journal of Physics*, **10**(11):113002, 2008.

[97] P.M.Th.M. Van Attekum and J.M. Trooster. The resolution obtainable in x-ray photoelectron spectroscopy with unmonochromatized Mg Kα radiation. *Journal of Electron Spectroscopy and Related Phenomena*, **18**(1):135 – 143, 1980.

[98] H.L. Meyerheim, R. Popescu, J. Kirschner, N. Jedrecy, M. Sauvage-Simkin, B. Heinrich, and R. Pinchaux. Geometrical and compositional structure at metal-oxide interfaces: MgO on Fe(001). *Phys. Rev. Lett.*, **87**:076102, 2001.

[99] B.D. Yu and J.-S. Kim. Ab initio study of ultrathin MgO films on Fe(001): Influence of interfacial structures. *Phys. Rev. B*, **73**(12):125408, 2006.

[100] T. Kanaji, K. Asano, and S. Nagata. Behaviour of impurity atoms and adsorbed oxygen atoms on (001) face of iron epitaxial film. *Vacuum*, **23**(2):55 – 59, 1973.

[101] J.L. Vassent, M. Dynna, A. Marty, B. Gilles, and G. Patrat. A study of growth and the relaxation of elastic strain in MgO on Fe(001). *J. Appl. Phys.*, **80**(5727):9, 1996.

[102] H.L. Meyerheim, R. Popescu, N. Jedrecy, M. Vedpathak, M. Sauvage-Simkin, R. Pinchaux, B. Heinrich, and J. Kirschner. Surface X-ray diffraction analysis of the MgO/Fe(001) interface: Evidence for an FeO layer. *Phys. Rev. B*, **65**(144433), 2002.

[103] M. Dynna, J.L. Vassent, A. Marty, and B. Gilles. A lowenergy electron diffraction investigation of the surface deformation induced by misfit dislocations in thin MgO films grown on Fe(001). *J. Appl. Phy.*, **80**:2650, 1996.

[104] A. Tekiel, S. Foster, J.Topple, Y. Miyahara, and P. Grütter. Reactive growth of MgO overlayers on Fe(001) surfaces studied by low-energy electron diffraction and atomic force microscopy. *Applied Surface Science*, **273**(0):247 – 252, 2013.

[105] M. Klaua, D. Ullmann, J. Barthel, W. Wulfhekel, J. Kirschner, R. Urban, T.L. Monchesky, A. Enders, J.F. Cochran, and B. Heinrich. Growth, structure, electronic, and magnetic properties of MgO/Fe(001) bilayers and Fe/MgO/Fe(001) trilayers. *Phys. Rev. B*, **64**:134411, 2001.

[106] F. Nolting, D. Legut, J. Rusz, P.M. Oppeneer, G. Woltersdorf, and C.H. Back. Anisotropy of the $L_{2,3}$ x-ray magnetic linear dichroism of Fe films on GaAs: Experiment and ab initio theory. *Phys. Rev. B*, **82**, 2010.

[107] J. Nogués and I.K. Schuller. Exchange bias. *Journal of Magnetism and Magnetic Materials*, **192**:203 – 232, 1999.

[108] C.-H. Lambert, A. Rajanikanth, T. Hauet, S. Mangin, E.E. Fullerton, and S. Andrieu. Quantifying perpendicular magnetic anisotropy at the Fe-MgO(001) interface. *Applied Physics Letters*, **102**(12), 2013.

[109] G. Le Lay, D. Mao, A. Kahn, Y. Hwu, and G. Margaritondo. High-resolution synchrotron-radiation core-level spectroscopy of decapped GaAs(100) surfaces. *Phys. Rev. B*, **43**:14301–14304, 1991.

[110] G. Wedler, B. Wassermann, R. Nötzel, and R. Koch. Stress evolution during Fe(001) epitaxy on GaAs(001). *Applied Physics Letters*, **78**(9), 2001.

[111] J.D.W. Thompson, J.R. Neal, T.H. Shen, S.A. Morton, J.G. Tobin, G. Dan Waddill, J.A.D. Matthew, D. Greig, and M. Hopkins. The evolution of Ga and As core levels in the formation of Fe/GaAs(001): A high resolution soft x-ray photoelectron spectroscopy study. *J. Appl. Phys.*, **104**, 2008.

[112] T. Ashraf, C. Gusenbauer, J. Stangl, G. Hesser, M. Wegscheider, and R. Koch. Stress and interdiffusion during molecular beam epitaxy of Fe on As-rich GaAs(001). *J. Phys.: Condens. Matter*, **23**, 2011.

[113] S. Dreiner. *Untersuchung von Ober- und Grenzflächen mittels niederenergetischer Photoelektronenbeugung.* Dissertation, Westfälische Wilhelms-Universität Münster, 2002.

[114] C. Kohlmann. *Gauß Verbreiterung von XPS-Signalen.* Bachelor thesis, Technische Universität Dortmund, 2014.

[115] N.W. Ashcroft and D.N. Mermin. *Festkörperphysik.* Oldenbourg, München, 2007.

[116] D. C. Weier. *Interface investigation between hydrocarbon and hydrocarbon-like molecules on semiconductor surfaces.* Dissertation, Technische Universität Dortmund, 2010.

[117] F. Schönbohm. *Temperaturverhalten und Strukturbestimmung dünner Metalloxidschichten auf Siliziumoberflächen.* Dissertation, Technische Universität Dortmund, 2013.

[118] P.H. Kopitzki. *Einführung in die Festkörperphysik.* Teubner Studienbücher, Wiesbaden, sixth edition, 2007.

[119] C. Westphal. The study of local atomic structure by means of x-ray photoelectron diffraction. *Surface Science Reports*, **50**(1-3):1–106, 2003.

[120] F.R. Negreiros, E.A. Soares, A. de Siervo, R. Paniago, V.E. de Carvalho, and R. Landers. Theoretical study of the heteroepitaxial growth of Pd on Cu(111), Pd on Ni(111), Ni on Pd(111), and Cu on Pd(111) using a semiempirical method. *Phys. Rev. B*, **81**:085437, 2010.

[121] A. De Siervo, E.A. Soares, R. Landers, and G.G. Kleiman. Photoelectron diffraction studies of Cu on Pd(111) random surface alloys. *Phys. Rev. B*, **71**:115417, 2005.

[122] C.E. Mortimer and U. Müller. *Chemie.* Thieme Verlag, Stuttgart, 2003.

[123] D.J. O'Connor, B.A. Sexton, and R.St.C. Smart (Eds.). *Surface Analysis Methods in Material Science.* Springer, Berlin, second edition, 2003.

[124] L.B. Freud and S. Suresh. *Thin film materials.* University Press, Cambridge, 2003.

Parts of this work have been published in:

D. Handschak, T. Lühr, F. Schönbohm, S. Döring, C. Keutner, U.Berges, and C. Westphal (**2013**)
Structural investigation of the three-layer system MgO/Fe/GaAs(001) by means of photoelectron spectroscopy and diffraction. *Phys. Rev. B*, **88**:045313

D. Handschak, F. Schönbohm, T.Lühr, C. Keutner, U. Berges, and C. Westphal (**2013**)
Investigation of the MgO adsorbate and the MgO/Fe interface on a Fe/GaAs(001) substrate by means of XPS and XPD. *NSTI-Nanotech*, **Vol.1**, pp.105-108, www.nsti.org, ISBN:978-1-4822-0581-7

D. Handschak, M.F. Tesch, F. Schönbohm, T. Lühr, C. Keutner, U. Berges, H.-Ch. Mertins, and C. Westphal (**2014**)
Structure and magnetic characterization of the interfacial regimes of MgO/Fe/GaAs(001). *submitted*

Further publications

L.H. de Lima, D. Handschak, F. Schönbohm, R. Landers, C. Westphal and A. de Siervo (**2014**)
Atomic structure of bare buffer layer on SiC(0001) chemically resolved. *Chem. Commun.*, **50**(88), 13571-13574

International conference contributions:

TechConnect World and National Innovation Summit - Nanotech Washington D.C. USA, May 2013
Speech on: Investigation of the MgO adsorbate and the MgO/Fe interface on a GaAs(001) surface by means of XPS and XPD

Conference contributions:

DPG Frühjahrestagung Berlin, 2012
Speech on: Investigation of the three layer system MgO/Fe/GaAs(001) by means of XPS and XPD

DPG Frühjahrestagung Regensburg, 2013
Poster: Investigation of the MgO absorbate and the MgO/Fe on GaAs(001) surface by means of XPS and XPD

DPG Frühjahrestagung Dresden, 2014
Speech on: A photoelectron-diffraction investigation of the Fe/GaAs(4×2) interface

DPG Frühjahrestagung Berlin, 2015
Speech on: Is a surface reconstruction really necessary for an epitaxial Fe growth on a GaAs(001) surface?

List of Figures

List of Tables

Danksagung

An dieser Stelle möchte ich mich bei Personen bedanken, die zum Gelingen dieser Arbeit maßgeblich beigetragen haben.

Mein besonderer Dank gilt Herrn Prof. Dr. Carsten Westphal für die Vergabe dieses interessanten Themas, sowie seine Unterstützung und Förderung während meiner Doktorarbeit, die hilfreichen Diskussionen, wertvollen Anregungen und Motivationen.

Herrn Dr. Kai Phillip Schmidt danke ich herzlich, dass er sich Zeit genommen hat die Zweitkorrektur dieser Arbeit zu übernehmen.

Dem kompletten Lehrstuhl E1b danke ich für die schöne, lustige und produktive Zeit während meiner Arbeit. Ein besonderer Dank geht dabei an Frank Schönbohm für die große Unterstützung, Tobias Lühr für die theoretischen Diskussionen und Patrick Mehring für wertvolle Anregungen.

Ein weiterer großer Dank gebührt Marc Tesch, ohne ihn wären die magnetischen Messungen und dessen Interpretation nicht möglich oder denkbar gewesen. Danke für das Korrekturlesen der T-MOKE Kapitel und die wertvollen Anregungen.

Dem gesamten DELTA-Team danke ich für die Unterstützung während der Strahlzeiten.

Meiner Familie und meinen Freunden danke ich für die Unterstützung und die angenehme Zeit fern ab vom Promotionsstres und Physik.

Den größten Dank gebührt meinem Verlobten Holger Krull. Danke für deine Unterstützung, Motivation, Ratschläge, Diskussionen und Anregungen. Danke für die vielen liebevollen Stunden mit und ohne Physik.
Ich hätte es so gerne „Krullsches Pyramidenwachstum“ genannt ☺...

Danke